Titre: Title:	Spatially Distributed Interferometric Receiver for 5G Wireless Communications and Sensing Applications
Auteur: Author:	Bilel Mnasri
Date:	2019
Type:	Mémoire ou thèse / Dissertation or Thesis
Référence: Citation:	Mnasri, B. (2019). Spatially Distributed Interferometric Receiver for 5G Wireless Communications and Sensing Applications [Ph.D. thesis, Polytechnique Montréal]. PolyPublie. https://publications.polymtl.ca/3991/

URL de PolyPublie: PolyPublie URL:	https://publications.polymtl.ca/3991/
Directeurs de recherche: Advisors:	Ke Wu, & Serioja Ovidu Tatu
Programme: Program:	génie électrique

POLYTECHNIQUE MONTRÉAL

affiliée à l'Université de Montréal

Spatially distributed interferometric receiver for 5G wireless communications and sensing applications

BILEL MNASRI

Département de génie électrique

Thèse présentée en vue de l'obtention du diplôme de *Philosophiæ Doctor*

Génie électrique

Août 2019

POLYTECHNIQUE MONTRÉAL

affiliée à l'Université de Montréal

Cette thèse intitulée :

Spatially distributed interferometric receiver for 5G wireless communications and sensing applications

présentée par **Bilel MNASRI**

en vue de l'obtention du diplôme de *Philosophiæ Doctor*

a été dûment acceptée par le jury d'examen constitué de :

Mohammad S. **SHARAWI**, président
Ke **WU**, membre et directeur de recherche
Serioja Ovidiu **TATU**, membre et codirecteur de recherche
Cevdet **AKYEL**, membre
Roni **KHAZAKA**, membre externe

DEDICATION

To my family

ACKNOWLEDGEMENTS

First and foremost, I would like to sincerely thank Professor Ke Wu for being my supervisor throughout my doctoral studies. I am very grateful for his excellent guidance, his encouragement and patience during this journey. I particularly appreciate his devotion to research, his ability to combine theoretical aspects with engineering design, and his vast knowledge. Working with Professor Ke Wu has been an enjoyable and invaluable learning experience, which has inspired me to face challenges, question thoughts, and express ideas. My deepest thanks should also go to my Ph.D. co-supervisor, Professor Serioja Tatu for his advices and suggestions during the course of my studies, which have significantly contributed to the improvement my work. I would also thank Professor Tarek Djerafi for training and teaching me the art of microwave engineering. I also extend my gratitude to all jury members who have accepted to take time in order to evaluate this thesis. Their insightful comments have significantly contributed to improving this thesis presentation. In addition, I would like to thank various members of the technical staff of Huawei Technologies Canada for technical discussions and collaboration we had during the years. I am deeply indebted to my colleagues and friends. Their friendships have made my journey truly enjoyable.

I would like to thank Poly-Grames research center staff for their assistance and help over the years. My sincere thanks also go to Nathalie Lévesque, Louise Clément and Rachel Lortie for their friendship and administrative assistance during my studies at Polytechnique Montréal.

Finally, I would like to thank my family for all their immense love, presence and support. Nothing could have been possible without the long sacrifice of my parents over the years. This thesis is dedicated to them.

RÉSUMÉ

Les systèmes de télécommunications sans fils ont connu une révolution et un succès sans précédent dans l'histoire humaine, et ce depuis l'introduction de la première génération des réseaux mobiles au début des années 1980. Alors que ce premier standard de communication était essentiellement basé sur des méthodes de modulation analogique du signal, ce qui ne permettait que la transmission de la voix, les générations des systèmes de télécommunications qui ont succédé depuis le deuxième standard mondial GSM, se sont basées sur la transmission numérique qui représente une plateforme universelle pour le traitement des données de toute sorte (voix, donnés texte, vidéos haute définition, etc,). En effet, le traitement numérique du signal qui a débuté avec les premiers travaux sur la théorie de l'information, aux laboratoires Bell aux États-Unis vers la fin des années quarante du siècle passé, constitue le noyau dur de tous les standards de communication, y-compris la cinquième génération des réseaux 5G, dont la date d'entrée au marché mondial est prévue vers le début de l'année prochaine 2020.

En effet, les réseaux de communications sans fils actuels, avec au sommet de la pyramide le standard 4G-LTE, ne peuvent pas répondre aux attentes des utilisateurs et des entreprises en termes de débit de transmission de données qui ne cesse d'augmenter d'une façon exponentielle, et pouvant atteindre les 40 Exabytes par mois vers 2020. De plus, la naissance du concept de l'internet des objets (IoT) qui consiste en l'interconnexion d'un très grand nombre de mini-capteurs sans fils qui vont gérer des milliers, voire des millions d'activités des toutes sortes, tels que l'aide à la conduite des voitures dans les routes, le contrôle des températures et des feux dans les régions forestières, la transmission des données médicales des patients en temps réel vers les centres hospitaliers, etc.

Dans le but de répondre aux besoins actuels et futurs, la venue de la cinquième génération des réseaux des communications 5G est devenue urgente plus que jamais. En effet, ce nouveau standard ne sera pas une amélioration incrémentale de la 4G-LTE, mais sera plutôt toute une nouvelle plateforme intelligente offrant des débits de données allant jusqu'à plusieurs gigabits par seconde, avec un temps de latence ne dépassant pas 1 milliseconde dans le but d'assurer une qualité de service sans égal.

Pour réaliser toutes ces promesses, les éléments de la couche physique doivent être revisités. En particulier les récepteurs radiofréquences (RF) couramment utilisés dans le contexte des communications sans fils, tels que les architectures homodynes, hétérodynes et superhétérodynes ont des limitations bien qu'ils sont dotés d'un nombre d'excellentes caractéristiques (une plage dynamique large pouvant atteindre 100 dB, flexibilité de conception en basse fréquences, etc-). Ces limitations incluent leur consommation de puissance énorme, qui est due essentiellement à l'utilisation de plusieurs étages de mélange et amplification des signaux faibles pour faire descendre le spectre du signal reçu en bande de base, ce qui devient très couteux, surtout en ondes millimétriques. De plus, les architectures hétérodynes et superhétérodynes souffrent également d'une bande passante réduite qui est difficilement adaptée pour l'opération sur des portions larges du spectre électromagnétique, comme c'est le cas des ondes millimétriques.

Par conséquent, de nouvelles architectures de conception des circuits RF doivent être étudiées et validées pour résoudre les problèmes mentionnés et les proposer comme des alternatives aux récepteurs conventionnels. Dans ce contexte, cette thèse présente l'étude de nouvelles techniques interférométriques pour la réalisation de nouveaux récepteurs multi-entrées à démodulation directe et des systèmes de détection d'angle d'arrivée.

Tout d'abord, une architecture est présentée dans le but d'augmenter la plage dynamique des récepteurs RF basés sur les interféromètres six-ports. En effet, un récepteur six-port conventionnel souffre d'une plage dynamique limitée par la largeur de la zone linéaire des détecteurs de puissance utilisés à ses sorties, ce qui limite la taille des modulations que les six-ports peuvent traiter. La nouvelle architecture utilise deux jonctions six-port en parallèle, dont chacune est responsable de traiter une partie d'une large constellation dans le but de maximiser le débit de données offert ainsi que la plage dynamique du récepteur. Ensuite, un interféromètre spatial pour la détection de l'angle d'arrivée (AoA) d'un signal RF, en utilisant seulement trois coupleurs hybrides est présenté tout en analysant le phénomène d'ambigüité lié à la périodicité du AoA mesuré. Le volet suivant de la thèse est consacré pour l'étude théorique et expérimentale d'une nouvelle architecture d'un récepteur RF multi-entrées qui s'inspire de la technologie six-port et se base sur l'interférométrie spatiale dans le but de créer des corrélations qui vont être utilisées pour extraire le signal en bande de base transmis, tout en réduisant à moitié la perte de puissance du signal RF par rapport au récepteur six-port classique.

Dans le but d’augmenter le débit de données transmis, un détecteur de puissance logarithmique ayant un temps de montée de l’ordre de 17 nanosecondes est conçu et fabriqué dans le but de l’utiliser pour la démodulation haut débit avec des vitesses allant jusqu'à 120 Mb/s dans le cas d’une modulation 64-QAM, avec une qualité de réception mesurée par la métrique EVM (Error Vector Magnitude) comparable à celle obtenue par les récepteurs six-port conventionnels.

Finalement, une méthode pour la détection du AoA d’un signal RF est proposée en liaison avec le récepteur distribué multi-entrées, tout en se basant sur la transmission de symboles pilotes connues par l’émetteur et le récepteur. A la réception de ces symboles, il est possible de déterminer la différence de phase entre les signaux à l’entrée des antennes et déduire l’angle d’arrivée du signal reçu, tout en suivant un formalisme mathématique expliquant le principe d’opération ainsi que l’étude d’ambigüité concernant la détection du AoA.

ABSTRACT

Wireless communication systems are one of the most famous success stories in the field of engineering in modern era. In fact, the birth of the first generation of mobile communications goes back to the early 1980's. This first standard was based on analog modulation with the aim of transmitting only voice signals. And with the progress made in signal processing techniques and the large-scale productions of digital integrated circuits, the second generations of wireless communications was introduced in the nineties of the last century. Since then, a new standard for wireless mobile systems has been introduced every ten years or so, with ever increasing data rates, lower latency and better quality of service, thanks to the adoption of sophisticated modulation schemes and robust error correcting codes, in conjunction with improved hardware capabilities over the years. The magic progress in wireless technologies is strongly related to the magnificent research work pioneered by Claude Shannon on information theory in 1948 at Bell-labs, in combination with continuous research efforts conducted by millions of brilliant minds worldwide.

However, the current wireless generation of wireless systems 4G-LTE is unable to follow the explosion of wireless traffic, which is trigged by the exponential demand for higher data rates, which would create monthly traffic of about 40 Exabytes by 2020. Moreover, the birth of Internet of Things (IoT) concept is a driving force towards the emergence of a huge platform of billions of interconnected devices and sensors, used to control and monitor an ever-increasing number of applications (forests fire detection, intelligent cars, real-time health monitoring for sick and old people , etc.). As a matter of fact, the upcoming of the fifth generation (5G) of wireless mobile networks has become a very urgent necessity in order to meet the widely-discussed system requirements in terms of capacity, latency and quality of service.

Consequently, elements of the physical layer must be redrawn and reorganized in order to avoid the prohibited cost of network deployment and power consumption of billions of interconnected devices. In this thesis, we focus on the theoretical study and experimental validation of novel interferometric techniques to be adopted in the design of low-power direct conversion receivers,

which are capable of performing joint demodulation and angle of arrival (AoA) detection of RF signals.

This research topic is motivated by developing an effective approach to mitigating the limitations of conventional heterodyne and super heterodyne radio frequency (RF) receivers, in terms of power consumption along all the stages of mixing and amplification to down convert received modulated signals into baseband. In addition, these receivers are less suitable for operation at 5G millimeter waves because of their design complexity and manufacturing cost, although they present high dynamic range around 100 dB and beyond.

Thus, new alternative architectures for RF receivers must be studied and developed, considering overcoming the limitations of conventional architectures, which have been used for many decades. Within this context, this thesis presents a class of interferometric architectures for direct demodulation and angle of arrival detection for 5G applications and beyond.

First, a dual six-port receiver (SPR) is proposed to overcome the limited dynamic range of conventional six-port receivers and also to process high order modulations. In fact, the dynamic range of six-port receivers is fundamentally limited by the square law-region of power detectors used to detect the envelope of RF signals at their input, which is not linear, in practice, over a large power range. Thus, the proposed architecture makes use of two parallel six-port circuits to down-convert high order modulations and double the dynamic range of the whole receiver, while requiring 3 dB higher local oscillator (LO) power. Another multiport interferometer system for AoA detection is also proposed, along with a theoretical analysis of angular resolution and ambiguity-free detection range.

The main contribution of thesis consists in the theoretical study and experimental validation of a novel spatially distributed multi-input interferometer direct conversion receiver. The proposed architecture inherits the same advantages of conventional six-port receivers, such as design simplicity, low-power consumption, low-cost and easy scaling at millimeter-wave frequencies, while reducing the natural loss of six-port circuits by almost 50 %. This receiver is based on the use of a set of equally spaced antennas at the receiver, and exploits the phase correlation between wave fronts at antenna inputs, in order to create specific and precise correlations needed to extract the in-phase and quadrature components of RF modulated signals. The proof of concept

demonstration of the multi-input interferometer receiver shows excellent measurement results, which agree very well with theoretical foundations and simulations.

In order to provide experimental results at higher data rates, a power detector is designed and manufactured using the commercial Analog Devices AD8318 integrated circuit (IC), which exhibits a measured rise time of about 17 nanoseconds. This power detector enables the detection of modulated signals with bandwidth of up to 20 MHz, which makes possible the recovery of high order modulations such as 64-QAM at the speed of 120 Mb/s. Error vector magnitude (EVM) is adopted throughout the thesis as a metric to measure the quality of recovered baseband signals and compare it with state-of-the-art results reported in research literature, and all measurements show very promising results as the measured EVM does not exceed 10 % for all modulation schemes, which validate the feasibility of adopting the proposed interferometer receiver for future wireless systems. Moreover, the quality of received signal could be further improved through well-known calibration and linearization techniques. It is worth mentioning that the proposed receiver architecture offers 50 % less internal loss than conventional six-port receivers, while requiring three more antennas to operate in point-to-point communication scenarios. Although this represents more complexity and constraints in terms of coupling between adjacent antennas, which should be about -30 dB, the proposed multi-input architecture provides 3 dB more dynamic range than classic SPR and could be used in the design of multi-functional receivers.

Finally, a new method for detecting the angle of arrival of RF modulated signals using the proposed multi-input interferometric architecture is presented, which is based on sending a training sequence of symbols known at both the transmitter and receiver, and then extracts the phase difference between wave fronts received at the input of antennas using the recovered baseband signals following a mathematical modeling covering the principle of operation, as well as the study of the ambiguity-free detection range. The proposed method provides wider ambiguity-free intervals (up to 180) compared to conventional six-port based AoA detection systems.

TABLE OF CONTENTS

LIST OF TABLES

LIST OF FIGURES

LIST OF SYMBOLS AND ABBREVIATIONS

1-D	One-Dimensional
2-D	Two-Dimensional
5G	Fifth generation of wireless systems
ADS	Advanced Design System
AM	Amplitude Modulation
AoA	Angle of Arrival
AWGN	Additive White Gaussian Noise
BER	Bit Error Rate
BPSK	Binary Phase Shift Keying
CDMA	Code Division Multiple Access
EVM	Error Vector Magnitude
FCC	Federal Communications Commission
FDD	Frequency Division Duplex
GSM	Global System for Mobile communication
HFSS	High-Frequency Structure Simulator
I	In-Phase
IC	Integrated Circuit
IS-95	Interim Standard 95
ITU	International Telecommunications Union
LO	Local Oscillator
LTE	Long Term Evolution

MIMO	Multiple Input and Multiple Output
OFDM	Orthogonal Frequency Division Multiplex
Q	Quadrature
QAM	Quadrature Amplitude Modulation
RF	Radio Frequency
SNR	Signal to noise ratio
TDD	Time Division Duplex
TIA	Telecommunications Industry Association
UDN	Ultra Dense Network
UMTS	Universal Mobile Telecommunications Service

LIST OF APPENDICES

CHAPTER 1 INTRODUCTION

1.1 Motivation

Wireless communications have been one of the best success stories in the engineering field in the modern era. In fact, the Interim Standard (IS-95) was introduced by Qualcomm and then adopted as a standard by the Telecommunications Industry Association in TIA/EIA/IS-95 release published in 1995, as the first generation of Code Division Multiple Access (CDMA) based digital telephony in the United States [1]. Since then, a brand-new generation of wireless systems has been adopted every ten years or so [2]. IS-95 (Interim Standard-95) in the united states and GSM (Global System for Mobile communication) in Europe were at most able to provide data rates of about 9.6 Kb/s in early nineties, which just supported voice transmission and modest short messages service, with microwave carrier frequencies around 800/ 850/ 900/ 1800 MHz and using classic convolution coding, interleaving and simple diversity schemes as well as equalization to combat channel fading [3].

The third and fourth generations of mobile communications pushed the performances of telecommunication networks to unprecedented limits. In fact, the Universal Mobile Telecommunications Service (UMTS) and the Long Term Evolution (LTE) standards were introduced with novel modulation techniques such as Wideband-Code Division Multiple access (W-CDMA) and Orthogonal Frequency Division Multiplex (OFDM) in combination, with Multi-User Multiple Input Multiple Output MU-MIMO [4], and more robust coding schemes, which is needed to provide higher data rates of tens of Mb/s with better quality of service and ever decreasing latency to ensure that critical real time applications are supported [5].

However, with the exponential growth and explosion of mobile data traffic and the birth of a revolution of digital culture all over the planet, as people tend to use smartphones, tablets for data/video streaming, and billions of sensors for different goals are expected to be used by 2020 to connect vehicles, machines and collect/transmit data about temperature, fire activity, vital signals monitoring, the current 4G standard is just unable to carry on with the predicted volume of data traffic which is expected to be in order of tens of Exabytes per month in the coming years [6-10]. This urged the standardization bodies and the international regulatory agencies like the Federal Communications Commission FCC and the International Telecommunications Union

ITU to create special focus groups, which work hand in hand with industry in order to establish technical recommendations and general guidelines to be adopted within the fifth generation of wireless systems 5G [11-13].

1.2 Overview of 5G wireless standard

In order to meet the ever-increasing growth of data traffic in mobile networks, 5G network was introduced as a platform which is able to provide 1000 times more capacity (with a latency less than 1 millisecond) than the proceeding generation of wireless systems, namely 4G-LTE [14]. Although, this figure seems to be very promising, it is worth mentioning that it is very difficult to deploy it in practice using the same architecture of 4G standard. Hence, to get 5G network out of the myth into reality, researchers and engineers in both academia and industry have agreed on multiple critical points that should put 5G on the map within the next few years. Each of these points relates to one or more of OSI layers (Physical, Data link, Network, Transport, Session, Presentation and Application). And because this thesis focuses on some aspects of the physical layer, we will only introduce two features related to this layer of OSI model.

1.2.1 Massive MIMO

After Stanford university professor Paulraj introduced the MIMO concept for the first time in 1994 [15], mobile operators were very excited to apply this technology, which will enhance incredibly the spectral efficiency, and provide many orders of magnitude of wireless channels capacity without any increase in terms of transmitted power or allocated bandwidth. Many researchers invested significant efforts at Bell-Labs to prototype and test first MIMO prototypes [16]. However, it appeared soon that the mathematical modeling is far from reality and the expected scalable data rate with the number of antennas could not be reached in practice. The reason for this failure was discovered to be related to the fact that MIMO is only scalable in rich scattering environments with low correlation between antennas [17].

In real world measurements, the correlation between handset or base station antennas is strong, even in the absence of direct line of sight, which prevented MIMO to be a real revolution in wireless technology [18-20]. Some efforts went into the direction of looking at the problem from another point of view, by using multiple antennas at the base station, with multiple handsets

equipped with one antenna each, which is known as MU-MIMO [21]. However, the complexity of the dirty-paper coding technique to be used with the proposed scheme made MU-MIMO a good topic in academic research, but not for industry. Fortunately, Thomas Marzetta came up with the solution in his 2010 paper entitled: ‘’Noncooperative Cellular Wireless with Unlimited Numbers of Base Station Antennas’’[22], and demonstrated that MU-MIMO is a suitable solution when using so many antennas at the base station with single antenna handsets as illustrated in Figure 1.1. In fact, the use of a couple of hundred antennas at the base station in combination with maximum ratio combining or zero forcing at the base station alleviates even the need to estimate the channel in the downlink, while providing multiple orders of magnitude of increase in the sum spectral efficiency (up to 145 bits/sec/Hz) and allocating the whole the bandwidth to everyone within the cell, and not relying on FDD but rather on TDD [23]. Testbeds at sub-6GHz frequency, have been built in Sweden, England, the United States and China to verify the proposed solution of Marzetta and all of them agreed that Massive MIMO is going to be the benchmark of 5G [24-27].

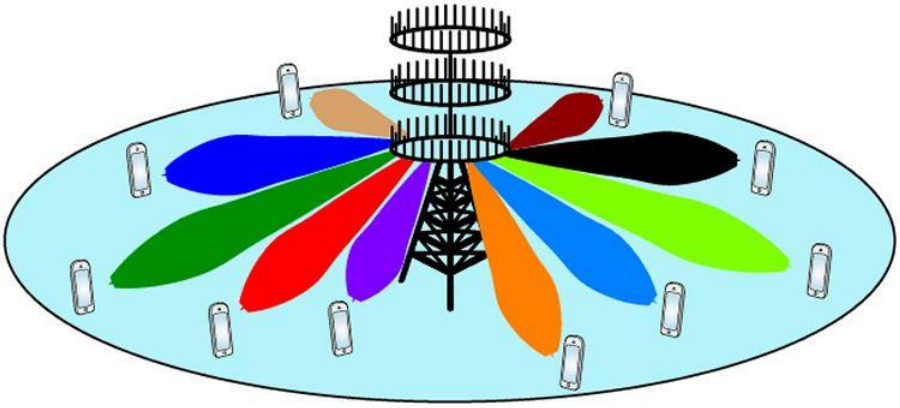

Figure 1.1 Massive MIMO: spatial multiplexing pushed to a pleasant extreme [28]

1.2.2 5G ultra-dense network

Sub-6 GHz frequencies have been always the preferred part of the electromagnetic spectrum to be used in wireless communications because of the easiness of RF circuits design at those frequencies, their low cost, and especially the ability of low frequencies to reach far distances as the pathloss behaves in free space, as the square of the inverse of the carrier frequency. These

characteristics of microwave frequencies were of great interest for mobile operators, when deploying their networks using large cells with radius of up to 30 km, which reduced the cost of deployment and enabled the fast penetration of past generations into the market.

Unfortunately, because of the scarcity of radio resources at microwave frequencies and the explosion of services and applications to be served in 5G networks, especially with the birth of internet of things (IoT), which would connect machines, sensors, etc.., and enable the automation of thousands of functions, it has been found evident that a migration toward millimeter waves is needed (28, 38 and 60 GHz), where several GHz of bandwidth are available for use [29-30]. Hence, it is obvious that 5G cellular network will be a combination of large umbrella cells using microwaves, where each large cell is subdivided in small cells (with radius in the range of few hundred meters) serving users through millimeter waves [31].

In fact, it is necessary to understand that 5G spectrum is not only about mm-waves, but it is rather a completely new paradigm of sub-6 GHz frequencies serving users with high mobility (e.g. vehicles with high speeds in highways) in order to avoid the traffic of handovers, and using mm-waves for users with low mobility and who demand high data rates, which is illustrated in Figure 1.2.

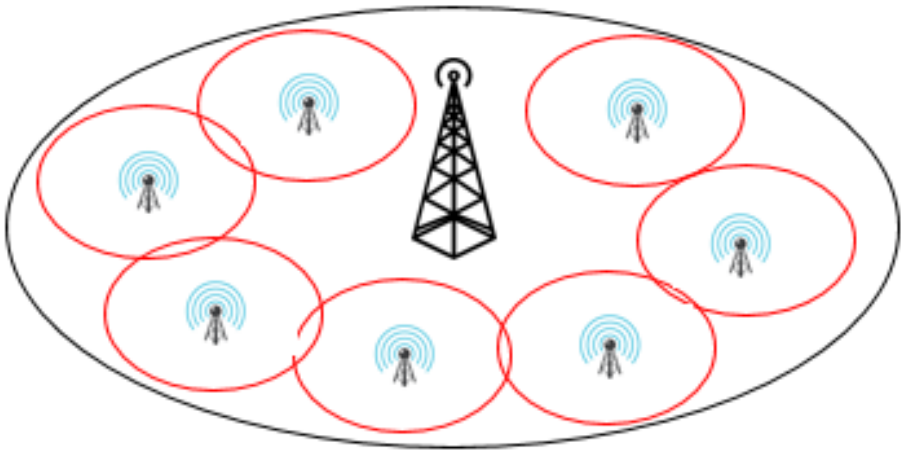

Figure 1.2 5G network densification

1.2.3 Power consumption and energy efficiency in 5G networks

The migration from one generation of wireless systems to the next faces many challenges and problems that need to be studied and solved. In fact, 5G networks are not an exception, as they must be planned in such a way to handle the extremely huge volume of data that is expected to be generated by the billions of connected devices. Moreover, the number of nodes in 5G backhaul network is going to be many orders of magnitude bigger than its counterpart in past generations, because of the ultra-densification of cells [32-35]. Thus, it is obvious that the energy consumption of 5G base stations will be greater than 4G network BSs. In addition, all connections in the backhaul subsystem must be wirelessly deployed to enable fast penetration into the market and mainly to reduce the costs, by avoiding fiber optics interconnectivity. There is also the lurking threat behind the promise of 5G delivering up to 1,000 times as much data as today's networks is that 5G could also consume up to 1,000 times as much energy, which is a big problem, since today's 4G network power consumption is already huge. Concerns over energy efficiency are beginning to show up at conferences about 5G deployments, where methods for reducing energy consumption have become a hot topic. As a matter a fact, new low-power wireless transceiver architectures must be introduced, studied and validated in order to be used within 5G systems in order to avoid a possible divergence of energy efficiency toward values that would complicate the deployment of the new technology [36-38].

1.3 Overview of RF receiver architectures

1.3.1 Super-heterodyne receiver

The most popular configuration for RF receivers is the super-heterodyne architecture. As depicted in Figure 1.3, this typical architecture is based on multiple down-conversion stages, where the received RF signal is first amplified and translated around an intermediate frequency using a first mixer Mixer 1 and a local oscillator LO1, then, a second down-conversion using LO2 takes place to get the baseband signal. The first band pass filter is used to pre-select the bandwidth of operation (which is essential to reduce the amount of noise gathered at the input of the low-noise amplifier LNA). The second band pass filter is needed for image rejection (the symmetric channel in the frequency domain that would fall around the same frequency after

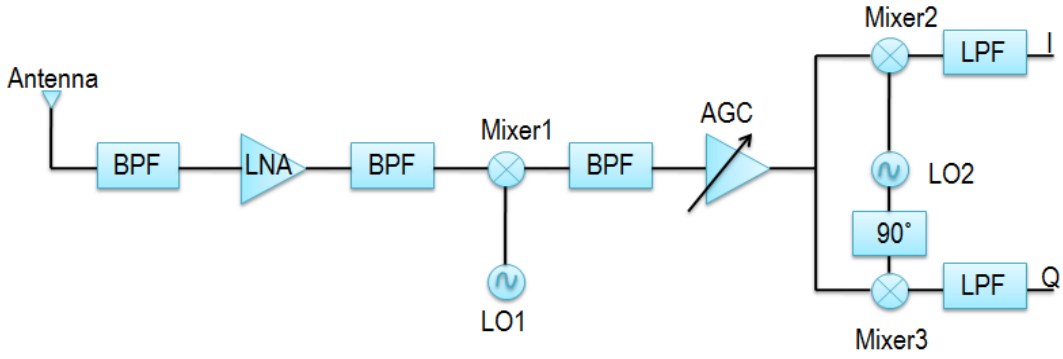

Figure 1.3 Super-heterodyne receiver block diagram

Mixer1). The third BPF is used for channel selection and both low-pass filters are used to get the baseband in-phase and quadrature components (I and Q) of the RF modulated signal. This architecture has been the most used in wireless receivers since its first introduction by American electrical engineer Edwin Howard Armstrong in his patent of 1917 [39]. In fact, super-heterodyne receivers ensure a good level of sensitivity (allowing lower power signal at receiver input for which there is sufficient signal-to-noise ratio at the receiver output) thanks to the multi-amplification stages, which clearly makes this architecture the best of RF receivers in terms of dynamic range, which could easily reach 120 dB. The good features of the super-heterodyne receiver are not a free lunch, because of the high-power consumption of this receiver (within the multi-amplification stages and the required LO power levels to drive the mixers) [40].

1.3.2 Homodyne zero-IF receiver

Another typical architecture is the zero-IF receiver, also known as the homodyne receiver, which is depicted in Figure 1.4. This architecture is a simplified version of the super-heterodyne receiver, because instead of using two or more down-conversion stages, it converts the RF signal directly to baseband. First, the modulated signal is first selected through a band pass filter, and then it is amplified. Finally, it is directly down converted to baseband using two mixers with a 90^{o} phase shift between them (to get I /Q components separately). Compared to the heterodyne

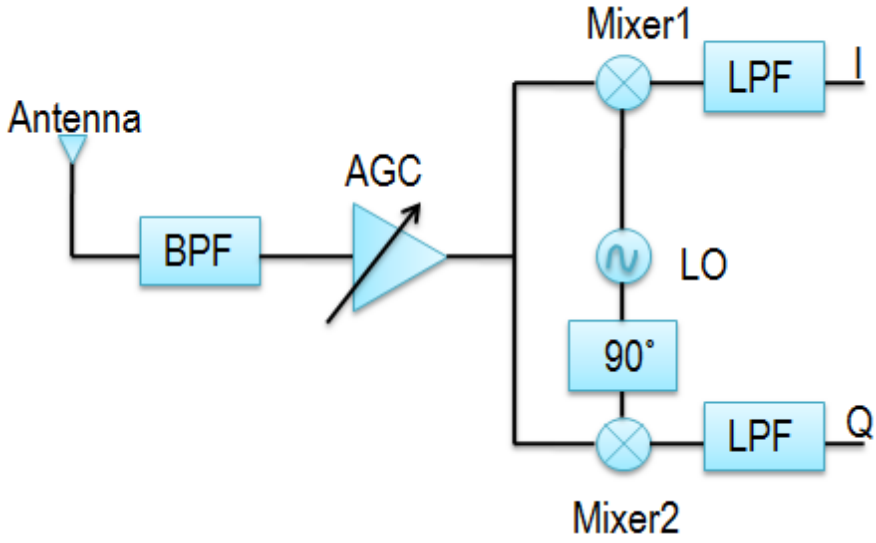

Figure 1.4 Homodyne receiver block diagram

architecture, this has a clear reduction in the number of analogue components and guarantees a high level of integration thanks to its simplicity. Despite its simplicity compared to the super-heterodyne architecture, many components of the zero-IF receiver are more complex to design and deploy. In addition, the direct translation to DC can generate several problems that have strongly conditioned the use of this architecture over its super-heterodyne counterpart.

Problems like DC offset (which is caused by local oscillator (LO) leakage to RF port resulting in unwanted self-mixing), I/Q mismatch due to errors in I/Q modulation have been widely reported in literature [41-43]. A similar configuration to the previous one is the low-IF receiver, in which the RF signal is mixed down to a non-zero low or moderate IF (few hundred kHz to several MHz) instead of going directly to DC, using quadrature RF down-conversion. This solution attempts to combine the advantages from the zero-IF receiver and the super-heterodyne receiver. This architecture still allows a high level of integration (advantage from zero-IF) but does not suffer from the DC problems (advantage from super-heterodyne), since the desired signal is not situated around DC. However, this architecture continues to suffer from the image frequency, I/Q mismatch problems and the ADC power consumption is increased as high conversion rate is required.

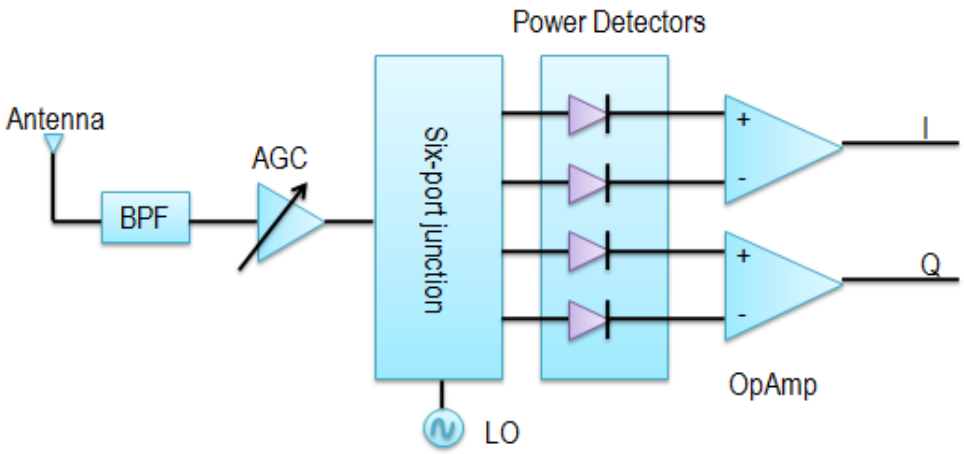

Figure 1.5 Six-port receiver architecture

1.3.3 Six-port receiver

The official birth year of the six-port measurement technique is 1977, when three fundamental papers [44] and several accompanying papers were published in the December issue of the IEEE Transactions on Microwave Theory and Techniques. Although the inventors, Glenn F. Engen and Cletus A. Hoer of the National Bureau of Standards (now National Institute of Standards and Technology), Boulder, Colorado, USA, had published papers with partial ideas and used the term previously, these articles presented for the first time a complete and unified theoretical background and offered guidelines for optimum six-port design [45]. The six-port technique is a method of network analysis, i.e. that of scattering parameters measurement: either only of reflection coefficient, in which case we speak about six-port reflectometer (SPR) or both reflection and transmission coefficients, in which case we speak about six-port network analyzer (SPNA).

In May 1994 and during IMS week in San Diego, California, USA., J. Li, a Ph.D. candidate under the supervision of Professor Ke Wu and Professor Renato G. Bosisio in the Poly-Grames Research Center at Polytechnique Montreal, presented for the first time the six-port receiver and proved the concept of calculating the complex ratio of an incoming modulated signal and a known local oscillator (LO) signal by using the six-port technique [46]. Since then, hundreds of research papers have been published and presented with the study and implementation of six-port

based RF receivers capable of incorporating many functions such as demodulation, angle of arrival detection, Doppler shift detection for RADAR applications, etc. As depicted in Figure 1.5, the canonical architecture that is widely known for six-port receivers is composed of a passive junction composed of power dividers and/or hybrid couplers. This junction is in charge of providing interferometric combinations between the LO reference signal and the incoming RF modulated signal. These combinations are required to discriminate the angle and amplitude of the received signal after passing the four outputs of the junction through power detectors operating under their square law-region [47]. In fact, the six-port receiver has many advantages over conventional heterodyne and homodyne receivers. However, SPR has its own limitations, which will be summarized in the Table 1.1.

Table 1.1 Comparison of RF receiver architectures

Architecture	**Advantages**	**Major problems**
Super-heterodyne	✓ Selectivity ✓ Sensitivity ✓ High dynamic range	✓ Image frequency ✓ Complexity ✓ Huge LO power
Homodyne	✓ Simplicity ✓ IC integration	✓ Strong DC problems ✓ High LO power
Low-IF	✓ No DC problems ✓ Simplicity of design	✓ Requires high performance ADC ✓ Image frequency
Six-port receiver	✓ Broadband junction ✓ Simplicity of design ✓ Suitable for mm-waves ✓ Very low LO power	✓ Limited dynamic range ✓ More than 6 dB of loss I/Q mismatch ✓ Non-linearity of power detectors

1.4 Major contributions

This Ph.D. thesis focuses on the study, analysis, design, implementation and experimental validation of a novel interferometric receiver. In fact, the six-port receiver has attracted attention from both academia and industry for its many advantages (some of them are listed in Table 1.1.1). SPR is attractive for 5G applications because it requires many orders of magnitude less LO power than conventional heterodyne/homodyne receivers. Hence, it is well suitable for devices to be used in the next generation of wireless systems, in order to considerably reduce the energy consumption of the whole network. Moreover, SPR can easily be implemented at mm-waves using simple circuitry which could be integrated on the same PCB, which has been proved and demonstrated in many research papers at 28 GHz, 60 GHz and beyond. However, the six-port receiver suffers from its low dynamic range, which is limited by the width of the square law region of power detectors. In addition to not being able to compete against classic homodyne and heterodyne receivers in terms of dynamic range, SPR presents at least 6 dB of loss within the six-port junction because of the use of passive hybrid couplers. In practice the loss is greater than 6 dB caused by substrate loss of the fabricated circuits.

In this context, we propose in this thesis, a dual SPR receiver that provides twice the dynamic range of classic SPR while requiring only 3 dB more LO power, which enables the recovery of high order modulation schemes at reduced EVM values when compared to conventional SPR. In addition, a novel spatially distributed multi-input interferometric receiver is proposed. This receiver inherits all the advantages of classic SPR and reduces their loss by 50%. Various modulation schemes are successfully received with an EVM less than 10 % using a test bed implemented at 5 GHz for proof of concept demonstration. And to operate at higher data rates, a power detector is also designed using Analog Devices AD8318 chip with a measured rise time of about 17 ns. This power detector is used to improve measured data rate for up to 20 MS/s.

Finally, we propose a method for AoA detection using the proposed spatially distributed multi-input receiver. This method is based on sending a training sequence, which is known at the transmitter and receiver. Then, AoA can be easily computed within the ambiguity-free interval using a simple algorithm. Measurements results carried out at 5 GHz show good agreement with

simulations with an error less than 10%, which validates the feasibility of using the proposed method for AoA detection.

1.5 Thesis organization

This research work starts from the foundations of conventional six-port receivers and proposes new alternatives for the design of more flexible architectures capable of performing joint direct demodulation and angle of arrival detection. The present thesis is organized as follows:

Chapters 1 and 2 present a general introduction for the thesis research work, by exploring the history of wireless technology and providing an overview of 5G standard, with a summary of digital communications and their application in the study of conventional demodulators.

In chapter 3, we propose a dual six-port receiver with improved dynamic range. The proposed six-port based receiver makes use of two six-port passive circuits operating in parallel to process high-order modulation schemes. An experimental prototype is developed in order to validate the theoretical modeling, and reported measurement results have confirmed the capacity of this architecture in doubling the dynamic range of six-port receivers. A simple interferometer-based direction of arrival detection system is also reported in chapter 4, which is composed of three hybrid couplers and combines the waves received through four equally-spaced antennas in order to determine the angle of arrival through a process of phase discrimination.

Chapter 5 presents the mathematical modeling for the principle of operation of a novel spatially distributed multi-input interferometric receiver. The new receiver architecture aims to reduce the natural loss of classic six-port receivers, while inheriting all their advantages such as design simplicity, low-cost and low power consumption. Simulations results for various effects, like antenna coupling and carrier frequency offset are reported in this chapter. An experimental prototype operating at 5 GHz is investigated in chapter 6, in order to validate the theory and simulations of chapter 5 and compare obtained results with those reported in the published state-of-the-art.

In chapter 7, we provide further measurement results covering more aspects, in the aim of assessing the performance of the proposed architecture at different values of the received power and at higher data rates when using fast power detectors having a short-rise time. In addition, a

new method is presented in chapter 8, for angle of arrival detection through the baseband recovery of a training sequence known at the transmitter.

Finally, a summary of the research outcomes is given in chapter 9. This is supported by some concluding remarks and some interesting research tracks to be followed in the future based on the introduced ideas through this dissertation.

CHAPTER 2 STATE OF THE ART OF DIGITAL COMMUNICATIONS

In order to make this thesis self-consistent and self-contained, this chapter presents a general overview of digital communications, by working out the fundamentals. First, a brief history of digital communications is presented. Then, the basics of digital modulation/demodulation techniques are introduced in connection with practical RF implementations. Finally, some well-known performance indicators such Error Vector Magnitude EVM and bit error rate BER are presented for different wireless channels.

2.1 History of wireless communications going digital

The beginning of the twentieth century witnessed the first attempts of transmitting voice wirelessly using analog AM modulation. Later, wireless telegraphy appeared as one of the first techniques to transmit information as a series of discrete symbols (dot, dash, letter space, word space). Nyquist and Hartley made incredible and important contributions in modeling communication theory in their Bell System Technical Journal papers of 1924 and 1928, respectively [48-49]. They both introduced some first approximation relationship affecting wireless telegraphy speed, noise and bandwidth. However, digital communications and the theory of information were not fully understood until Claude E. Shannon published his historical paper of 1948, entitled: *A Mathematical Theory of Communication*, which is considered the best paper ever written in the field of engineering [50]. In this paper, Shannon was able to give an abstract model for any digital communication system and he derived the first closed-form expression for the capacity of transmitting information (maximum data rate) in the case of an additive white Gaussian noise, as a function of available bandwidth B and signal to noise ratio SNR

$$C = B.\log_2(1 + SNR) \tag{2.1}$$

Shannon demonstrated that for a given set of B and SNR, one could transmit and receive data at any rate $R<C$ at any arbitrarily low error value, using a suitable modulation/coding scheme. It is worth mentioning that the goal of any communication system (including 5G and beyond) is to increase data rates and try to reach the Shannon capacity, which is a fundamental limit. As a

matter of fact, 5G systems will include new portions of the electromagnetic spectrum (mm-waves), as the low microwave frequencies can no longer offer the expected data rates, and thus more bandwidth is needed to linearly increase the capacity of 5G systems.

2.2 Basics of digital modulation

Radio communications are used for transmitting and receiving information wirelessly, through radio. In communication systems, a process called digital modulation is very crucial since it transforms digital symbols into waveforms that are compatible with the characteristics of the channel, so that signal transmission becomes more efficient. Digital modulation includes baseband modulation as well as bandpass modulation. In the baseband modulation, these waveforms are a sequence of shaped pulses, which are made suitable for wired communications. On the other hand, in the bandpass modulation, shown in Figure 2.1, the shaped pulses further modulate a high-frequency sinusoidal signal, which is often called a carrier. The bandpass modulation is essentially shifting the low-frequency spectrum of the shaped pulses to a high carrier frequency. In this way, it brings up a number of advantages for wireless signal transmission. First, high-frequency signals can be radiated effectively by an antenna with reasonable size. Second, high-frequency signals from different sources can share a single channel through frequency-division multiplexing. Third, interference can be minimized through some modulation schemes. Finally, some system operations such as filtering and amplification can be easily performed by properly choosing a carrier frequency [51].

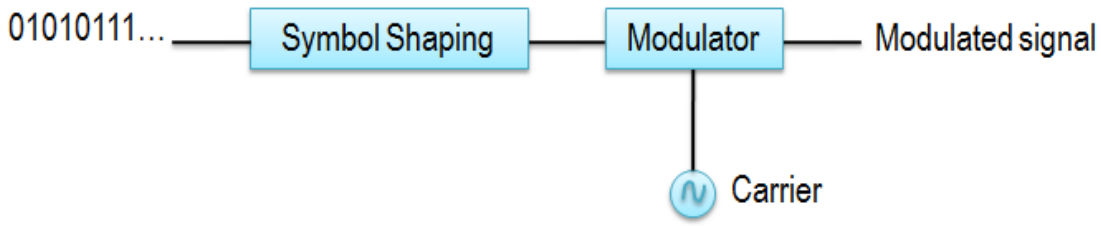

Figure 2.1 Schematic of bandpass modulator

Let us denote a sinusoidal signal (carrier) as:

$$S(t) = A.\cos(\omega t + \theta) \tag{2.2}$$

where A, ω, θ are the amplitude, the radian frequency and the phase of the carrier signal, respectively. By varying one or more of these three parameters, we can obtain fundamental bandpass modulation techniques: ASK, FSK and PSK and QAM.

2.2.1 Amplitude shift keying

The expression of an ASK modulated signal is:

$$S_i(t) = A_i.\cos(\omega_c t + \theta_0); i = 1..N \tag{2.3}$$

where the amplitude of the carrier Ai changes with respect to the corresponding input signal, while ω_c and θ_0 are kept constant. Binary ASK (often called on-off keying (OOK)) is a special case of ASK modulation. Figure 2.2(a) shows the digital symbols and the corresponding modulated waveform of an OOK signal, and Figure 2.2(b) illustrates OOK constellation.

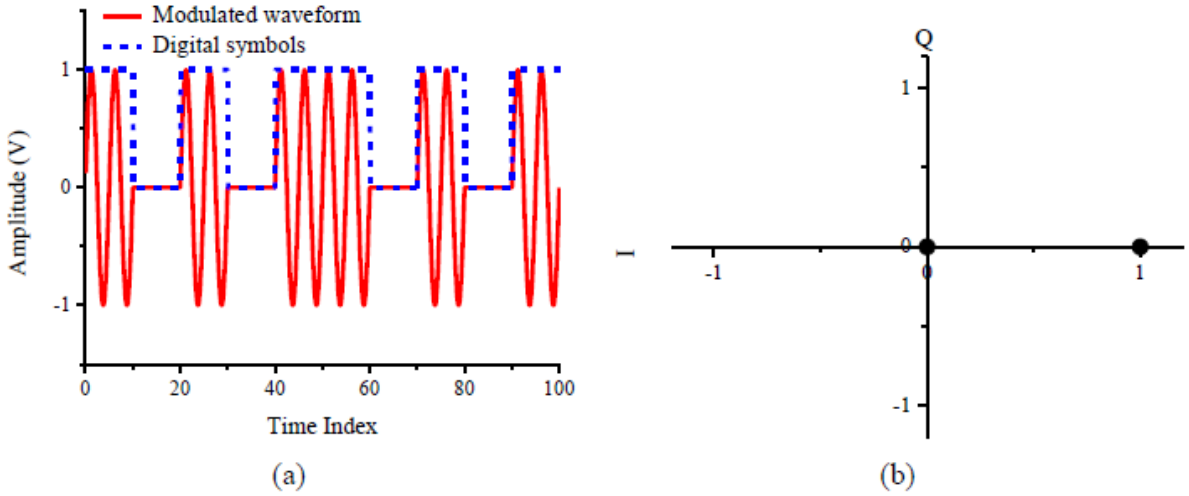

Figure 2.2 (a) Waveform and (b) constellation diagram of OOK signal

Binary ASK is the simplest of the digital modulation in terms of mathematical modeling, as well as from the point of view of practical implementation of the both the modulator and demodulator. However, OOK only offers 1 bit per transmitted symbol, and thus it is not spectrum efficient, but

it is always preferred for use when only low data rates are needed, or when the signal to noise ratio is so low, and cannot handle complex modulation schemes. This modulation could be more spectrum efficient if the carrier is modulated with multi-levels to enhance the overall bit rate.

2.2.2 Frequency shift keying

An FSK modulated signal is expressed as:

$$S_i(t) = A.\cos(\omega_i t + \theta_0); i = 1..N \tag{2.4}$$

where the radian frequency of the carrier ω_i changes with respect to the corresponding input signal, while A and θ_0 are kept constant. Figure 2.3(a) shows the digital symbols and the corresponding modulated waveform of a binary FSK (BFSK) signal, and Figure 2.3(b) illustrates the corresponding constellation.

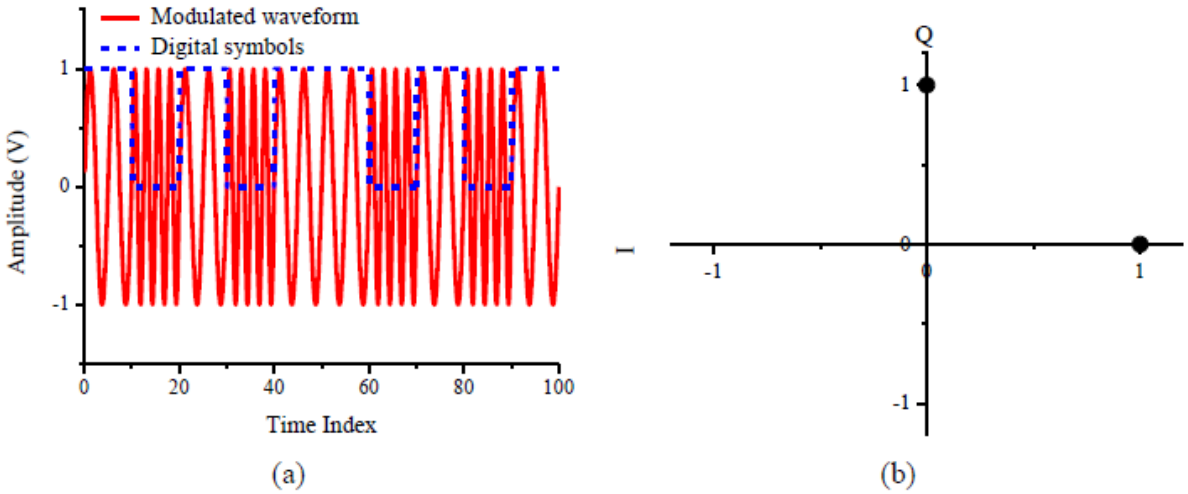

Figure 2.3 (a) Waveform and (b) constellation diagram of BFSK signal

FSK is more robust against noise than ASK and thus is preferred to achieve lower BER, however, it is not spectrum efficient as it requires more bandwidth than any other modulation scheme. Thus, the designer of any communication system must make a compromise while choosing the suitable modulation scheme, given the constraints he is dealing with [52].

2.2.3 Phase shift keying

A signal modulated using PSK is generally expressed as:

$$S_i(t) = A.\cos(\omega_c t + \theta_i); i = 1..N \tag{2.5}$$

where θi will have N discrete values while A and ω_c are constant.

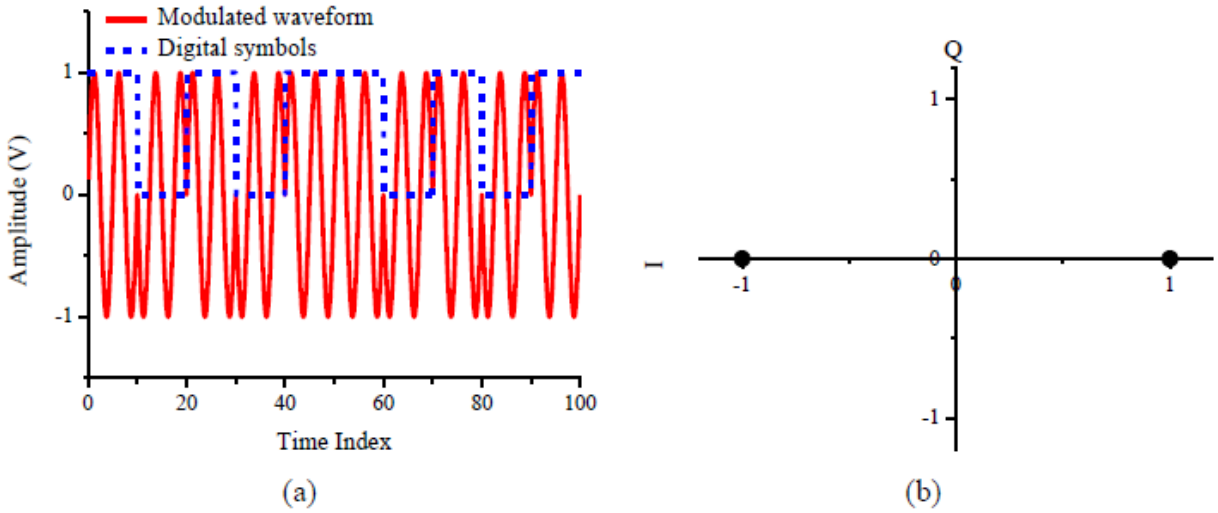

Figure 2.4 (a) Waveform and (b) constellation diagram of BPSK signal

Figure 2.4(a) shows the digital symbols and the corresponding modulated waveform of a binary PSK (BPSK) signal. We can see that the modulated waveform adopts two different phase conditions according to the value of digital symbols. From the corresponding constellation diagram shown in Figure 2.4(b), we can observe that the BPSK signal has the largest Euclidean distance for a given signal energy, and therefore, it should have the lowest BER for a given SNR compared to OOK and BFSK signals [53].

2.2.4 Quadrature amplitude modulation

In order to enhance the spectrum efficiency of previously stated modulation schemes, another form of encoding symbols into discernable waveforms is known as QAM, which modulates instantaneously two orthogonal sinusoids and adds the two obtained modulated carriers before transmission. Hence, M-ary QAM modulations can created (where M is the size of the constellation) where each of the orthogonal sinusoids is modulated through an $M^{-1/2}$ PAM modulation. In Figure 2.5(a), 4-QAM is also regarded as quadrature PSK (QPSK). Due to its high transmission efficiency, QAM is extensively used in wireless communications. And if the signal

to noise ratio allows it, then high order QAM modulations could be used like 16-QAM, which is depicted in Figure 2.5(b)

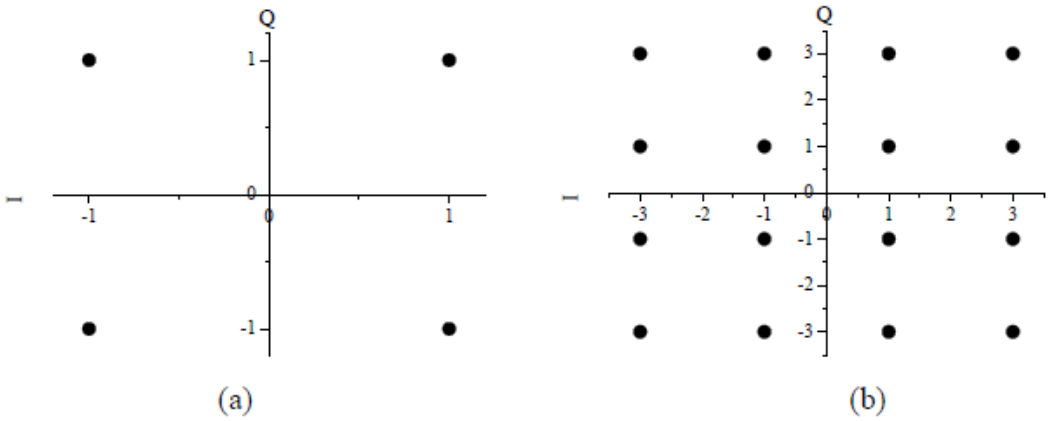

Figure 2.5 Constellation diagram of (a) 4-QAM (QPSK) signal and (b) 16-QAM signal

2.3 Quadrature demodulation

The reverse process of modulation is called demodulation and it consists in the extraction of the baseband signal containing the transmitted information from the received RF bandpass modulated signal.

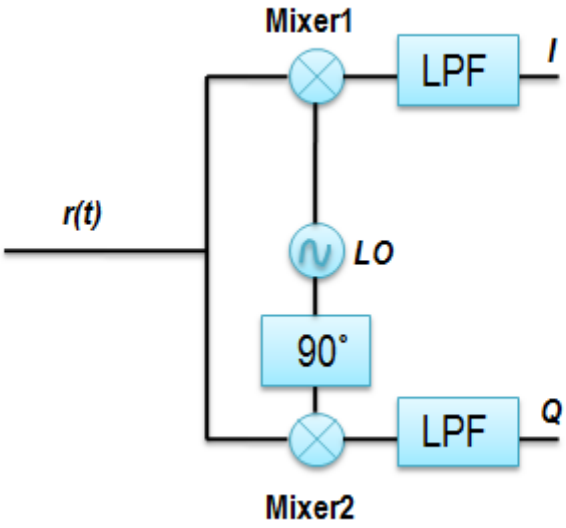

Figure 2.6 Block diagram of an ideal quadrature demodulator

Let us simply express the received signal *r(t)* as:

$$r(t) = I.\cos(\omega_c t) + Q.\sin(\omega_c t) \tag{2.6}$$

where *I* and *Q* are the in-phase and quadrature components of the received signal. And ω_c is the radian frequency of the carrier. At the receiver, a reference signal *u(t)* is used to demodulate the received signal and it can be denoted as:

$$u(t) = \cos(\omega_c t) \tag{2.7}$$

As depicted in Figure 2.6, In the I-channel, the received signal is mixed with a coherent reference signal, and then the mixing products are filtered by a low-pass filter (LPF), which gives the in-phase component of the received signal. This process can be mathematically represented as follows.

$$\begin{aligned} r(t).\cos(\omega_c t) &= (I.\cos(\omega_c t) + Q.\sin(\omega_c t)).\cos(\omega_c t) \\ &= I.\frac{1+\cos(2\omega_c t)}{2} + Q.\frac{\sin(2\omega_c t)}{2} \\ &\xrightarrow{LPF} I \end{aligned} \tag{2.8}$$

In the same way, the quadrature components can be extracted by mixing the received signal with the same coherent signal shifted by 90^0 and applying a low pass filter to the output of the mixer.

$$\begin{aligned} r(t).\sin(\omega_c t) &= (I.\cos(\omega_c t) + Q.\sin(\omega_c t)).\sin(\omega_c t) \\ &= I.\frac{\sin(2\omega_c t)}{2} + Q.\frac{1+\cos(2\omega_c t)}{2} \\ &\xrightarrow{LPF} Q \end{aligned} \tag{2.9}$$

2.4 Quantification of the quality of transmission

2.4.1 Error vector magnitude

The error vector magnitude or EVM (sometimes also called relative constellation error or RCE) is a measure used to quantify the performance of a digital radio transmitter or receiver. A signal sent by an ideal transmitter or received by a receiver would have all constellation points precisely at the ideal locations, however various imperfections in the implementation (such as carrier

leakage, low image rejection ratio, phase noise etc.) cause the actual constellation points to deviate from the ideal locations. Informally, EVM is a measure of how far the points are drifted from the ideal locations.

Noise, distortion, spurious signals, and phase noise all degrade EVM, and therefore EVM provides a comprehensive measure of the quality of the radio receiver or transmitter for use in digital communications.

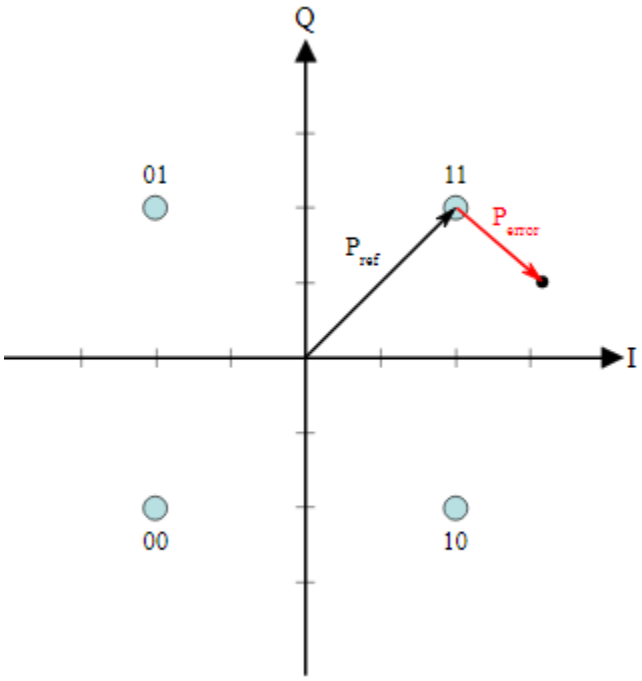

Figure 2.7 Constellation diagram and error vector

As illustrated in Figure 2.7, an error vector is a vector in the complex plane between the ideal constellation point and the point received by the receiver. In other words, it is the difference between actual received symbols and ideal symbols, and is mathematically expressed as [54]:

$$EVM\,(\%) = \sqrt{\frac{\sum (r_n - s_n)^2}{\sum s_n^{\,2}}}.100 \tag{2.10}$$

where r_n and s_n are the received and the ideally transmitted symbols, respectively.

2.4.2 Bit error rate

In digital transmission, the number of bit errors is the number of received bits of a data stream, over communication channels, which have been altered due to noise, interference, distortion or bit synchronization errors. The bit error rate (BER) is the number of bit errors per unit time. The bit error ratio (also BER) is the number of bit errors divided by the total number of transferred bits during a studied time interval. Bit error ratio is a unitless performance measure, often expressed as a percentage.

In simulations, BER may be evaluated using stochastic (Monte Carlo) computer simulations. If a simple transmission channel model and data source model is assumed, the BER may also be calculated analytically using closed-form expressions. The computation of bit error rate has been extensively studied in literature, and we can find BER closed-form expressions for almost all types of wireless channels (AWGN, Rayleigh, Rice, Nakagami-n, Nakagami-m, etc..) [55]. In fact, an additive white Gaussian noise channel is only an ideal model that does not exist in reality, and is only used for education purposes, because of its simplicity and the easiness of equations derivation in AWGN context. In the case of a wireless link with no line-of-sight component, the channel is modeled as Rayleigh. If a line-of-sight component is present, the channel is called Ricean. In some special cases, it has been shown that none of the aforementioned channel models fits with real world measurements. For this reason, new models were developed, like Nakagami-n and Nakagami-m, which incorporate parameters that can take into account new phenomena that Rice and Rayleigh models cannot describe [55].

The analysis of the performance of any communication system must include the study of bit error rates for different modulations schemes within the channel, in which the transmitter and receiver are deployed. Such analysis is crucial in system design, as it will determine how much power the transmitter must radiate and what kind of channel coding technique must be used to decrease error rate at the receiver side. It is worth mentioning that EVM and BER are related to each other through a closed-form expression, so determining one of them through simulations or measurements is enough to get the value of the other parameter [56].

$$P_b \approx \frac{2(1-\frac{1}{L})}{\log_2 L}.Q\sqrt{\left[\frac{3.\log_2 L}{L^2-1}\right]\frac{2}{EVM^2{}_{RMS}.\log_2 M}} \tag{2.11}$$

The following table gives closed-form expressions for SER and BER in AWGN channel, as a function of the signal to noise and bit energy to noise ratios.

Table 2.1 Symbol and bit error probabilities for coherent modulation in AWGN channel

Modulation	**Symbol Error Rate: SER**	**Bit Error Rate: BER**
BPSK	$P_s = Q(\sqrt{2\gamma_s})$	$P_b = Q(\sqrt{2\gamma_b})$
QPSK	$P_s \approx 2Q(\sqrt{\gamma_s})$	$P_b = Q(\sqrt{2\gamma_b})$
M-PSK	$P_s \approx 2Q(\sqrt{\gamma_s}\sin(\pi/M))$	$P_s \approx \frac{2}{\log_2 M} Q(\sqrt{2\gamma_b \log_2 M}\sin(\pi/M))$
M-QAM	$P_s \approx 4Q(\sqrt{\frac{3\bar{\gamma}_s}{M-1}})$	$P_s \approx \frac{4}{\log_2 M} Q(\sqrt{\frac{3\bar{\gamma}_b \log_2 M}{M-1}})$

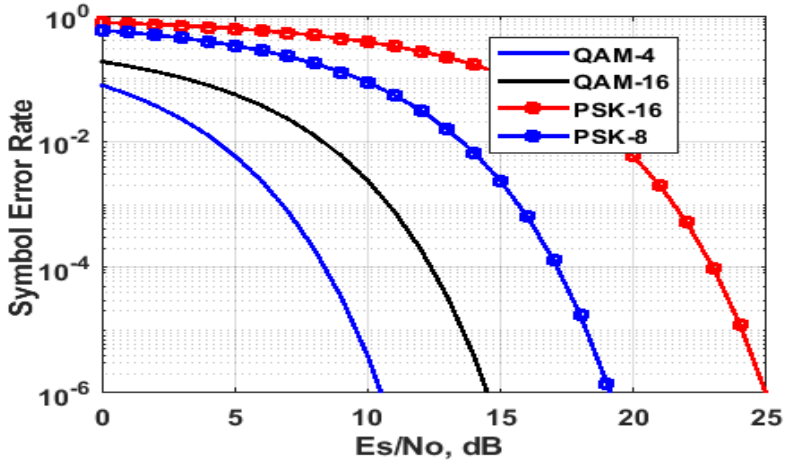

Figure 2.8 Bit-error rate simulation results for BPSK, QPSK, 8-PSK and 16-PSK, over AWGN channel.

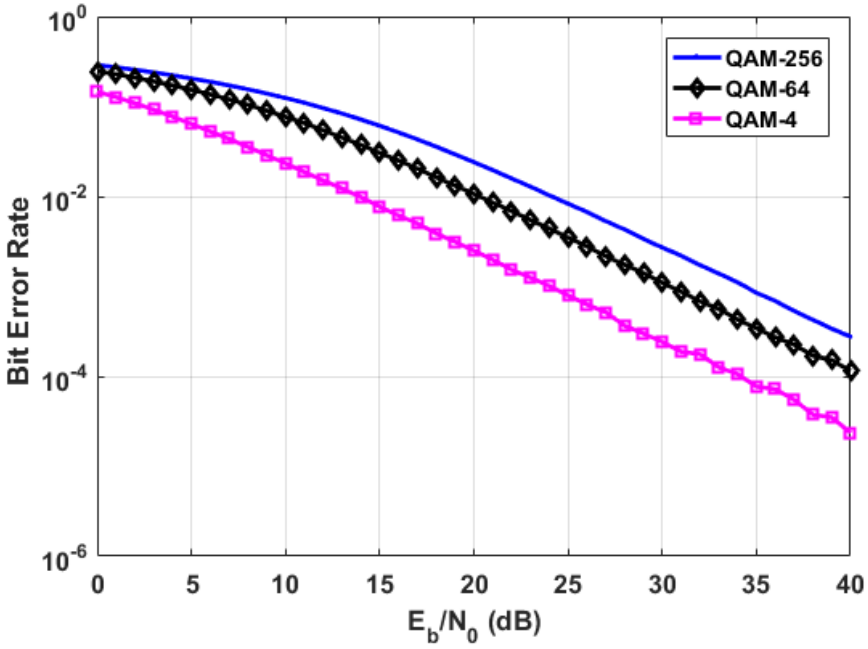

Figure 2.9 Bit-error rate simulation results for QAM-4, QAM-64 and QAM-256, over Rayleigh channel.

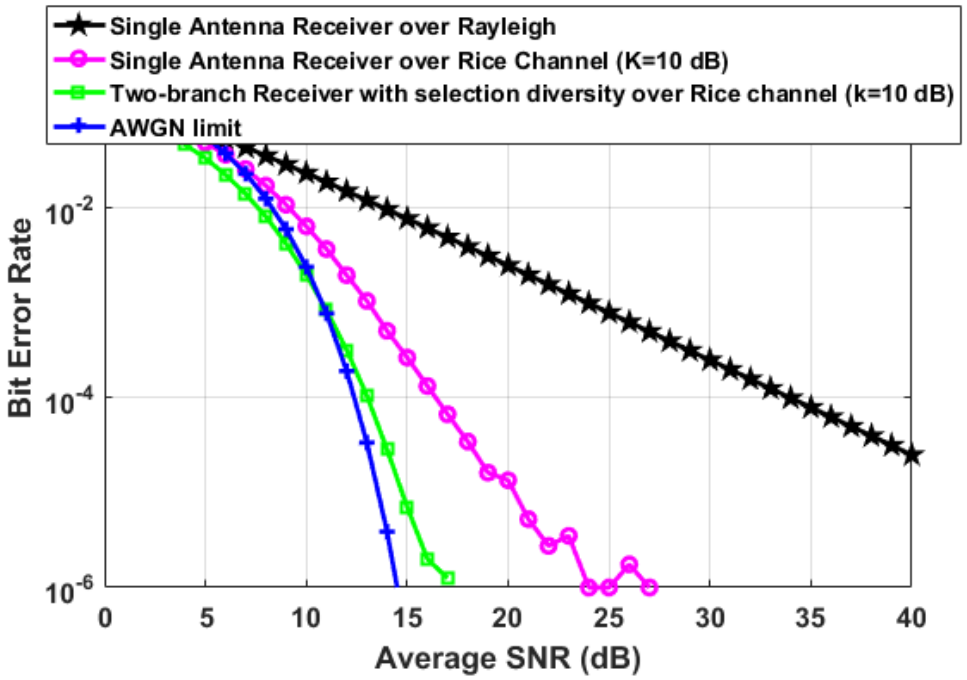

Figure 2.10 Bit error rate simulation results of QAM-16 with selection diversity over Rice channel (K=10 dB)

2.5 Conclusion

This chapter has briefly introduced the history of digital communications. Then, several basic digital bandpass modulation techniques, as well as the process of demodulation were presented. Finally, the chapter was concluded by illustrating some key performance indicators of digital transmission, namely, the error vector magnitude EVM and bit error rate BER. Both metrics will be used in next chapters when examining the performances of the proposed receiver architecture.

CHAPTER 3 DYNAMIC RANGE IMPROVEMENT OF SIX-PORT RECEIVER

There is an increasing demand for high data-rate wireless communications and broadband transceiver/ receiver systems with reduced hardware complexity and high flexibility. However, the existing hardware architectures for radio communication systems suffer from a number of limitations including high cost, design complexity, as well as high power consumption. For instance, for most mixers in conventional receivers, to obtain a good conversion gain, the power of local oscillator must be more than 10 dBm [57], which is a relatively high-power level. Moreover, in conventional receiver systems, the phase noise of the local oscillator (LO) is transformed directly into the phase noise in the baseband [58]. This results in adjacent channel interference, usually caused by reciprocal mixing, consequently decreasing the selectivity of the receiver. Radio architectures having a potential to overcome the previously mentioned limitations include six-port based RF receivers. The design simplicity combined with the wideband characteristics of a six-port receiver architecture tackles many of the current challenges of receiver systems. It provides a straightforward approach for broadband operations, low power consumption, and low manufacturing cost, making it a promising candidate for various applications within the next generation of wireless systems 5G [59-60].

3.1 Operation principle of the six-port receiver

The six-port circuit was first introduced by Cohn and Weinhouse to evaluate the phase of a microwave signal, and it was extended by Hoer and Engen as an alternative low-cost network analyzer to be used for the accurate computation of the reflection coefficient of microwave circuits. Between 1972 and 1994, several research activities around the six-port concept were conducted by many laboratories including Poly-Grames Research Center of Ecole Polytechnique de Montreal, where the six-port was used for the first time in history as a direct conversion millimeter wave receiver. Since then, the six-port direct conversion receiver (SPR) has attracted attention from both academia and industry, where it has used as modulator, demodulator, in radar application and angle of arrival detection systems, and in many other applications [61-65].

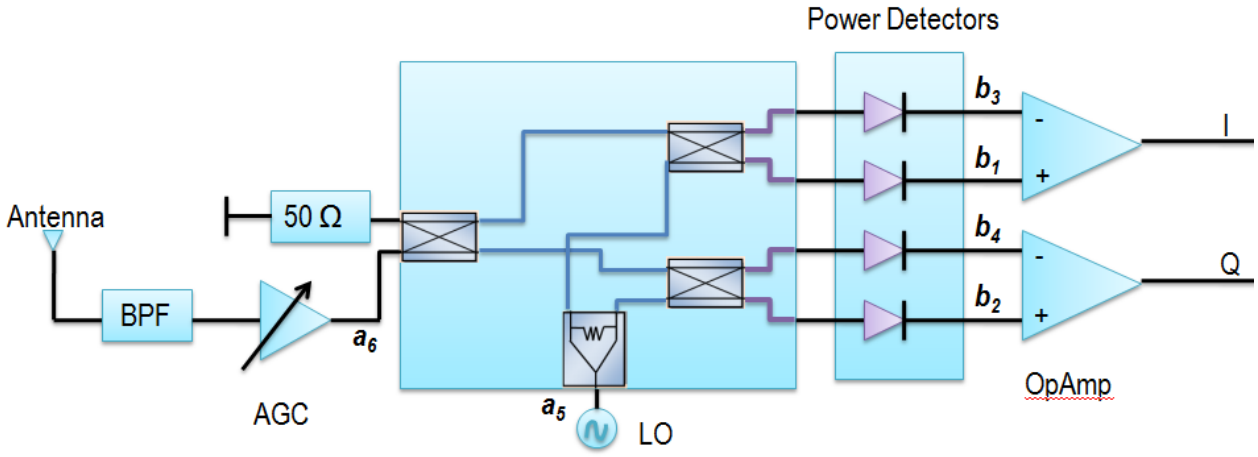

Figure 3.1 RF Front-End for a conventional six-port receiver

As depicted in Figure 3.1, the six-port receiver is composed of antenna that operates around the required frequency band followed by a bandpass filter (BPF) for channel selection, an Automatic Gain Control (AGC) that amplifies the incoming RF signal and overcomes the fluctuations of the carrier power, which can be caused of channel fading. Once the RF modulated signal is amplified and filtered, it goes, along with the local oscillator LO reference, through a six-port passive junction to create four interferometric, linear and independent signal combinations. The S-matrix for a Wilkinson power divider and a hybrid coupler are given by [66]:

$$S_{wilkinzon} = -\frac{j}{\sqrt{2}}\begin{bmatrix} 0 & 1 & 1 \\ 1 & 0 & 0 \\ 1 & 0 & 0 \end{bmatrix} \tag{3.1}$$

$$S_{wilkinzon} = \frac{1}{\sqrt{2}}\begin{bmatrix} 0 & j & 1 & 0 \\ J & 0 & 0 & 1 \\ 1 & 0 & 0 & j \\ 0 & 1 & j & 0 \end{bmatrix} \tag{3.2}$$

Thus, using the above matrices, the scattering matrix for the whole six-port circuit can be easily written as:

$$[S] = \frac{1}{2}\begin{bmatrix} 0 & 0 & 0 & 0 & -j & j \\ 0 & 0 & 0 & 0 & 1 & j \\ 0 & 0 & 0 & 0 & 1 & 1 \\ 0 & 0 & 0 & 0 & -j & -1 \\ -j & 1 & 1 & -j & 0 & 0 \\ j & j & 1 & -1 & 0 & 0 \end{bmatrix} \tag{3.3}$$

In order to mathematically explain the principle of operation of the six-port receiver, the expression of the six-port output waves can be easily written as:

Table 3.1 Wave expressions at the output of the six-port junction

$b_1 = -j\frac{a_5}{2} + j\frac{a_6}{2}$	$b_2 = \frac{a_5}{2} + j\frac{a_6}{2}$
$b_3 = \frac{a_5}{2} + \frac{a_6}{2}$	$b_4 = -j\frac{a_5}{2} - \frac{a_6}{2}$

As a matter of fact, if we denote the RF modulated signal (a_6) and the coherent reference carrier (a_5) as [41]:

$$a_5 = a.e^{j(\omega_0 t + \varphi_5)} \tag{3.4}$$

$$a_6 = \alpha(t).a.e^{j(\omega_0 t + \varphi_6(t))} = a_5.\alpha(t).e^{j(\Delta\varphi(t))} \tag{3.5}$$

By replacing the expressions of a_5 and a_6 in the system of equations in Table 3.1, we obtain the following equations:

$$b_1(t) = -j\frac{a}{2}.e^{j(\omega_0 t + \varphi_5)}.\left[1 + \alpha(t).e^{\Delta\varphi(t)+\pi}\right] \tag{3.6}$$

$$b_2(t) = \frac{a}{2}.e^{j(\omega_0 t+\varphi_5)}.\left[1+\alpha(t).e^{\Delta\varphi(t)+\pi/2}\right] \tag{3.7}$$

$$b_3(t) = \frac{a}{2}.e^{j(\omega_0 t+\varphi_5)}.\left[1+\alpha(t).e^{\Delta\varphi(t)}\right] \tag{3.8}$$

$$b_4(t) = -j\frac{a}{2}.e^{j(\omega_0 t+\varphi_5)}.\left[1+\alpha(t).e^{\Delta\varphi(t)-\pi/2}\right] \tag{3.9}$$

It should be noted that the output dc signals are the results of connecting the four six-port circuit outputs to the power detectors (see Figure 3.1). We consider that the power delivered at the output of each ideal power detector is proportional to the square of the RF signal magnitude. Under these conditions

$$V_i(t) = K.b_i(t).b_i^*(t) \tag{3.10}$$

Thus, the dc output voltages can be expressed as [67]:

$$V_1(t) = K.\frac{a^2}{4}(1+\alpha^2(t)-2.\alpha(t).\cos(\Delta\varphi(t))) \tag{3.11}$$

$$V_2(t) = K.\frac{a^2}{4}(1+\alpha^2(t)-2.\alpha(t).\sin(\Delta\varphi(t))) \tag{3.12}$$

$$V_3(t) = K.\frac{a^2}{4}(1+\alpha^2(t)+2.\alpha(t).\cos(\Delta\varphi(t))) \tag{3.13}$$

$$V_4(t) = K.\frac{a^2}{4}(1+\alpha^2(t)+2.\alpha(t).\sin(\Delta\varphi(t))) \tag{3.14}$$

In order to generate quadrature signals I/Q, we use differential operational amplifiers at outputs 1, 3, and 2, 4. Hence, the in-phase and quadrature components at the output of OpAmps can be simply expressed as:

$$I(t) = A_G.(V_3(t) - V_1(t)) = K.a^2.A_G.\alpha(t).\cos(\Delta\varphi(t)) \tag{3.15}$$

$$Q(t) = A_G.(V_4(t) - V_2(t)) = K.a^2.A_G.\alpha(t).\sin(\Delta\varphi(t)) \tag{3.16}$$

We can define a complex vector using I(t) and Q(t) as follows:

$$\Gamma(t) = I(t) + jQ(t) = K.a^2.A_G.\alpha(t).e^{j\Delta\varphi(t)} \tag{3.17}$$

This complex vector is clearly a representation of the baseband modulated signal being received. Consequently, the six-port architecture is simpler than the classical homodyne/heterodyne counterpart. Moreover, it requires many orders of magnitude lower LO power when using zero-bias Schottky diode power detectors. For these reasons, the six-port receiver is one of the most promising direct conversion demodulators [68].

3.2 Dynamic range of six-port receivers

As illustrated by (3.10), the direct demodulation process requires the use of power detectors operating under the square law region regime. In practice, power detectors have a limited square law region, which means that the output voltage is proportional to the input RF power, only within a specific interval of input power. Outside this region, the output voltage can be expressed as an N^{th}-order polynomial expansion of the input power, and the obtained Γ vector is no longer a representation of the baseband modulated signal, because of the contribution of the high-order exponents [69]. Figure 3.2 illustrates the behavior for typical diode detectors, where an input power ranging from -40 dBm to -10 dBm is necessary to operate in the linear region the device, while at the same time being above the noise floor. Hence, the square law region for this detector

is about 30 dB. However, one can easily notice that the six-port junction presents at least 6 dB of loss (which should be higher in practice due to the loss within the substrate itself and loss of mismatching) in the dynamic range of the whole receiver if we take into account the fact that the RF signal must go through two couplers before being applied to the input of power detectors.

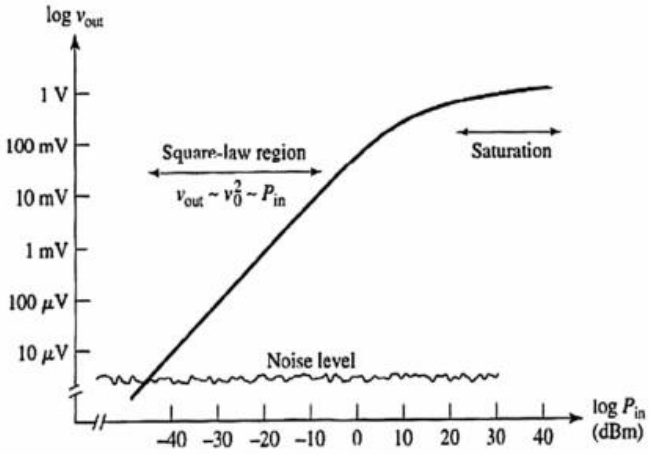

Figure 3.2 Square-law region for a typical diode detector

Consequently, in the case of high-speed communications, the AGC is not able to track the fast change of incoming RF signal power (i.e. every symbol period), and the dynamic range *Dr* is related to the width of the square law region of power detectors $W_{square\text{-}law\text{-}region}$ and the loss of the six-port junction (including the 6 dB loss previously explained), as [70]:

$$Dr = W_{square\text{-}law\text{-}region} - L_{junction} \quad \text{in dB} \tag{3.18}$$

If power detectors with the behavior as shown in Figure 3.2 are used, the dynamic range of the six-port receiver would be equal to *Dr* ~30-6 = 24 dB. It is worth mentioning that the example above is only for illustration purpose, and there are several commercial power detectors with up to 70 dB of square region (at microwave frequencies), which would result in six-port receiver with around 64 dB of dynamic range.

Such commercial power detectors are now available for microwaves but almost absent at millimeter waves due to the difficulty of their design and fabrication cost and especially because

millimeter waves have become recently a hot topic in research and industry as well, with the rise of 5G standard.

In fact, SPR with only 24 dB dynamic range as illustrated in Figure 3.2, are far from the 120 dB dynamic range of conventional heterodyne/super-heterodyne receivers. Using power detectors with wider square law region is always preferred for six-port receivers. However, in order to compete with conventional receiver architectures, the dynamic range of SPR must be enhanced to make it a good candidate for future wireless communications, and to improve its competitiveness against conventional receiver architectures.

3.3 Improvement of six-port receivers dynamic range

The limited square law region of power detectors, which are used for power reading in the multiport interferometer, is a challenging issue in the development of six-port receivers. To overcome this problem and provide better data rates, some solutions have been introduced and presented in the literature. One technique, for example, focuses on the linearization of power detectors using polynomials so that high-order modulations can be handled in the same way as QPSK and QAM-16 schemes

Abul Hasan et al. have highlighted the foundation of such a method and an experimental verification has been performed showing the possibility of demodulating QAM-64 with an average error vector magnitude (EVM) of 1.66% around a center frequency of 2.4 GHz [69]. Another scheme, which aims to control the diode bias through a blind algorithm to reduce the EVM, was proposed by Lima et al. [105].Moreover, Joakim Östh et al. presented a wideband six-port receiver, operating over a bandwidth of 1 GHz around the center frequency of 7.5 GHz, which is capable of offering data rates up to 1.7 Gb/s[85], with a bit error rate of 5.10^{-5} when applying an equalizer after the detection process while using conventional diode based power detectors. Although these approaches have been successful in demodulating high-order modulations, it is important to mention that complicated digital algorithms are used to mitigate the limited square law region of the diode based detectors. Therefore, the digital information contained in the RF signals is no longer treated in the analog domain, and the complexity and cost of the receiver are inherently increasing.

In this chapter, an alternative six-port based receiver architecture is proposed and studied aiming to increase the demodulation performances of SPR without the need for digital algorithms, while operating within narrow frequency bands, in order to avoid the memory effect of power detectors. In fact, the proposed dual SPR aims to mitigate the limited square law region of power detectors while keeping the all analog operation of six-port receivers. An experimental prototype is developed to validate the anticipated improvements of the six-port receiver performances.

3.3.1 Dual six-port receiver architecture

The proposed architecture is introduced to increase the six-port receiver dynamic range, which allows a direct demodulation of high order modulations. In fact, a received amplified RF signal is equally split using a Wilkinson power divider as depicted in Figure 3.3. The first of the twin signals is processed by first six-port circuit SP1 in a rather conventional manner. On the other hand, the second of the twin RF signals passes through an attenuator, with a fixed attenuation Att which is equal to the width of the detectors square law region, before being demodulated by the second six-port SP2. Hence, the first six-port SP1 would be responsible of demodulating the constellation symbols received at energy level P_1 satisfying the following condition.

$$\left|P_1 - P_{carrier}\right| \leq D \quad \text{in dB} \tag{3.19}$$

where $P_{carrier}$ refers to the RF carrier power in dBm, and D denotes the width of the power detector square law region in dB. On the other hand, SP2 would be in charge of processing symbols received at power levels P2 satisfying the following condition.

$$D \leq \left|P_2 - P_{carrier}\right| \leq 2D \quad \text{in dB} \tag{3.20}$$

Introducing an attenuator Att at the input of SP2 is necessary to reduce the power level P_2 so that it can be processed within the square law region of power detectors. Followed by SP2, the dc voltages at the output will be simply amplified in the baseband by an operational amplifier A2, where A2 would be greater than A1 in order to compensate the attenuator effect. In this way, both

six-ports will instantaneously demodulate different points of the complex constellation. To overcome reading overlapped signals, DC voltage limiters [V1,V2] are added at the output of power detectors in order to create a partition of the symbols processed by SP1 and SP2. Indeed, the goal of adding the DC voltage limiters is to divide the demodulation task between SP1 and SP2 so that it appears that each is related to a different area in the complex plane. It is also important to mention that if the constellation size is bigger, the proposed architecture could be extended and another six-port circuit SP3 should be added in series with an attenuator Att' to handle the remaining symbols of the constellation. According to the proposed approach, there is no need to apply any digital algorithm to either linearize the behavior of power detectors, or to control the biasing point of diode detectors in order to follow the RF signal dynamic range. As a consequence, the proposed scheme enables keeping the all analog treatment of digital signals which is the main feature of six-port demodulators.

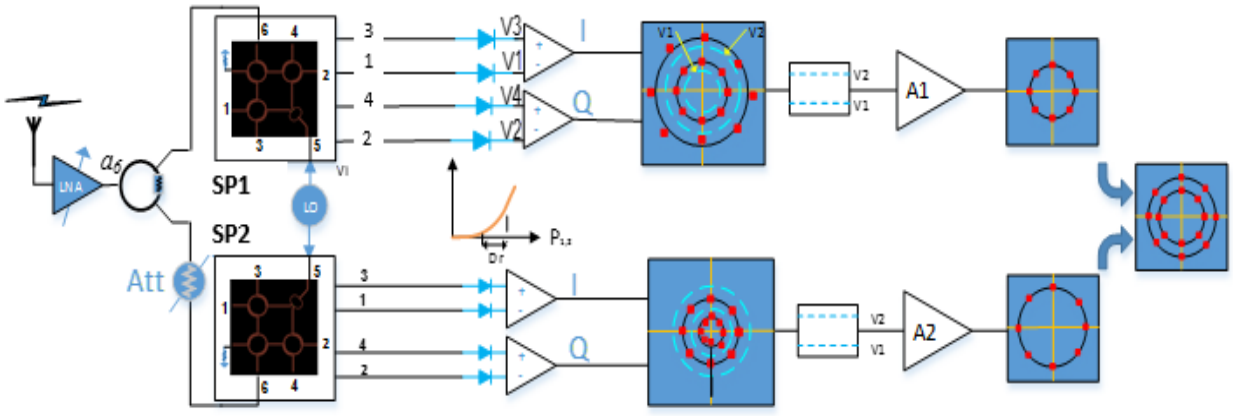

Figure 3.3 Schematic description of the proposed architecture

3.3.2 Experimental results

In order to experimentally validate the performances of the dual six-port receiver architecture, a six-port junction is designed with Advanced Design System ADS of Keysight, using Rogers laminates 6002 with a dielectric permittivity ε_r =2.94 and thickness of 0.5 mm. As depicted in Figure 3.4(a), the six-port junction is designed to operate around the center frequency of 5 GHz is composed of one Wilkinson power divider and three hybrid-90^o couplers, and the fabricated six-port junction is shown in Figure 3.4(b). The simulation results for S parameters for input ports 6

are given in Figure 3.5. The measured magnitude and phase of S-parameters are given by Figure 3.6 and 3.7, respectively. The good measurement results in terms of power division and phase distribution between output ports are a good indicator of the performance of the whole SPR.

The squaring function needed to recover the baseband signal was performed by using eight power detectors (ZX47-60-S+) made by Mini-Circuits.

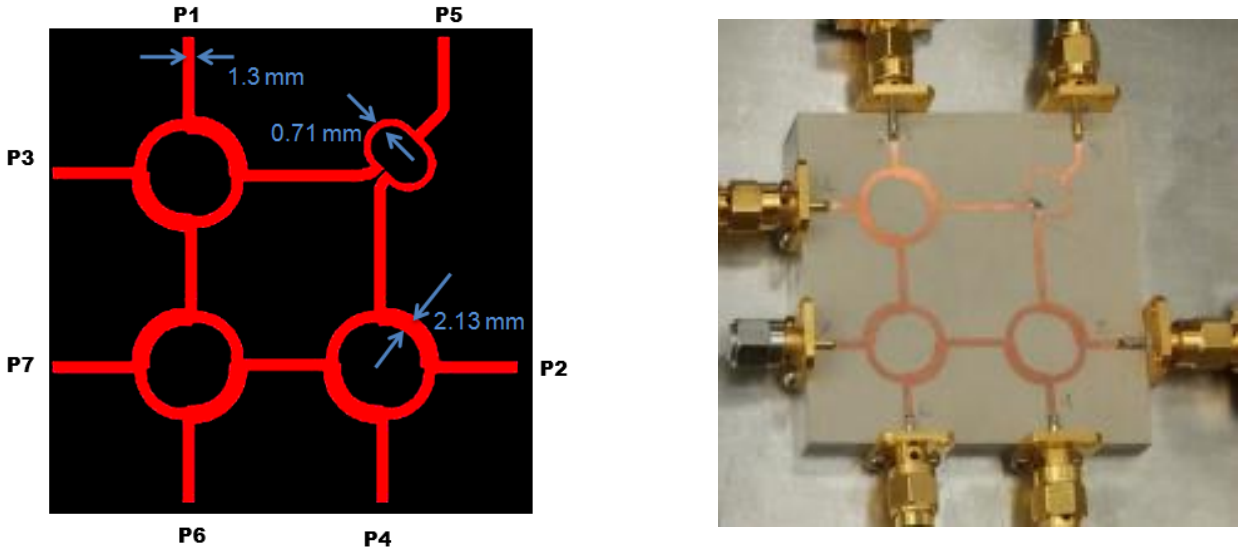

(a) (b)

Figure 3.4 (a) ADS layout of the six-port junction (b) Fabricated six-port junction

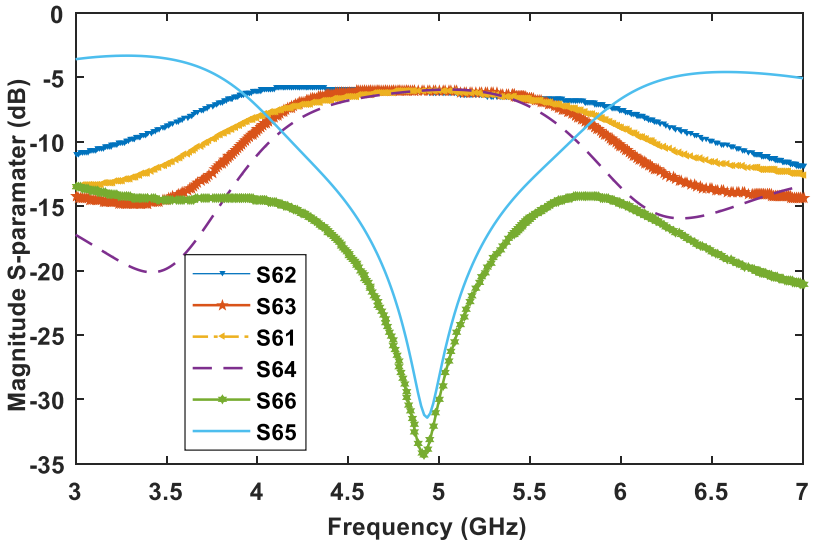

Figure 3.5 Simulated S-parameters magnitude with port 6 as input

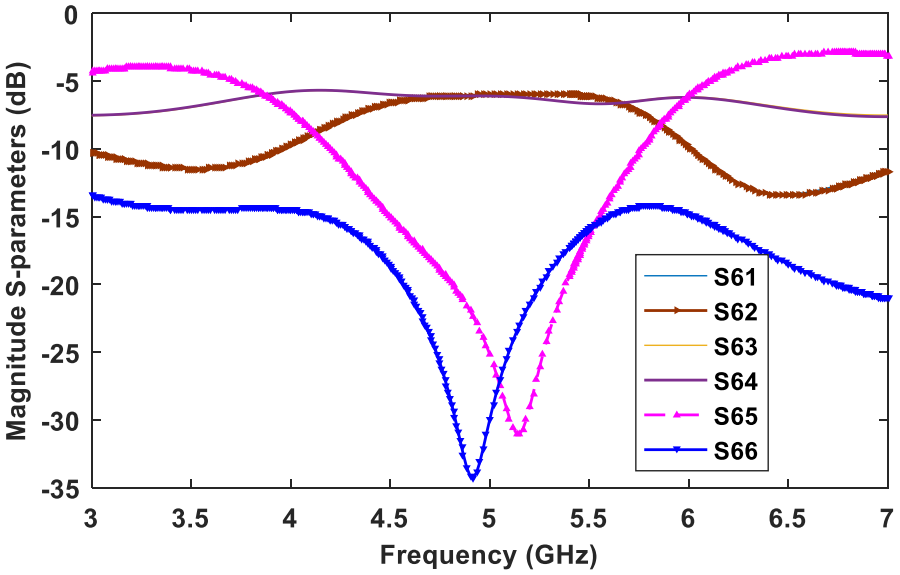

Figure 3.6 Measured S-parameters magnitude with port 6 as input

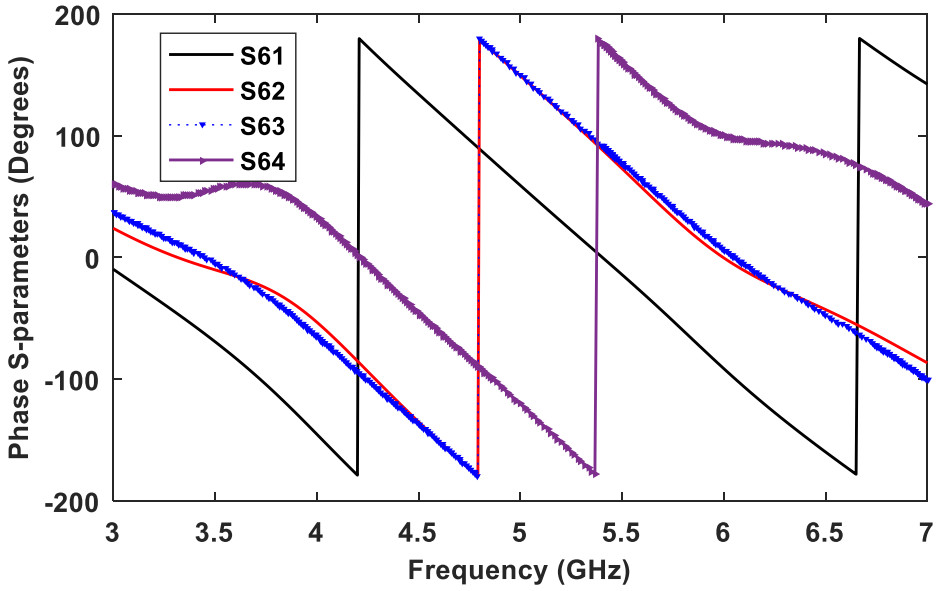

Figure 3.7 Measured S-parameters phase with port 6 as input

Two Agilent digital oscilloscopes were used to visualize the demodulation results through theirs X-Y functionality and a set of measurements were conducted at 5 GHz at a data rate of 1 MS/s with LO power of -20 dBm.

First, a modulation scheme following Gray Code was defined. In fact, a constellation of four rings was constructed. Each ring is composed of eight symbols. The inner two rings contain symbols which satisfy (3.19). These symbols are received at power levels less than D_r dB above the RF carrier. Hence, they are treated within the square law region of power detectors, namely by the junction SP1. The outer two rings are set in such a way that the symbols they contain are received with power levels more than D_r dB above the RF carrier as highlighted by (3.20). Hence, they are processed by SP2 after being attenuated.

The inner rings radii were set to 0.5 and 1 and the outer two rings radii were chosen to be 2.5 and 3. Thus, the symbols of the outer rings would have power levels which are at least 10 dB more than those of the inner rings. Hence, this constellation scheme enables us to highlight the distortion effect caused by the non-linearity of power detectors. In order to quantify the claims about the total receiver dynamic range improvement, the EVM is computed for the received constellation (as shown by the averaged received constellation points in Figure 3.8) using a set of 10^6 symbols sent randomly and it has been shown that EVM is reduced from 16.73% when using the conventional six-port circuit to 2.01% in the case of the proposed approach. A comparison of the EVM enhancement through the use of the solutions reported in the literature is given by Table 3.2, shows almost the same order of magnitude improvement with the proposed method [71].

Table 3.2 EVM improvement through the use of linearization, bias-control and the proposed dual six-port receiver

	Proposed solution	**Frequency band**	**EVM improvement**
[69]	Linearization	2.4 GHz	7.93 % to 1.66 %
[105]	Bias-control	Simulink model	6.3 % to 1.6 %
This work	Proposed approach	5 GHz	16.73 % to 2.01%

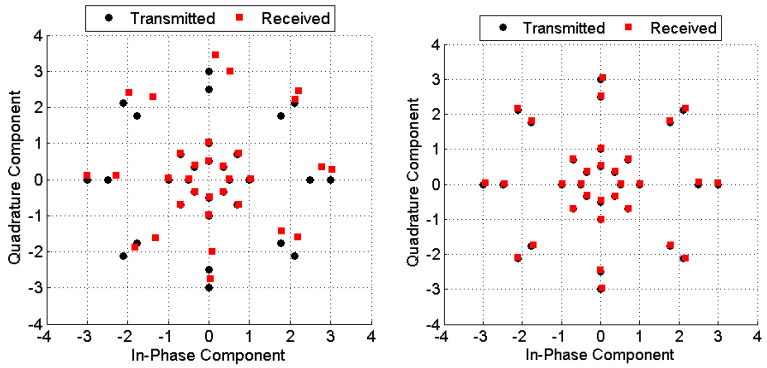

(a) (b)

Figure 3.8 (a) received constellation using one single six-port circuit, (b) received constellation using the proposed dual six-port architecture

3.4 Conclusion

In this chapter, a novel dual six-port receiver is presented. The new architecture is introduced in order to double the dynamic range of the whole receiver, which has been always limited by the reduced square law region of power detectors. The EVM is evaluated for the single six-port receiver and for the proposed scheme and it is demonstrated that there is a substantial improvement from 16.73% to 2.01%. Hence, the proposed scheme could be a good alternative for six-port-based sensing applications and higher data rates communication systems requiring a higher dynamic range.

CHAPTER 4 INTERFEROMETER BASED ANGLE OF ARRIVAL DETECTION SYSTEM

This chapter presents an interferometer-based direction of arrival (AoA) detection system. Unlike conventional six-port based phase discriminators, the proposed architecture uses only three couplers in combination with three receiving antennas. The modeling and analysis of the AoA detection scheme prove that it is possible to increase the measurement accuracy by increasing the inter-element distance between the receiving antennas. The proposed scheme is suitable for use at 5G millimeter wave frequencies as the wavelength is less than one centimeter and many antennas could be easily integrated within the receiver.

4.1 Importance of AoA detection

For many wireless communication and sensing systems, the knowledge of the Angle of Arrival (AoA) of an incoming RF signal is of great importance [72]. For instance, military radars are expected to detect with high accuracy the position, speed as well as azimuth/elevation coordinates of special targets based on the information contained within a backscattered wave signal [2]. New robots are also capable of moving and interacting with their environment without the need of any external remote control, which means that these robots must detect AoA of RF signals in order to increase their awareness of what and where is around them [73]. Moreover, with the emergence of next generation of wireless systems including 5G and the migration towards millimeter waves, it has been demonstrated that high-gain and beam-steering antenna arrays have to be used in order to combat the huge path loss at these frequencies. However, it has been proved through measurement campaigns that a small deviation of either transmitter or receiver may result in a loss of the communication link [74]. Hence, future wireless transceivers intended to be used at mm-wave frequencies must be capable of detecting AoA of an incoming RF signal on the fly with expected link efficiency [75].

Classic AoA detection systems are usually based on mixing architectures which require high local oscillator power [76]. These systems would be very fragile and expensive at higher

frequencies. To overcome the constraints of cost and power consumption while achieving high accuracy in connection with AoA detection, six-port interferometers have been used in order to measure the phase difference of an incoming RF signal. Then, a simple trigonometric derivation is applied in order determine AoA of the incident electromagnetic wave [76]. In fact, the six-port interferometer AoA detection system requires low LO power as it makes use Schottky-diode power detectors operating under their square law region. Moreover, the six-port passive circuit can be made broadband, which is an attractive feature for future wireless systems operating at mm-waves. In this chapter, a new interferometry-based AoA detection system is proposed, which inherits the same advantages of conventional six-port phase measurement circuits, and is composed of three hybrid couplers and three antennas instead of a four couplers junction and two antennas for six-port AoA detection systems.

4.2 Phase measurement principle

The block diagram of the proposed AoA detection system is depicted in Figure 4.1. It is composed of one hybrid-90^o coupler, two rat-race couplers, and three receiving antennas arranged with an equal inter-element distance *d*. In addition, four Schottky-diode based power detectors, operating under their square law-region, are used to generate DC voltages proportional to the magnitude of RF signals at their input. These voltages are then combined to estimate the angle of arrival of the incident electromagnetic wave using a simple trigonometric formula. It must be noticed that the proposed interferometer does not require any external LO reference signal.

In fact, if we consider the incident waves (after amplification through LNA, as power detectors have some minimum detectable power threshold to operate properly) at three antennas to be expressed as:

$$\psi_1 = a.\exp(j(2\pi ft + \Delta\varphi)) \tag{4.1}$$

$$\psi_2 = a.\exp(j2\pi ft) \tag{4.2}$$

$$\psi_3 = a.\exp(j(2\pi ft - \Delta\varphi)) \tag{4.3}$$

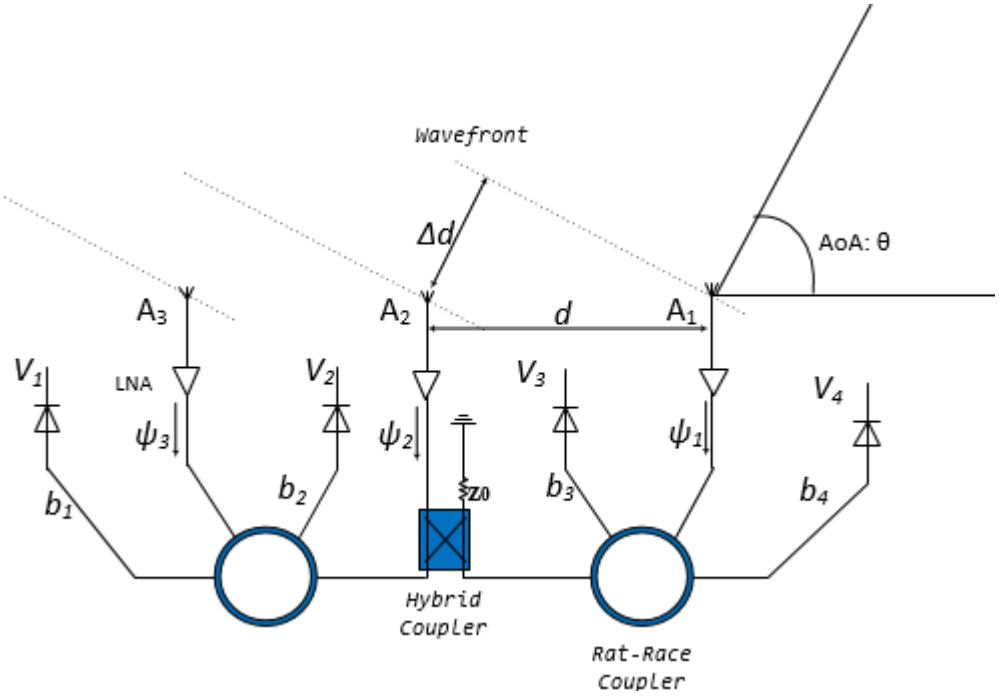

Figure 4.1 Block diagram of the proposed interferometer AoA detection system

where a and f are the amplitude and frequency of the incident wave respectively, and $\Delta\varphi$ is the phase difference between wave fronts at the receiving antennas and is expressed as follows:

$$\Delta\varphi = 2\pi\Delta d / \lambda = 2\pi d \sin(\theta) / \lambda \tag{4.4}$$

where Δd is the walking distance difference between the waves at consecutive receiving antennas, and λ is the wave-length relative to the frequency f, and θ is the angle of arrival of the incident wave with respect to the azimuth plane. The four signals (bi, i=1..4) created at the outputs of the interferometer are expressed as:

$$b_1 = \frac{a.\exp(\,j(2\pi ft - \Delta\varphi))}{\sqrt{2}} + \frac{j.a.\exp(\,j2\pi ft)}{2} \tag{4.5}$$

$$b_2 = \frac{a.\exp(\,j(2\pi ft - \Delta\varphi))}{\sqrt{2}} - \frac{j.a.\exp(\,j2\pi ft)}{2} \tag{4.6}$$

$$b_3 = \frac{a.\exp(\,j(2\pi ft + \Delta\varphi))}{\sqrt{2}} - \frac{.a.\exp(\,j2\pi ft)}{2} \tag{4.7}$$

$$b_4 = \frac{a.\exp(\,j(2\pi ft + \Delta\varphi))}{\sqrt{2}} + \frac{.a.\exp(\,j2\pi ft)}{2} \tag{4.8}$$

As mentioned earlier, the four power detectors operating under their square law region are used to generate dc voltages proportional to the magnitude of RF signals at their input, which read as follows:

$$V_1 = \frac{K.a^2}{2}\left(\frac{3}{2} - \sqrt{2}.\sin(\Delta\varphi)\right) \tag{4.9}$$

$$V_2 = \frac{K.a^2}{2}\left(\frac{3}{2} + \sqrt{2}.\sin(\Delta\varphi)\right) \tag{4.10}$$

$$V_3 = \frac{K.a^2}{2}\left(\frac{3}{2} - \sqrt{2}.\cos(\Delta\varphi)\right) \tag{4.11}$$

$$V_4 = \frac{K.a^2}{2}\left(\frac{3}{2} + \sqrt{2}.\cos(\Delta\varphi)\right) \tag{4.12}$$

Finally, the phase difference $\Delta\varphi$ could easily be computed using the obtained dc voltages as follows:

$$\Delta\varphi = \arctan\left(\frac{V_2 - V_1}{V_4 - V_3}\right) \tag{4.13}$$

4.3 Ambiguity analysis

By substituting equation (4.13) into equation (4.4), we generate a direct formula linking the incident wave angle of arrival θ to the four dc voltages at the output of the proposed interferometer:

$$\theta = a\sin(\frac{\lambda\Delta\varphi}{2\pi d}) = a\sin\left(\frac{\lambda}{2\pi d}.a\tan(\frac{V_2 - V_1}{V_4 - V_3})\right) \quad (4.14)$$

Thus, the angle of arrival θ is expressed as a nonlinear function of the four dc voltages and the inter-element distance d. In [77], G. Vinci et al. have studied the behavior of such function and demonstrated that there is a possible ambiguity on AoA computation. In fact, the key factor that expands or stretches the unambiguity range of the arc sine function is the inter-element distance *d*. For an inter-element distance $d=0.5\lambda$, the proposed interferometer is capable of determining any angle of arrival within the interval [-30°,30°]. If the angle of arrival is greater than 30°, the phase obtained through the proposed AoA detection system would fall within the ambiguity range because of a repetition pattern of the arc sine function as depicted in Figure 4.2.

If the inter-element distance is chosen to be a greater value ($d=4\lambda$), the ambiguity-free range would be stretched to the interval [-3.5°; 3.5°] which is demonstrated with the simulation results in Figure 4.3.

Consequently, an initial guess of AoA could be determined within ±30° by choosing $d=0.5\lambda$. Then, the obtained value for the angle of arrival could be better evaluated using another antenna couple having a greater inter-element distance $d=4\lambda$, which bounds AoA to be within the interval [-3.5°; 3.5°].

If more accuracy is needed, d must be increased to the required degree of precision (Table 4.1). It must be noticed that this process is ultimately possible and suitable for millimeter-wave communication systems where a large number of fingernail antennas could be integrated within a very small area as the wavelength is as small as 5 mm at 60 GHz, and eventually the AoA can be

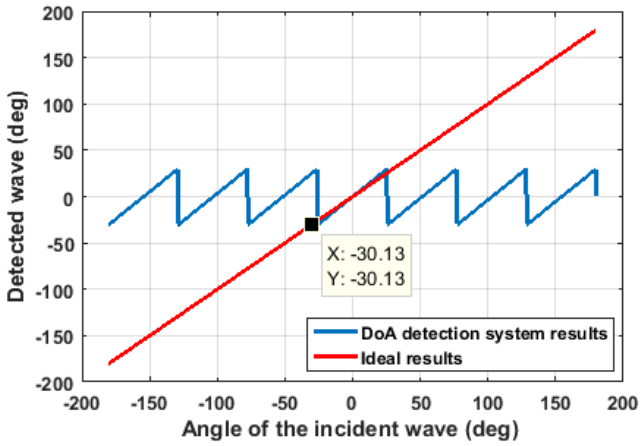

Figure 4.2 Simulation results for the detected AoA (d=0.5λ)

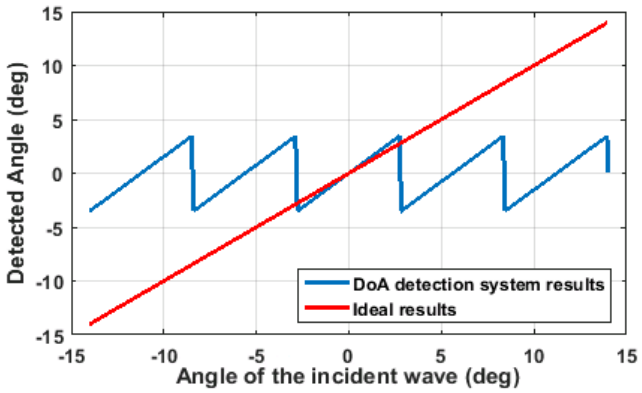

Figure 4.3 Simulation results for the detected AoA (d=4λ)

determined within ± 1.8^o if we choose antennas having an inter-element distance of 4 cm (8λ) which is quite reasonable from a practical point of view.

Table 4.1 Ambiguity-free range as a function of the inter-element distance *d*

Inter-element distance	**Unambiguity interval**
0.5λ	[-30^o ; 30^o]
Λ	[-14.4^o ; 14.4^o]
4λ	[-3.5^o ; 3.5^o]
8λ	[-1.8^o ; 1.8^o]

4.4 Conclusion

A new AoA detection system has been proposed in this chapter. It is based on the use of an interferometer circuit composed of three antennas and three couplers. The key features of this system are its robustness, low-cost and freedom from any LO signal while offering a high accuracy when measuring the direction of arrival of an unknown RF signal. The degree of precision for the AoA measurement can be augmented by increasing the inter-element distance to be on the order of few wavelengths. Thus, the proposed system could be a promising technique for next generation of wireless systems (including 5G) operating at millimeter waves.

CHAPTER 5 SPATIALLY DISTRTIBUTED MULTI-INPUT INTERFEROMETER RECEIVER ARCHITECTURE: ANAYLSIS AND SIMULATIONS

This chapter introduces a novel spatially distributed multi-input direct conversion receiver architecture based on interferometric correlations of wave signals for 5G systems and beyond. The proposed receiver scheme inherits the advantages of conventional six-port receivers, while reducing the internal SPR junction loss. The spatially distributed multi-input architecture is based on the use of a set of equally spaced four antenna elements instead of using a six-port junction composed of four hybrid couplers or other alternative circuit-based topologies. The mathematical modeling of the proposed receiver is derived and presented, in combination with simulation results covering different aspects such as coupling effect, carrier frequency effect, and BER as a function of angle of arrival.

5.1 Overview of conventional receivers' architectures and limitations

The exponential growth of data traffic that is facing today's 3G and 4G operators has urged the international regulatory agencies like Federal Communications Commission (FCC) and the International Telecommunications Union (ITU) to create special focus groups such as IMT-2020 in order to establish the technical recommendations and general guidelines to be adopted through the fifth generation (5G) of wireless systems [78].

In fact, emerging wireless communication standards are required to support the transmission of data rates in the order of multiple Gb/s with a latency of less than 1 millisecond [79]. In order to accommodate the challenging requirements and technical specifications for better performances in 5G systems, the whole network architecture has been redrawn. Indeed, the concept of Ultra Dense Networks (UDNs) has been introduced which stands for the deployment of multiple base stations and access points within the same area to get as close as possible to the end user [80].
Moreover, the whole backhauling system that enables fast and point-to-point communications between access nodes must be deployed wirelessly to avoid the well-known prohibited cost of fiber optics interconnectivities [81]. In addition, the energy consumption, the digital signal

processing requirements and the cost per unit access point within the wireless backhauling system must be decreased as much as possible to enable large scale deployment and easy penetration of the emerging technology into the market. Consequently, novel RF front-ends must be revisited, studied and validated in order to accommodate the aforementioned strict requirements concerning emerging 5G systems and beyond, including point-to-point communications between access points or fixed last mile entities of the backhauling network.

Many RF front-ends for backhauling and point-to-point communications purposes have been introduced and studied in literature. In [82], a novel front-end with high directivity and self-beam/null steering was presented, which operates at 2.4 GHz, enabling point-to-point communications while focusing on reducing the probability of intrusion and unwanted interception. Another low-cost smart antenna receiver subsystem operating over E-Band was introduced in [83]. This front-end is based on a beam-switching scheme, implemented through an SIW Butler matrix, which alleviates the problem of possible mismatch between highly directive 60 GHz antennas, and hence presents an excellent candidate for short range point-to-point communications.

A highly efficient digital baseband receiver was also presented in [84]. The proposed receiver is mainly based on an analog symbol timing recovery as well as digital carrier recovery. This prototype can provide data rates of about 5 Gb/s using 16-QAM in E-band with an optimal bit error rate of about 10^{-10}, but the heterodyne nature of this receiver as well as the complexity of its architecture would increase its cost and energy consumption.

Six-port direct conversion receivers, with conventional architecture as depicted in Figure 5.1, have shown promising capabilities since their first introduction in 1994. In fact, the six-port receiver architecture is cost effective and compact size which enables high data rates while requiring less LO power than conventional heterodyne receivers. However, the six-port receiver suffers from some crucial features, like its limited dynamic range when compared to the classic (homodyne/heterodyne) mixer-based receiver. The dynamic range of six-port receivers is directly linked to the width of the square law region of power detectors which depends on the characteristics of the diode/transistor being used for power detection. Moreover, the maximum symbol rate in six-port receivers is inversely proportional to the rise time of power detectors.

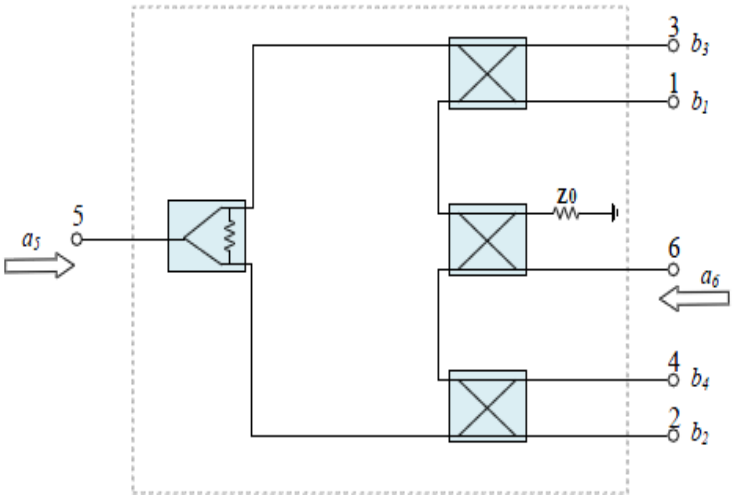

Figure 5.1 bloc diagram of conventional six-port circuit

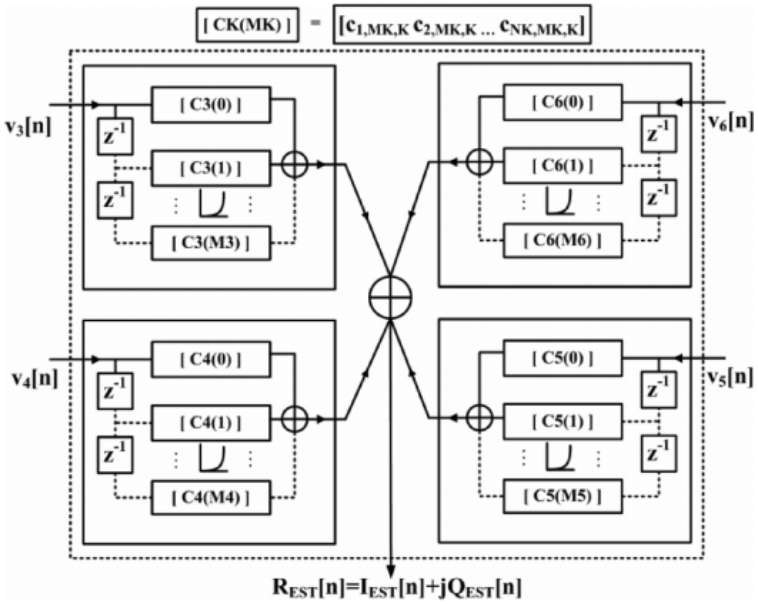

Figure 5.2 Proposed model for an SPR system taking into account all the identified system impairments [69].

In [69], a modeling and calibration method for a wideband six-port junction operating from 2 to 18 GHz is presented as shown in Figure 5.2, which is based on the linearization of power detectors, and the mitigation of the six-port junction amplitude and phase imperfections. In fact, six-port circuits always suffer from non-flat frequency response over the whole bandwidth

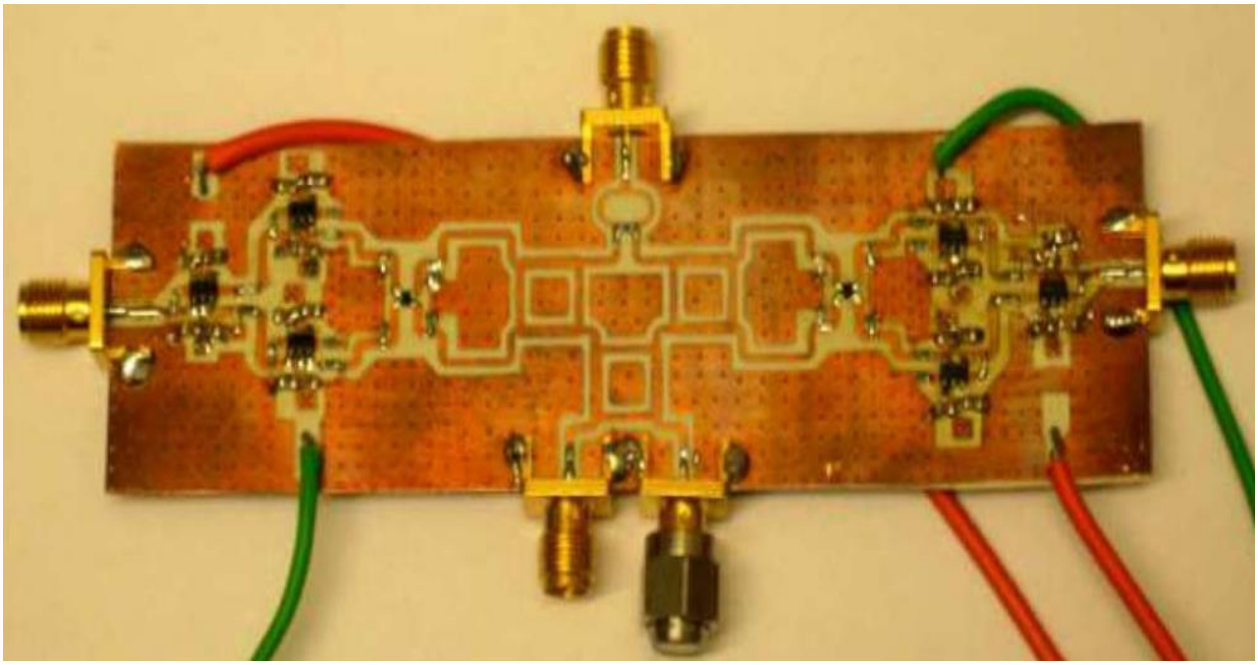

Figure 5.3 Photograph of the prototype demodulator [85]

(unequal power divisions for the power dividers and hybrids, and deviation of phase differences from ideal 90^{o} for the hybrids in the whole band of operation), which limits the frequency of operation of the whole circuit. As illustrated by Figure 5.3, another wideband (7-8 GHz) six-port demodulator is introduced in [85], which is operating at a data rate of 1.25 Gb/s, with an overall EVM of 10.7% when using 16-QAM with fast power detectors having a rise time of about 2 ns.

In this chapter, we propose a novel receiver architecture, which is based on spatially distributed multi-input interferometric correlations for derivations and development of low-cost, low-complexity direct conversion RF receiver for backhauling and point-to-point communications operating at 5 GHz. In fact, the proposed receiver inherits the same advantages of conventional six-port demodulators as reported in literature [86]-[91].

However, the proposed front-end is capable of demodulating digital signals without the need of the classic interferometer circuit, while using the same simple algorithm of I/Q signals regeneration. In addition, a number of other advantages can be anticipated such as low-loss and high efficiency reception at millimeter-wave frequencies.

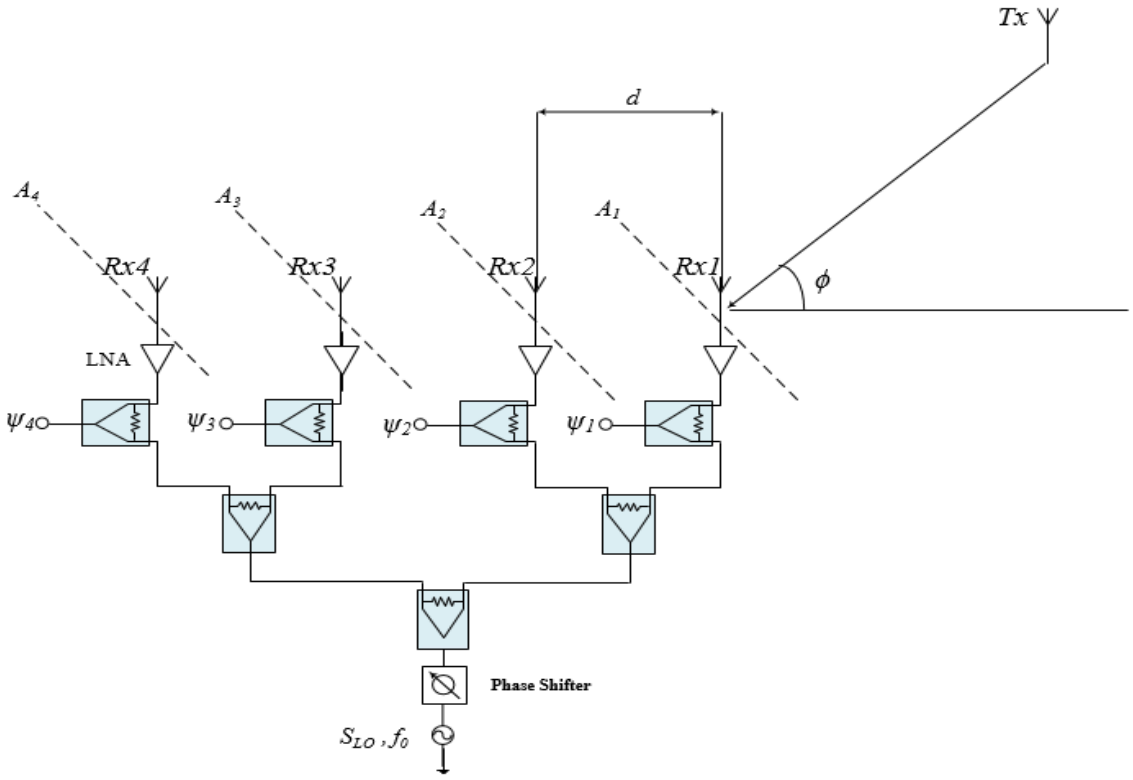

Figure 5.4 Schematic of the proposed spatially distributed multi-input receiver

5.2 Spatially distributed multi-input interferometer receiver

5.2.1 Receiver architecture

The block diagram of the proposed direct conversion receiver is depicted in Figure 5.4. It is composed of four antennas (*Rx1*, *Rx2*, *Rx3* and *Rx4*) with a constant inter-element distance *d*. Each antenna would receive a phased version of the same RF modulated signal being sent by the transmitter *Tx*. The phase difference β between received signals at two consecutive antennas is a function of the angle of arrival ϕ, the inter-element distance d, as well as the wavelength λ_0 relative to operating frequency f_0 of the system, and it can be expressed as:

$$\beta = 2\pi d \cos(\phi) / \lambda_0 \tag{5.1}$$

Let us consider the normalized received RF modulated signal $A_1(t)$ at antenna *Rx1* (after low-noise amplifier LNA) and the local oscillator signal $S_{LO}(t)$ to be defined as:

$$A_1(t) = \alpha(t).a.\exp(j(2\pi f_1 t + \theta(t))) \tag{5.2}$$

$$S_{LO}(t) = a.\exp(j(2\pi f_2 t + \theta_0)) \tag{5.3}$$

where $\alpha(t).\exp(j(\theta(t))$ is the instantaneous baseband modulated signal to be transmitted, which is modulated in amplitude and phase by $\alpha(t)$ and $\theta(t)$, respectively. The carrier signals used at the transmitter and receiver are given by $a.\exp(j(2\pi f_1 t))$ and $a.\exp(j(2\pi f_2 t + \theta_0))$, with a phase difference θ_0.

In the case of coherent demodulation, which is the topic of our study, the frequencies of the carriers at transmitter and receiver are equal ($f_1 = f_2 = f$). In the remaining of this chapter, we are only dealing with coherent demodulation, with an additional simulation study of the effect of carrier frequency offset on the performances of the receiver.

After passing through LNAs, the normalized signals at antennas *Rx2, Rx3* and *Rx4* can be expressed as:

$$A_2(t) = A_1(t).\exp(-j\beta) \tag{5.4}$$

$$A_3(t) = A_1(t).\exp(-2j\beta) \tag{5.5}$$

$$A_4(t) = A_1(t).\exp(-3j\beta) \tag{5.6}$$

And if the angle of arrival ϕ is fixed to make β equal to $\pi/2$, then after combining the received RF signals at the four antennas with the same reference LO following the circuit scheme presented in Figure 5.4, the four waves$(\psi_i(t), i = 1,2,3,4)$ at the input of the power detectors can be expressed as:

$$\psi_1(t) = \frac{A_1(t)}{\sqrt{2}} + \frac{S_{LO}(t)}{2\sqrt{2}} = \frac{a.\exp(\,j(2\pi ft + \theta_0))}{\sqrt{2}}.\left(\frac{1}{2} + \alpha(t).\exp(\,j\Delta\theta(t))\right) \tag{5.7}$$

$$\psi_2(t) = \frac{A_1(t).\exp(-j\frac{\pi}{2})}{\sqrt{2}} + \frac{S_{LO}(t)}{2\sqrt{2}} = \frac{a.\exp(\,j(2\pi ft + \theta_0))}{\sqrt{2}}.\left(\frac{1}{2} + \alpha(t).\exp(\,j\Delta\theta(t) - \frac{\pi}{2})\right) \tag{5.8}$$

$$\psi_3(t) = \frac{A_1(t).\exp(-j\pi)}{\sqrt{2}} + \frac{S_{LO}(t)}{2\sqrt{2}} = \frac{a.\exp(\,j(2\pi ft + \theta_0))}{\sqrt{2}}.\left(\frac{1}{2} + \alpha(t).\exp(\,j\Delta\theta(t) - \pi)\right) \tag{5.9}$$

$$\psi_4(t) = \frac{A_1(t).\exp(-j\frac{3\pi}{2})}{\sqrt{2}} + \frac{S_{LO}(t)}{2\sqrt{2}} = \frac{a.\exp(\,j(2\pi ft + \theta_0))}{\sqrt{2}}.\left(\frac{1}{2} + \alpha(t).\exp(\,j\Delta\theta(t) - \frac{3\pi}{2})\right) \tag{5.10}$$

where $\Delta\theta(t)$ is defined as the phase difference between the LO reference signal and $A_1(t)$

$$\Delta\theta(t) = \theta(t) - \theta_0 \tag{5.11}$$

In order to obtain baseband voltages proportional to the power of RF signals ($\psi_i(t), i = 1,2,3,4$), four power detectors are connected to the output combining ports of Wilkinson couplers. As it is known, the instantaneous dc output voltage of an ideal power detector is proportional to the square magnitude of the RF signal at its input.

$$V_i(t) = K_i\left|\psi_i(t)\right|^2, i = 1,2,3,4 \tag{5.12}$$

where K_i are constants measured in V/W. If the four power detectors are identical ($K_i = K, i = 1,2,3,4$), the output voltages can be expressed as:

$$V_1(t) = \frac{K.a^2}{2}\left(\frac{1}{4} + \alpha(t)^2 + \alpha(t).\cos(\Delta\theta(t))\right) \tag{5.13}$$

$$V_2(t) = \frac{K.a^2}{2}\left(\frac{1}{4} + \alpha(t)^2 + \alpha(t).\sin(\Delta\theta(t))\right) \tag{5.14}$$

$$V_3(t) = \frac{K.a^2}{2}\left(\frac{1}{4} + \alpha(t)^2 - \alpha(t).\cos(\Delta\theta(t))\right) \tag{5.15}$$

$$V_4(t) = \frac{K.a^2}{2}\left(\frac{1}{4} + \alpha(t)^2 - \alpha(t).\sin(\Delta\theta(t))\right) \tag{5.16}$$

Using these voltages, we can define a complex vector $\Gamma(t)$ by:

$$\begin{aligned}\Gamma(t) &= I(t) + jQ(t) \\ &= (V_1(t) - V_3(t)) + j(V_2(t) - V_4(t)) \\ &= \alpha(t).K.a^2.\exp(j\Delta\theta(t))\end{aligned} \tag{5.17}$$

It can be clearly observed that the magnitude of the defined $\Gamma(t)$ vector is proportional to the amplitude of the transmitted baseband signal, namely $\alpha(t)$ and if the phase of the LO reference is adjusted through the use of a phase shifter, in order to make $\theta_0 = 0^o$, $\Gamma(t)$ is going to be a representation of the modulated digital signal sent by the transmitter *Tx* and is simply given by:

$$\Gamma(t) = \alpha(t).K.a^2.\exp(j\theta(t)) \tag{5.18}$$

It must be noted that the obtained analytical expression of the complex vector is the same used in the classical six-port receiver theory [92-98].

5.2.2 Choice of the inter-element distance

As stated in the previous paragraph, the proposed receiver requires RF signals at the described antennas to be phase shifted by 90°. Hence, β as defined by (5.1) must be equal to $\pi/2$ when $\phi = \phi_{90}$.

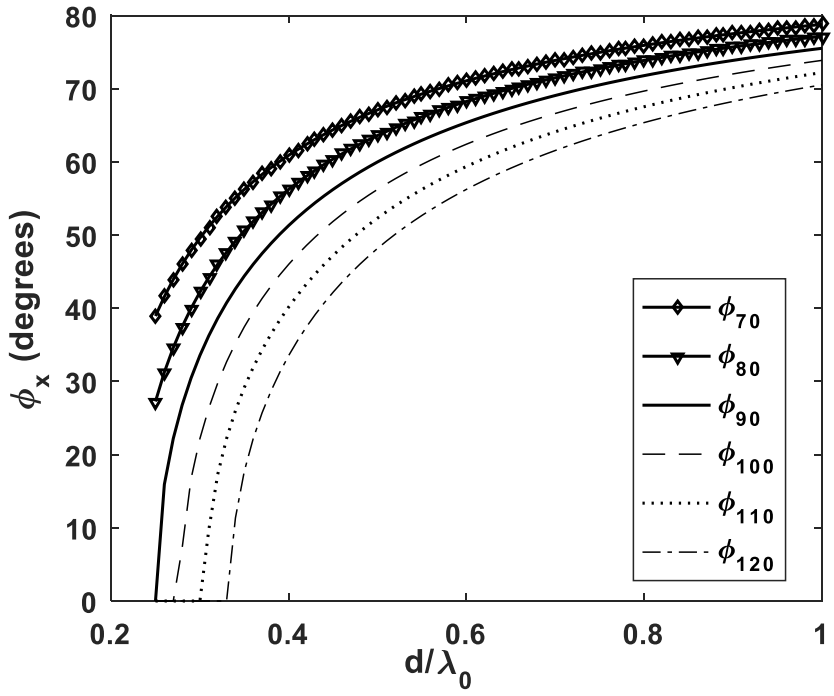

Figure 5.5 ϕ_x as a function of the inter-element distance

$$\beta = 2\pi d \cos(\phi_{90}) / \lambda_0 = \pi / 2 \tag{5.19}$$

Hence, ϕ_{90} can be expressed as:

$$\phi_{90} = \arccos(\lambda_0 / 4d) \tag{5.20}$$

The curves of ϕ_x (the angle of arrival that makes β equal to x degrees) as a function of the ratio is d/λ_0 is given by Figure 5.5. It can be concluded that there is a constraint regarding the choice of the inter-element distance d, namely:

$$d \geq \lambda_0 / 4 \tag{5.21}$$

If the inter-element distance d is chosen to be $0.75\lambda_0$, then the angle at which $\beta=90^0$ is $\phi_{90}=70^o$. Although the proposed system is intended to be used for wireless fixed point-to-point communications, where it is easy to fix the angle at which $\beta=90^0$, it is worth mentioning that it is always possible to include variable phase shifters at the input of four antenna elements, as shown in Figure 5.6. These variable phase shifters would be in charge of getting the required 90^o phase shift, between received signals at the input of four antennas.

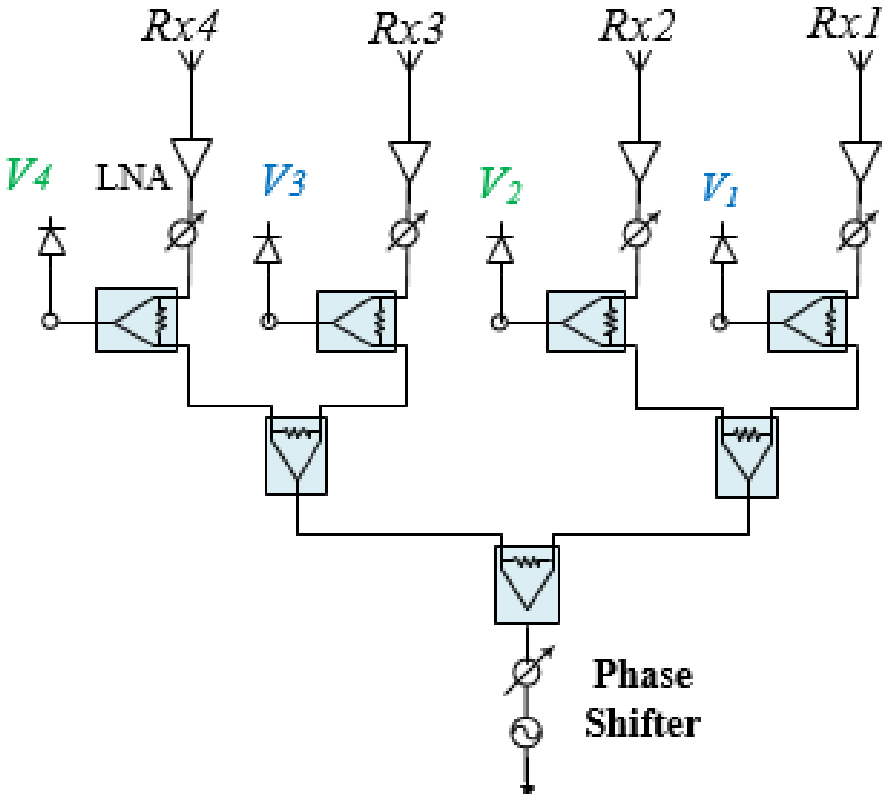

Figure 5.6 Block diagram of the proposed signal demodulator with phase shifters

Then, by using variable phase shifters, it would be possible to receive signals regardless the angle of arrival of the transmitted signal.

Moreover, a second row of four antenna elements (operating around another frequency band for example) could be implemented on top of the first one, which would create a dual-band receiver. And, from a conceptual point of view, more rows; each composed of four elements could be also implemented in two dimensions (2D), where each row has its own reference LO circuit.

It is worth mentioning that in some scenarios including 5G applications, high gain antennas are required at the receiver side, in order to amplify weak signals suffering, either from huge path loss, like in the case of millimeter-waves, or simply to reduce the interference level (as opposed to low gain antennas with wide beamwidth that capture unwanted signals coming from many directions) [99]. If such high gain antennas are to be implemented within the proposed receiver, it is needed to use beam-steering techniques, in order to capture signals, only from the required direction of arrival (ϕ_{90}) and reduce potential interference signals coming from unwanted directions. Moreover, digital interference cancellation techniques can also be applied to combat in-band interference signals from the same direction ϕ_{90} [100].

5.3 Performance assessment as a function of coupling and carrier frequency offset

5.3.1 The effect of coupling between antenna elements on the performance of the proposed receiver

In practice, the inter-element distance d has to be carefully chosen, in order to guarantee low coupling between the four antenna elements, which is a critical constraint for the wave expressions ($A_i(t), i = 1,2,3,4$) to hold true. Thus, a set of simulations are carried out using the proposed receiver architecture, in order to illustrate the bit error rate degradation for QPSK, as a function of different values of coupling between adjacent antennas.

Simulation results in Figure 5.7, show that for a coupling less than -30 dB, the bit error rate is less than 1 dB away from the ideal additive white Gaussian noise channel ,without coupling, which is illustrated with the constellation graph in Figure 5.8 (QPSK constellation at 10 dB SNR

with BER=10^{-5}). It is also concluded from Figure 5.7, that to get a bit error rate of 10^{-6}, the required signal to noise ratio for -30 dB coupling is 10.6 dB, while almost 15 dB of SNR is required to get the same BER for -10 dB coupling.

In addition, as the coupling factor increases, the bit error rate increases for the same value of SNR. For a coupling factor of -20 dB and -10 dB, the bit error rate is about 10^{-4} and 10^{-3}, respectively (both values at 10 dB SNR). This is also illustrated by simulation results for received QPSK constellations in Figure 5.8(b) (coupling of -20 dB) and Figure 5.8 (c) (coupling of -10 dB). Thus, the antenna elements must be carefully designed to get the lowest values of coupling (less than -30 dB), in order to reduce the bit error rate, and enhance the overall performance of the proposed receiver.

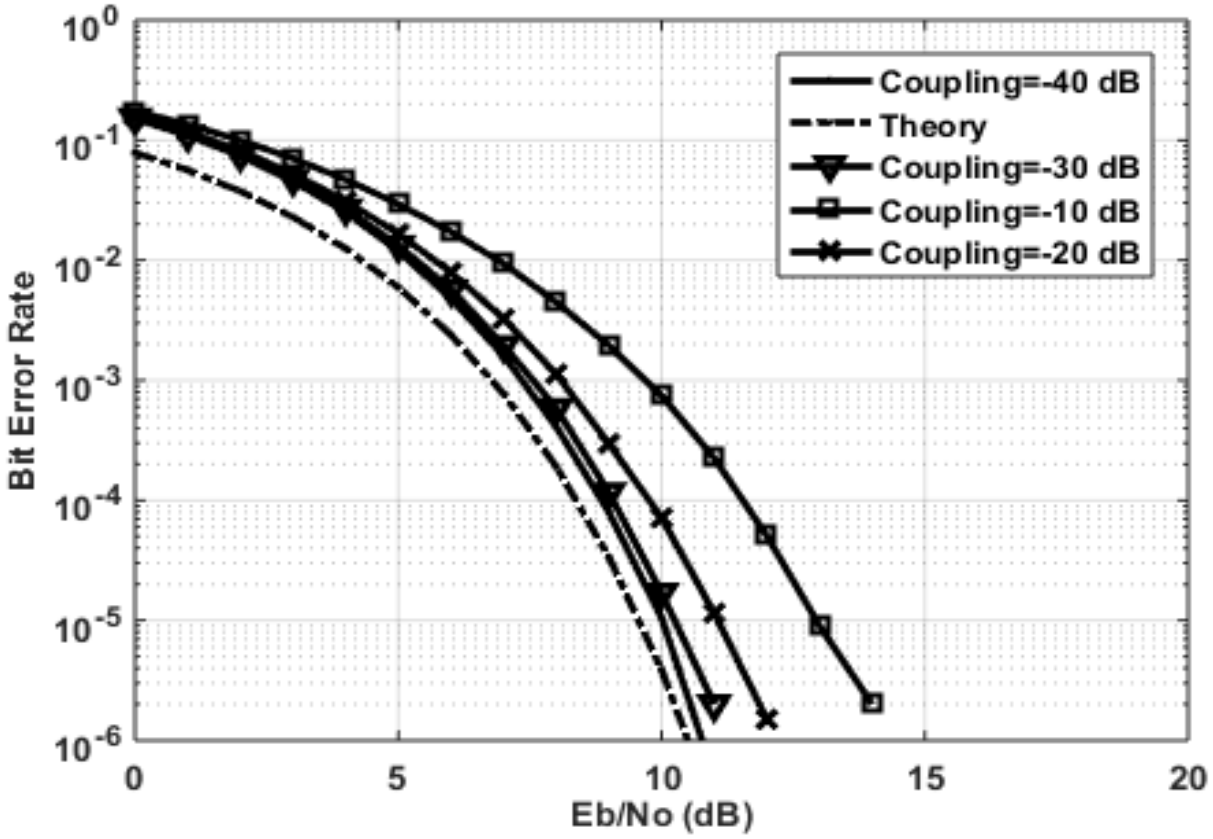

Figure 5.7 Bit error rate for QPSK as a function of different coupling values.

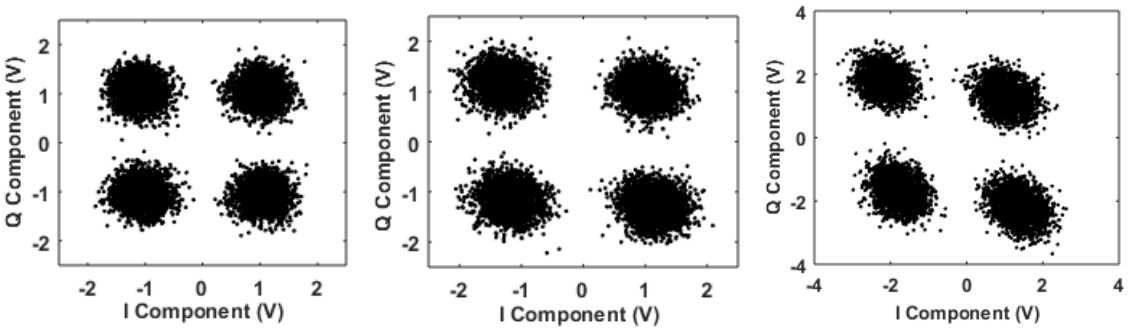

(a) (b) (c)

Figure 5.8 Simulated QPSK at 10 dB SNR and coupling of (a) -30 dB (b) -20 dB (c) -10 dB

5.3.2 Effect of carrier frequency offset

The phase change for β which is driven by a change of the operating frequency (Δf), for a fixed inter-element distance *d*, in connection with center point of the system bandwidth can be easily expressed as:

$$|\Delta\beta| = \frac{2\pi d\cos(\phi_{90})}{c}|\Delta f| = \frac{2\pi d(\lambda_0/4d)|\Delta f|}{c} \tag{5.22}$$

which can be reduced to:

$$|\Delta\beta| = \frac{\pi\lambda_0|\Delta f|}{2c} \tag{5.23}$$

where *c* is the speed of light in free space. It is clear from (23) that the phase offset for β is not correlated to the inter-element distance *d*, for the same change around the center operating frequency.

Moreover, it is worth mentioning that in wireless communications, it is a hard task to synchronize the frequencies at both the transmitter and receiver, because of the frequency mismatch in the transmitter and receiver oscillators; and because of the Doppler effect. As a matter of fact,

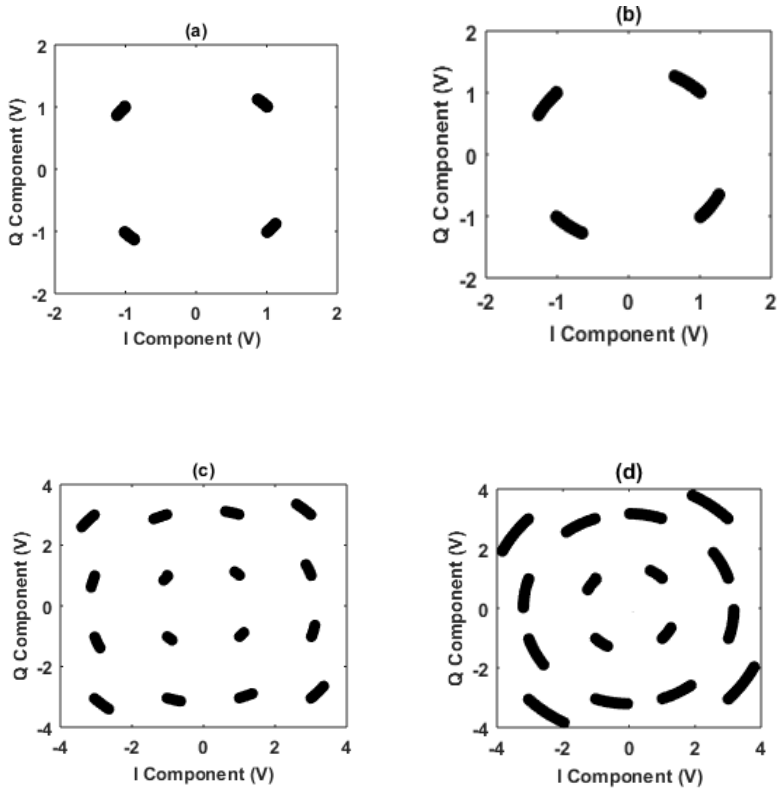

Figure 5.9 Simulated QPSK at freq. offset of 50 Hz, (b) Simulated QPSK at freq.offset of 100 Hz, (c) Simulated QAM-16 at freq. offset of 50 Hz, (d) Simulated QAM-16 at freq. offset of 100 Hz

multiple research studies have been conducted, which propose different techniques and solutions, to overcome the carrier frequency offset between the transmitter and receiver [101].

Simulations are carried out to illustrate the effect of frequency offset. Indeed, Figure 5.9(a) and 9(b) show the simulation results for 1000 received symbols at 1MS/s for QPSK at frequency offset of 50 Hz (with EVM=2.4%) and 100 Hz (EVM=4.6%), respectively. Figure 5.9(c) and 9(d) illustrate results for QAM-16 at 50 Hz (EVM=5.31%) and 100 Hz (11.56%), respectively.

Hence, like in all communication systems, in order to practically implement the proposed receiver in real environment, a module for carrier recovery is of extreme importance, to overcome the carrier frequency offset between oscillators at the transmitter and receiver.

5.4 System simulations

5.4.1 Simulation of the proposed receiver demodulation capability

System simulations are carried out using Advanced Design System (ADS) of Keysight Technologies with a system module as depicted in Figure 5.10. The transmitter (*Tx*) is composed of a modulator fed by a pseudo random bit train at a rate of 1 MS/s (corresponding to a bit rate of 2 Mb/s for QPSK and 4 Mb/s for QAM-16). The carrier frequency is set to be 5 GHz during the simulations and the transmitter power is fixed at 5 dBm. A power amplifier with 6 dB gain is used within the transmitter. A line-of-sight (LOS) link based on the well-known Friis model is used to represent the propagation path between the transmitter and the four receiving antennas ($Rxi, i = 1,2,3,4.$), each with a gain of 6 dBi and the propagation path length is fixed to 1m (beyond the far-field distance which is less than 10cm). In addition, the angle of arrival that makes ϕ equal to 90° was also included in the system simulation model while taking the inter-element distance to be equal to 4.5 cm (which is equal to 0.75 λ_0 at 5 GHz). At the receiver side, four LNAs with 6dB gain each are used at the input of four antennas. The LO frequency is maintained equal to the transmitter operating frequency. The Wilkinson power dividers being used at the receiver are chosen to operate around the center frequency of 5 GHz. In addition, the power detectors used in the simulations are represented by their behavioral function given by (5.12). Then, two ideal differential operational amplifiers are used to generate the I/Q signals according to (5.17). Finally, in order to obtain the demodulation constellation without the transition between consecutive states, two "sample-and-hold" circuits (SHCs) are used in combination with a clock operating at double the symbol rate.

An envelope simulation is performed during a period of 100 μs with a step of 0.2 μs and the clock frequency was set to 2 MHz during the simulations as shown by Figure 5.11 and 5.12 for the recovered symbols of BPSK and QPSK, respectively. The average EVM for QPSK and QAM-16 is found to be 3.3% and 6.85%, respectively.

The proposed system behaves as an excellent demodulator. In fact, for both QPSK and QAM-16 modulations, the simulations results show the ability of the proposed receiver to act as a good amplitude and phase discriminator.

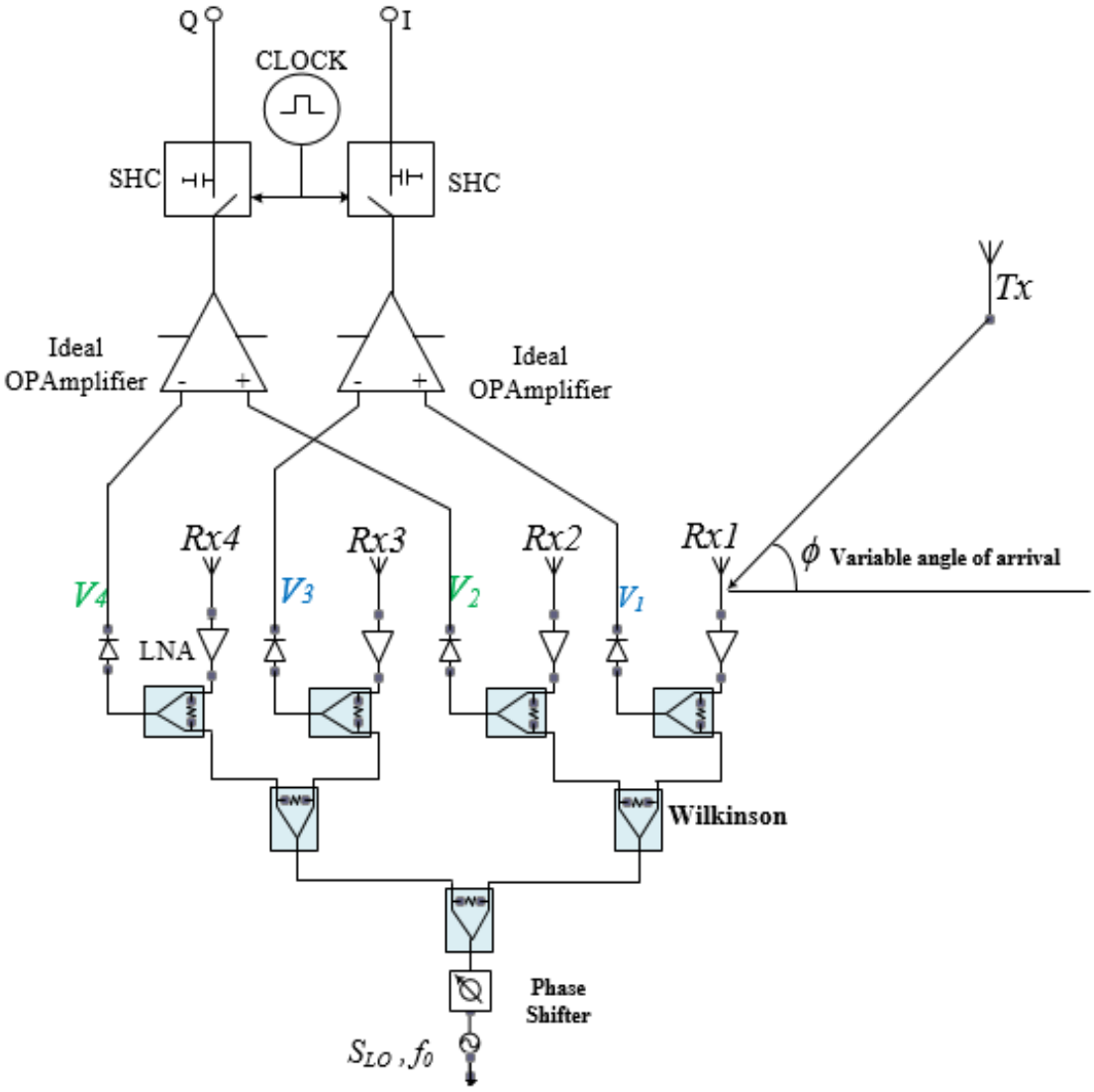

Figure 5.10 ADS simulation bloc diagram for the proposed multi-input interferometric receiver at 5 GHz

Hence, we can conclude that the proposed receiver clearly inherits all the advantages of the conventional six-port direct conversion receivers. Indeed, the whole concept is simple and can be easily implemented through low cost techniques. Moreover, the modulated RF signal is directly converted into its equivalent digital counterpart without the need of passing through a six-port interferometer junction.

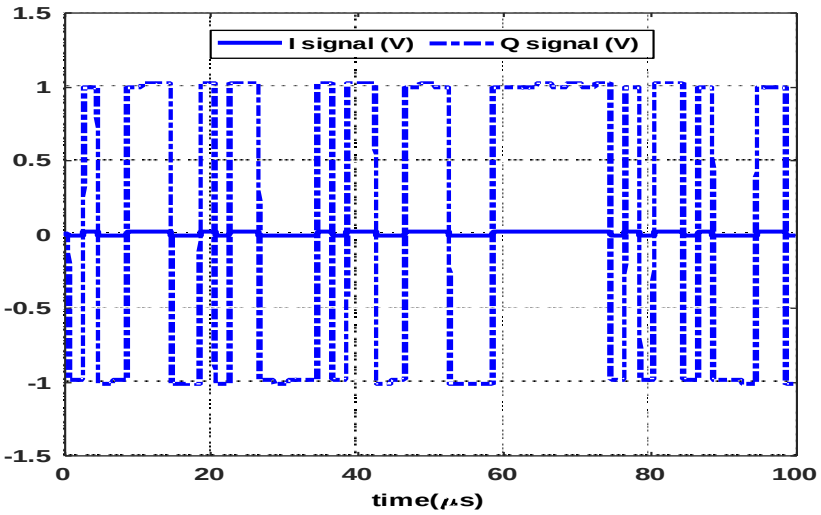

Figure 5.11 Simulation results for the received BPSK symbols over a period of 100 μs

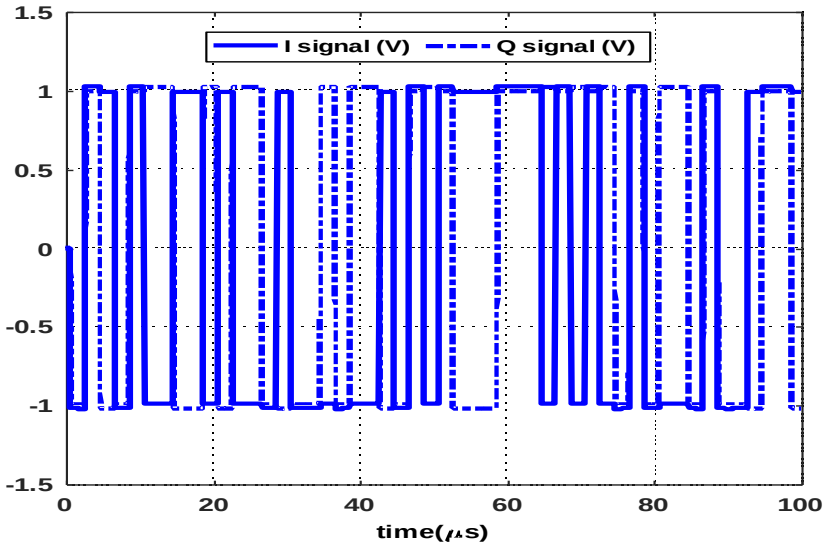

Figure 5.12 Simulation results for the received BPSK symbols over a period of 100 μs

The maximum data rate that could be handled by the proposed receiver is strictly linked to the rise time of power detectors to be used. Thus, simulations at a data rate of 1 MS/s , as shown in Figure 5.13(a) and 5.13(b) are only carried out to provide comparison results with measurements, and the same architecture is used to perform simulations at higher data rates (100 MHz and 200 MHz around 5 GHz at an SNR of 30 dB). Figure 5.14(a) illustrates the received QAM-16 constellations at 100 MS/s (which correspond to 400 Mb/s) with an EVM of 8.82 %. When the

data rate is doubled (800 Mb/s using a bandwidth of 200 MHz), the EVM for QAM-16 increases to 10.4% as depicted in Figure 5.14(b). The increase of EVM is inherently due to the phase offset as expressed in (23) as the phase offset β is equal to 1.8^0 and 3.6^0 for frequency difference of 100 MHz and 200 MHz, respectively. In fact, proper calibration and linearization techniques can be applied to the proposed receiver as it has been done with conventional six-port receivers [96].

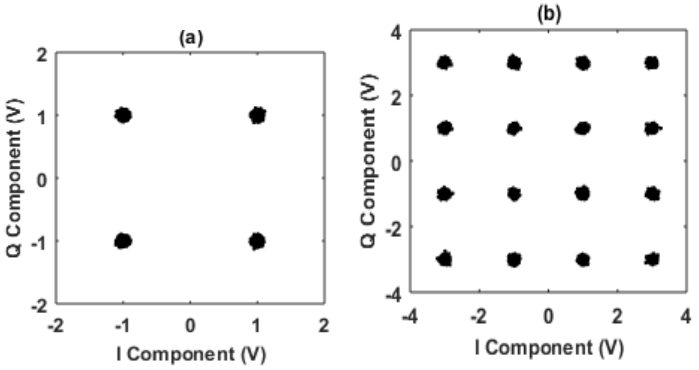

Figure 5.13 (a) received QPSK at 1 MS/s, (b) received QAM-16 at 1 MS/s

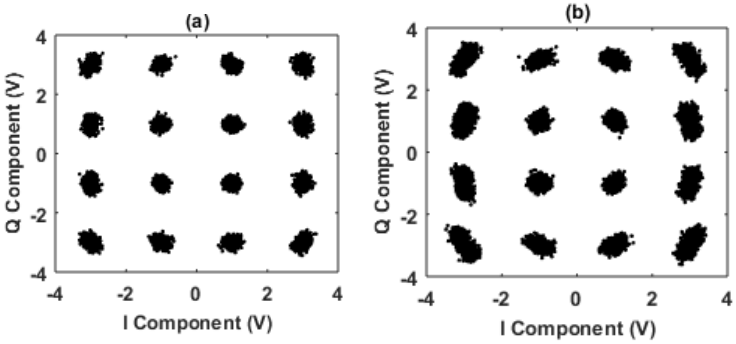

Figure 5.14 (a) received QAM-16 for a bandwidth of 100 MHz, (b) received QAM-16 for a bandwidth of 200 MHz

5.4.2 Simulation of bit error rate for QPSK modulation as a function of angle of arrival

A set of simulations are performed using ADS to compute the BER results for the QPSK modulation under different angle of arrival scenarios. In fact, when the angle of arrival ϕ is different from $\phi_{90,}$ the phase shift β is no longer equal to 90°. Hence, the received constellation is

going to be distorted and the BER would increase. During the simulations, the angle of arrival ϕ is varied for up to 11° around ϕ_{90} and a noise source (additive white Gaussian noise channel configuration) is included in order to compute the average BER for various values of signal to noise ratio. For all scenarios of interest, 1 million QPSK symbols were sent from the transmitter at the rate of 1 MS/s. The *I/Q* signals are determined using the same configuration depicted in Figure 5.10. The theoretical BER for QPSK in the presence of white noise is given by the following function:

$$P_b = \frac{1}{2} erfc\left(\sqrt{\frac{E_b}{N_0}}\right) \tag{5.24}$$

where E_b is the bit energy,$N_0/2$ is the variance of the additive white Gaussian noise, and *erfc* is the complementary error function given by:

$$erfc(z) = \frac{2}{\sqrt{\pi}} \int_z^{\infty} e^{-x^2} dx \tag{5.25}$$

And as the difference between the angle of arrival the optimal value ϕ_{90} exceeds 11^o, the phase difference between the RF signals at the input of the four antennas goes beyond 90° and the demodulation fails due to poor BER. Hence, it can be concluded that the proposed architecture is able to demodulate RF signals as long as the difference between the angle of arrival of the RF signal and does not exceed 11° for the chosen inter-element distance.

Table 5.1 gives the simulations results for the required signal to noise (E_b /N_0) to get a bit error rate on the order of 10^{-6} for various angles of arrival.

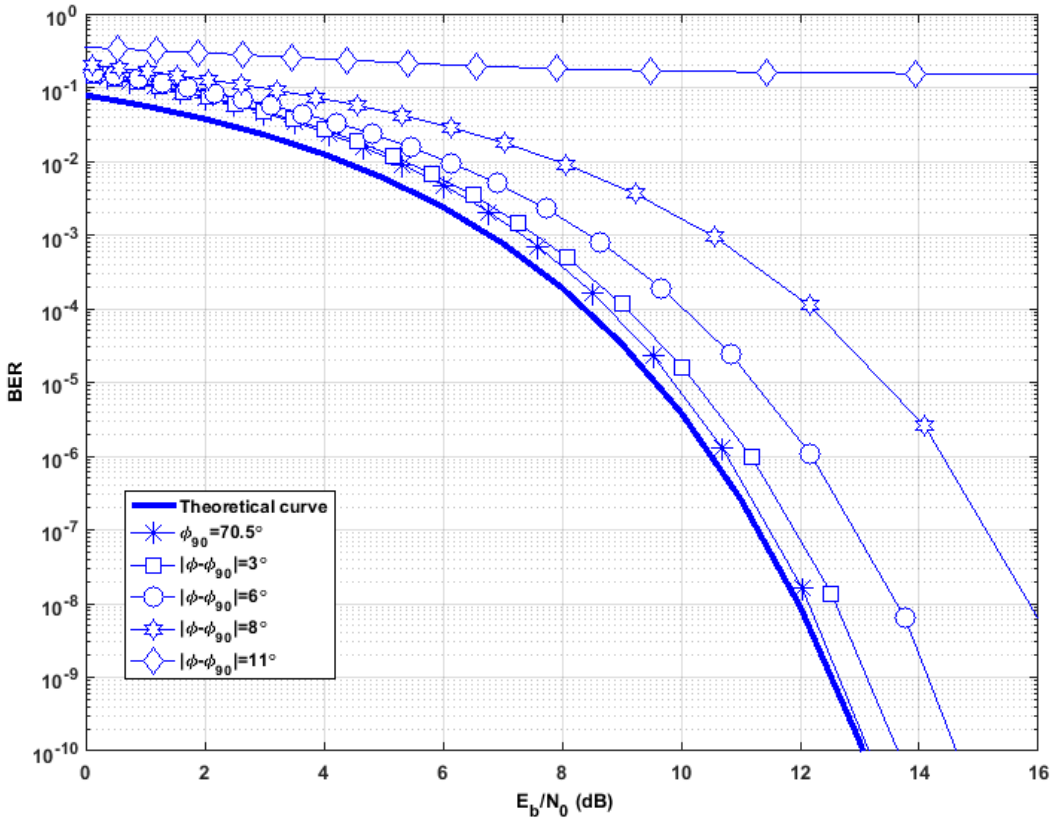

Figure 5.15 Bit error rate for QPSK for different values for angle of arrival

Table 5.1 Simulation results for the required SNR to get BER of 10^{-6}

	Required SNR (dB)
Theoretical value	10.6
$\phi = \phi_{90}$	10.7
$\phi = \phi_{90} \pm 3^o$	11.3
$\phi = \phi_{90} \pm 6^o$	12.15
$\phi = \phi_{90} \pm 8^o$	14.4
$\phi = \phi_{90} \pm 11^o$	N/A

5.5 Conclusion

The mathematical modeling and principle of operation of a novel multi-input interferometer receiver architecture have been presented in details within this chapter. In fact, the demodulation process for the proposed receiver is first explained using the combination of waves at the input of the receiving antennas with a coherent reference LO signal, before applying the resulting combinations to the input of four power detectors operating under their square law region, and using the output dc voltages to extract the transmitted baseband signal. Then, the effect of coupling and carrier frequency offset are studied and quantified through BER results as a function of SNR. In addition, the effect of the angle of arrival shift from the optimal value is also studied in terms of BER as a function of SNR, for different AoA values. Simulations using ADS software are also included to confirm the theoretical model framework.

CHAPTER 6 SPATIALLY DISTRTIBUTED MULTI-INPUT INTERFEROMETER RECEIVER ARCHITECTURE: PROTOTYPE AND MEASUREMENT RESULTS

This chapter focuses on the experimental validation of the performances of the proposed architecture and its feasibility to operate as a direct conversion receiver/demodulator. The design of the receiver components is first introduced with measured results. Then, the operation principle of a test-bench, which is operating at 5 GHz is explained in details. Various PSK/M-QAM modulation schemes are shown to be successfully detected and processed at a relatively low data rate of about 1 MS/s in the aim of validating the proposed concept.

6.1 Components design and fabrication

In order to experimentally validate the theoretical and simulation results presented in the previous chapter, a test bench is designed, and fabricated to operate around the center frequency of 5 GHz. the proposed receiver is composed of four patch antennas designed to operate within 500 MHz bandwidth around 5 GHz and with a gain of about 6 dBi, as depicted in Figure 6.1, with the simulated and measured S-parameters for the reflection and coupling coefficients illustrated by Figure 6.2 and 6.3, respectively . The inter-element distance between the four antennas is chosen to be d = 4.5 cm corresponding to 0.75 λ_0. These antennas are fabricated using the RT/duroid 6002 laminates with a thickness of 1.524 mm. the fabricated antennas have less than -10 dB of return loss and the average coupling between consecutive elements is less than -30 dB around the center frequency of 5 GHz.

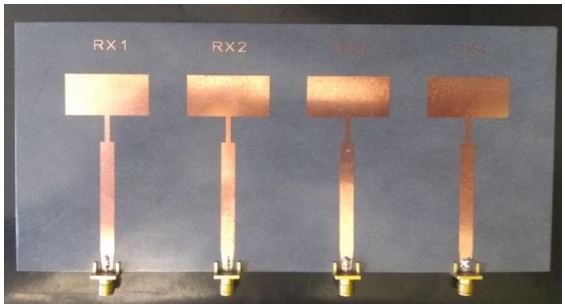

Figure 6.1 Set of four patch receiving antennas at 5 GHz

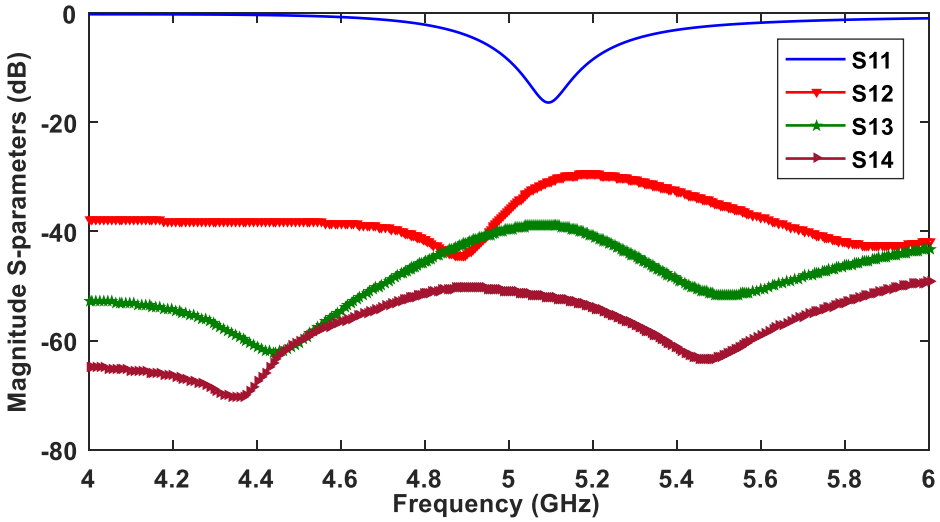

Figure 6.2 S-parameters simulation results for the receiving antenna set

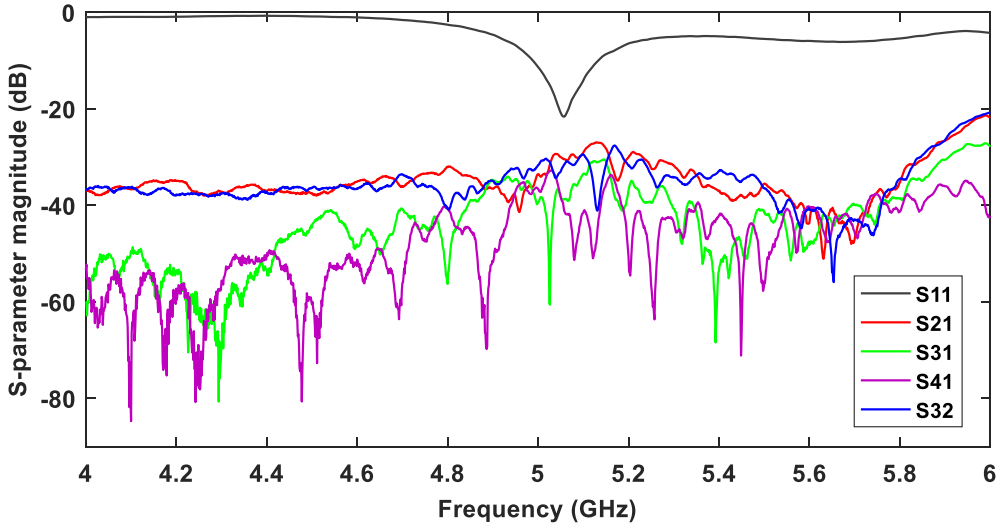

Figure 6.3 S-parameters measurement results for the receiving antenna set

Each of the RF signals at the input of the four antennas is combined with the same version of the local oscillator signal. Indeed, a simple circuit composed of Wilkinson power dividers is fabricated in order to get four identical parts of the LO signal as shown in Figure 6.4. The four signals resulting after combination with the local oscillator signal are passed through four power detectors (Mini-Circuits ZX47-55-S+) operating under their square law region. Finally, a digital phosphor oscilloscope Tektronix DPO7054 is used to display the received constellation.

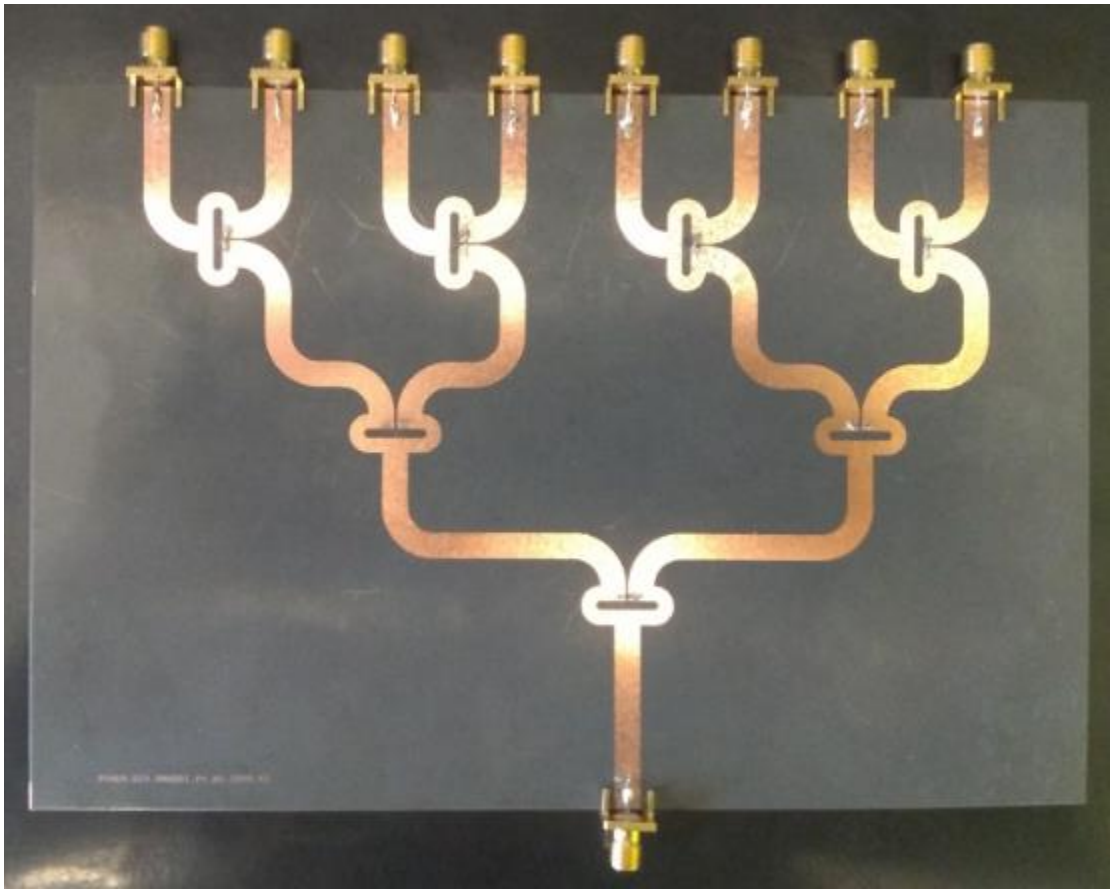

Figure 6.4 Wilkinson based circuit for equal LO power feeding

In fact, the four voltages $(V_i, i = 1,2,3,4)$ are applied to DPO inputs. Then, $V_1 - V_3$ and $V_2 - V_4$ are obtained using the predefined 'substract' operation of the DPO and the constellation is given through the oscilloscope *X*-*Y* display format.

Various modulations are studied using this test bench. First, the Agilent E4438C ESG vector signal generator which operates between 250 KHz and 1 GHz is used to create the modulated and the coherent LO signals at 1 GHz. And an Anritsu MG3692B signal generator is used to generate a pure coherent carrier signal at 4 GHz. Then, both the modulated signal and carrier are mixed with the same 4 GHz carrier using Wilkinson dividers and two Mini-Circuit mixers ZX05-U742MH-S+ , in order to up convert the modulated and coherent carrier around 5 GHz. A band pass filter operating around 5 GHz is designed and fabricated as shown in Figure 6.5, with simulated and measured S-parameters in Figure 6.6 and 6.7(a)-(b), respectively.

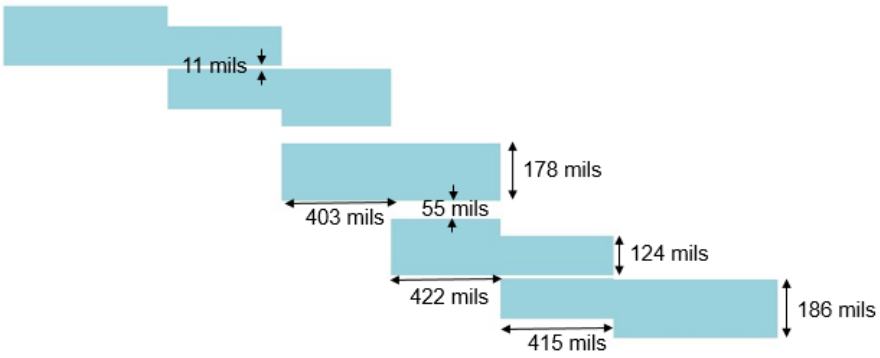

Figure 6.5 Layout of the bandpass filter operating at 5 GHz

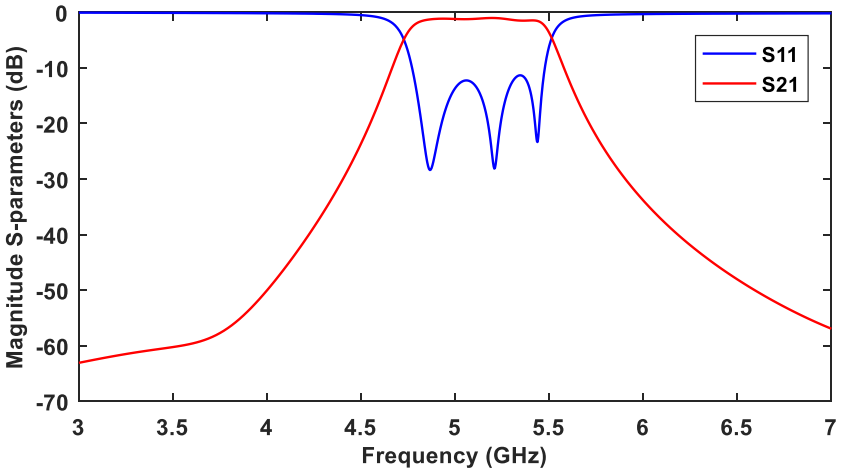

Figure 6.6 Simulated S-parameters for the band-pass filter operating around 5 GHz

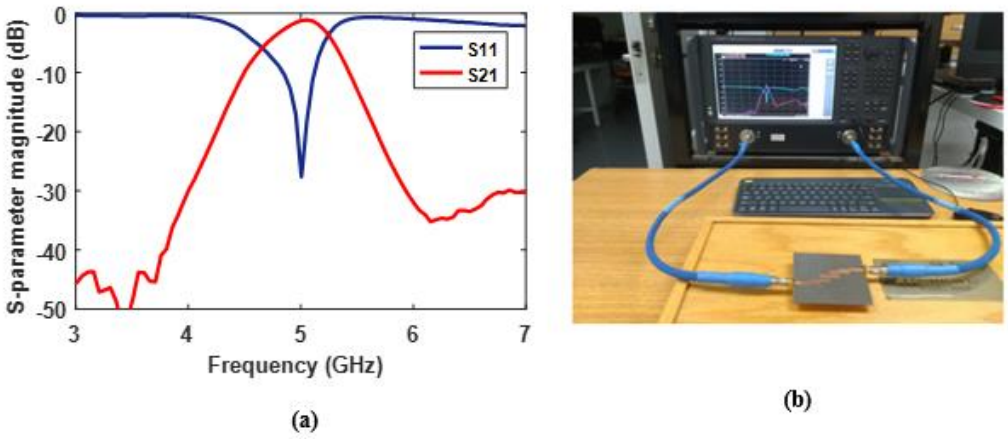

Figure 6.7 (a) Filter S-parameters measurement results, (b) Digital photo of the filter under measurement

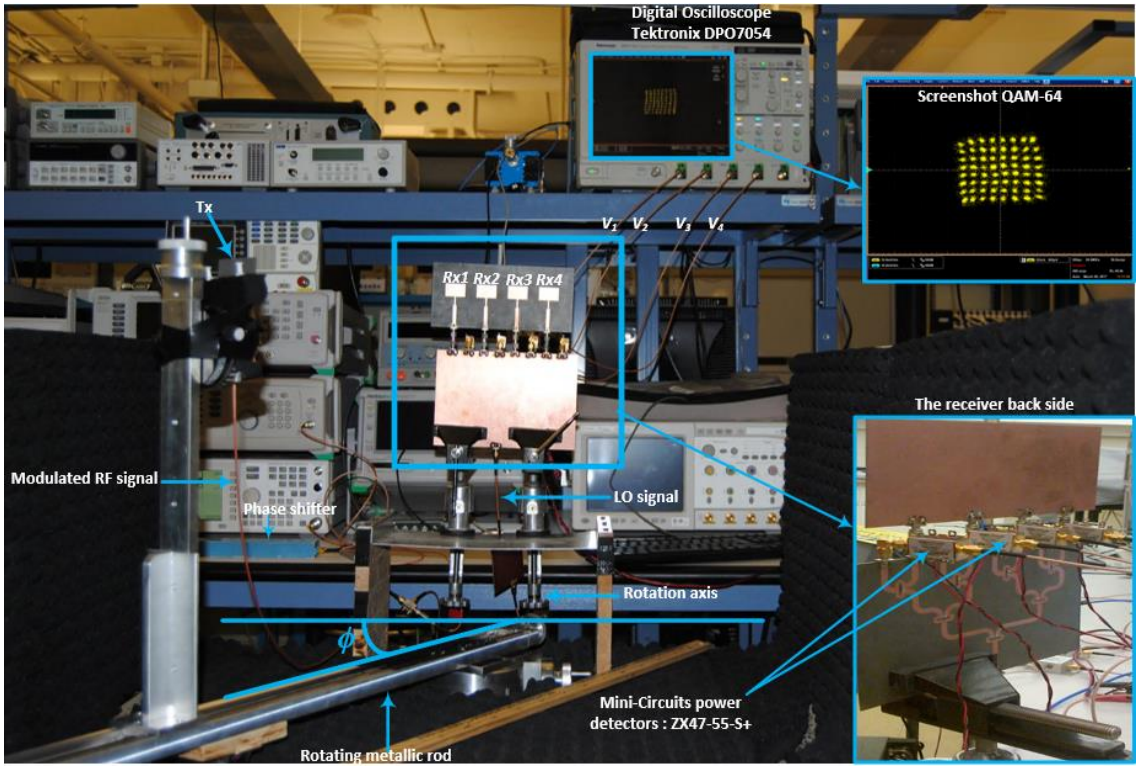

Figure 6.8 Digital photo of the fabricated test bench at 5 GHz with received 64-QAM

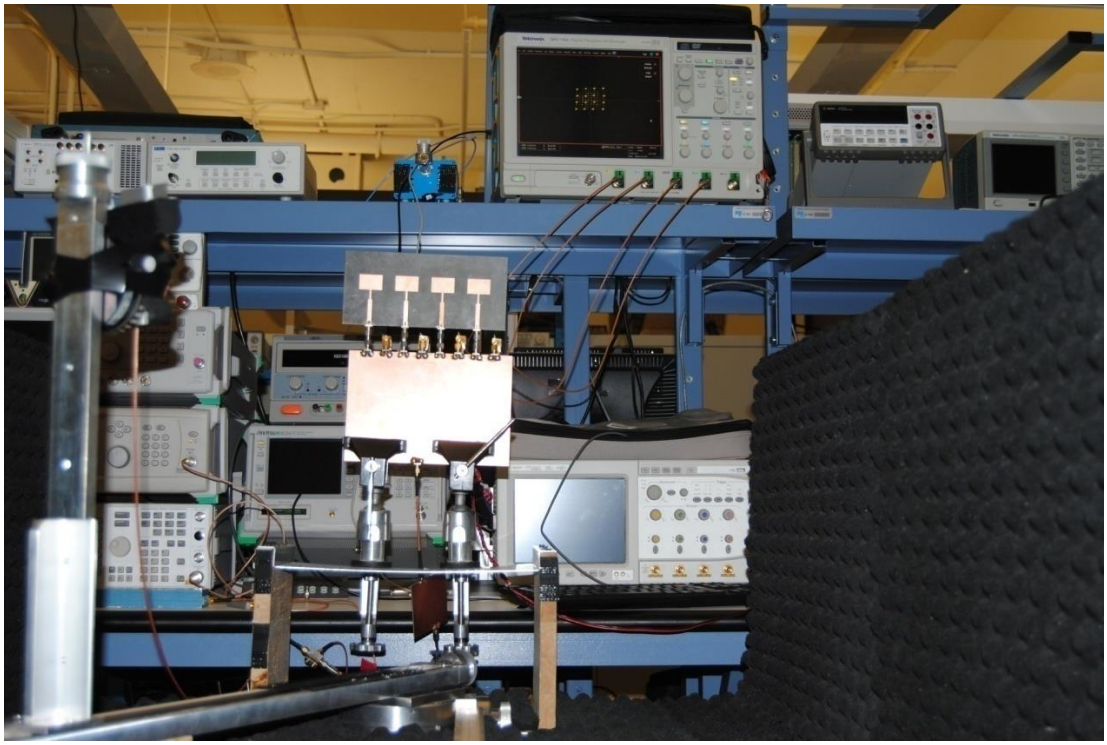

Figure 6.9 Digital photo of the fabricated test bench at 5 GHz with received 16-QAM

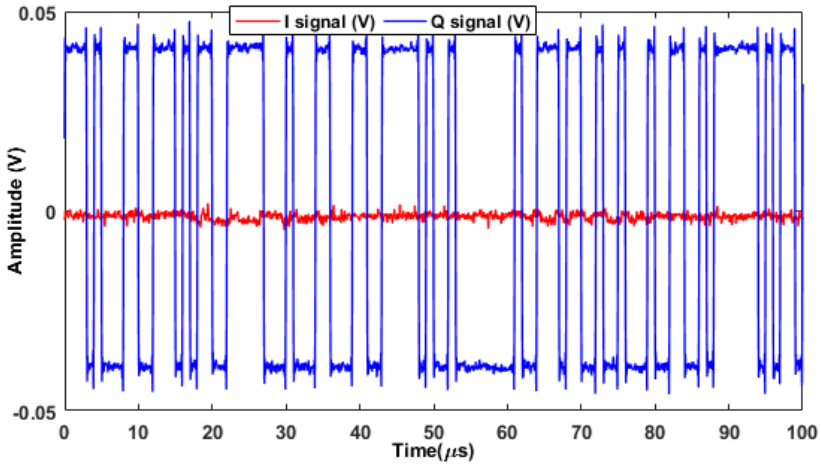

Figure 6.10 received I/Q bit stream for BPSK at data rate of 1Mb/s and over 100 μs

6.2 Test-bench overview and measurement results

During the measurements using the test-bed depicted in Figure 6.8 and 6.9, the Agilent E4438C ESG signal generator is set up to create the standard PSK/QAM modulation schemes at a bit rate of 1MS/s. The power of the modulated signal at the transmitting antenna *Tx* is set at 5 dBm while the LO signal power is fixed at -10 dBm after mixing and before being filtered (around -22 dBm at the input of power detectors).

Moreover, the distance between the transmitting antenna *Tx* and the array of receiving antennas is equal to 1m (in the far field region of the receiving antennas) and the angle ϕ as was fixed at 70^{o} which is equal to ϕ_{90} when d = 4.5 cm. various modulation schemes are successfully received and processed as depicted by the oscilloscope real time screen shots of the complex received constellations in Figure 6.11. For every modulation, the YT display format of the Tektronix DPO7054 oscilloscope is used to capture the train of the in-phase and quadrature components, as depicted in Figure 6.10 for the received I/Q bit streams for BPSK.

For the BPSK constellation in Figure 6.11(a), it can easily be seen that there are two different voltage levels around +40mV and -40 mV and they refer to binary symbols 1 and 0, respectively.

In the case of QPSK and QAM-16, there are 4 and 16 different points, respectively in the complex plane as shown by Figure 6.11(b) and 11(c). As for QAM-32, there are exactly 32 different points as depicted in Figure 6.11(d).

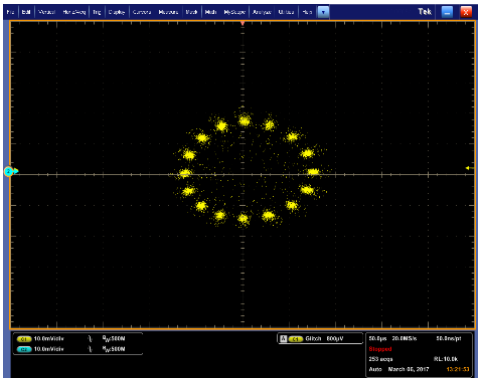

(a)

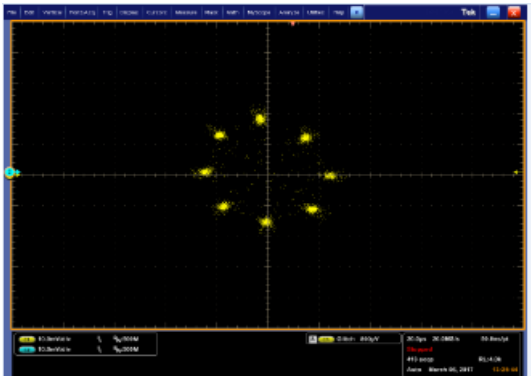

(b)

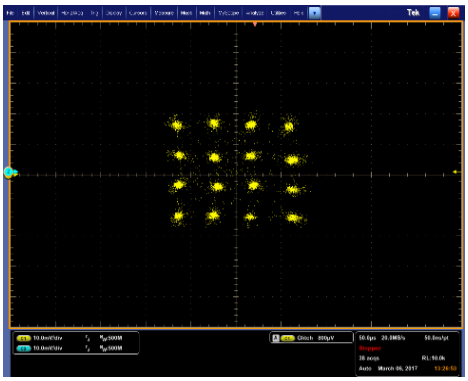

(c)

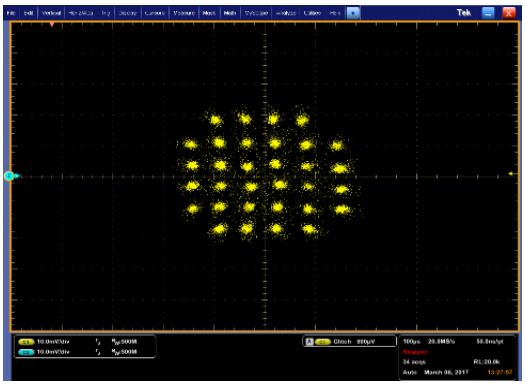

(d)

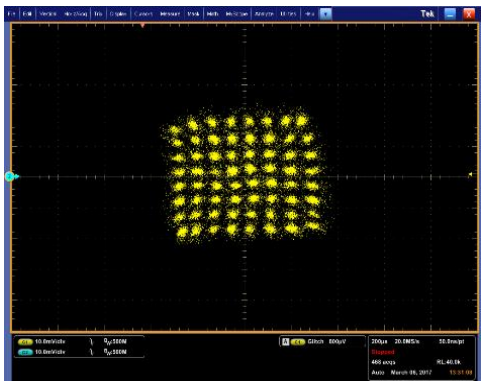

(e)

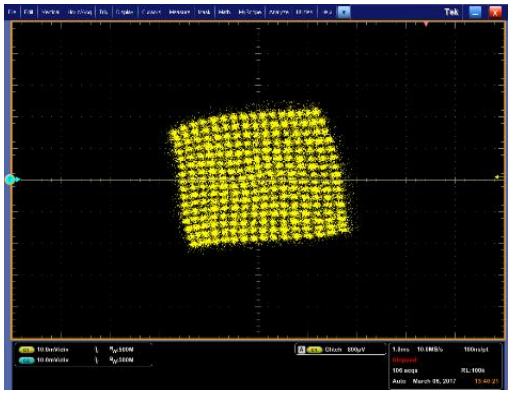

(f)

Figure 6.11 (a) received 16-PSK, (b) received 8-PSK, (c) received 16-QAM, (d) received 32-QAM, (e) received 64-QAM, (f) received QAM-256

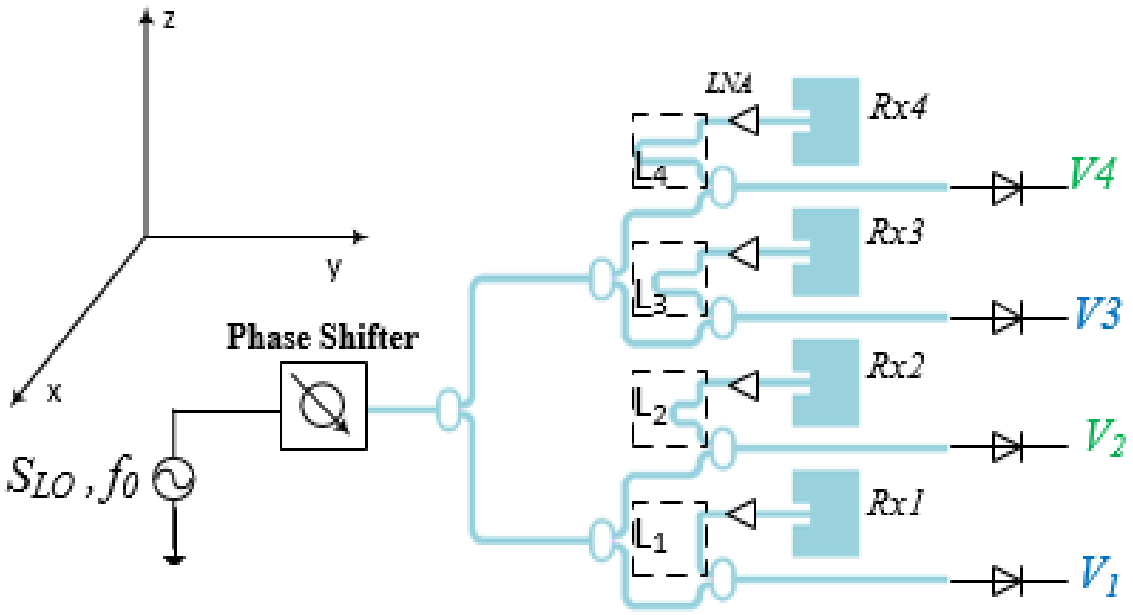

Figure 6.12 Alternative receiver architecture

6.3 Alternative architecture of the proposed receiver

As explained in the previous section, the proposed architecture is suitable for backhaul and fixed point to point communication, as the receiver is unable to perform the demodulation task when the difference between the angle of arrival of the RF signal and ϕ_{90} exceeds a certain threshold (11° in this work). This is because the required 90° phase difference between the RF signals at the input of four antennas, can be only provided for a specific angle of arrival with a certain tolerance to variation around the optimal value.

To overcome the constraint of strict alignment between the transmitter and the receiver and to enable the demodulation for any angle of arrival of the RF signal within the horizontal plane, a new alternative is introduced as depicted in Figure 6.12.

For this new architecture, the four antenna elements would receive the same wave front when the transmitting antenna is at any angle within the horizontal plane. Thus, the same version of the transmitted RF signal A_{rf} *(t)* would be captured at the input of the four antennas. Then four

combinations with the LO signal ($S_{LO}(t)$) are performed with the use of delay lines (L_i, i=1, 2, 3, 4) to provide the following equations:

$$A_{rf}(t) = \alpha(t).a.\exp(j(2\pi ft + \theta(t))) \tag{6.1}$$

$$S_{LO}(t) = a.\exp(j(2\pi ft + \theta_0)) \tag{6.2}$$

$$b1(t) = A_{rf}(t)/\sqrt{2} + S_{LO}(t)/2\sqrt{2} \tag{6.3}$$

$$b2(t) = -jA_{rf}(t)/\sqrt{2} + S_{LO}(t)/2\sqrt{2} \tag{6.4}$$

$$b3(t) = -A_{rf}(t)/\sqrt{2} + S_{LO}(t)/2\sqrt{2} \tag{6.5}$$

$$b4(t) = jA_{rf}(t)/\sqrt{2} + S_{LO}(t)/2\sqrt{2} \tag{6.6}$$

The phases of the delay lines provide the required phase difference (90°, 180° and 270°) between the four versions of the LO signal as highlighted in the previous chapter. The output voltages (V_i, *i=1, 2, 3, 4*) obtained when the normalized waves *bi, i=1, 2, 3, 4* are applied to the power detectors operating under their square law region are the same as those given by (5.13) to (5.16).

Using these four voltages, we can define and obtain the same complex vector as in (5.17). A prototype is fabricated as shown in Figure 6.13 to validate the new alternative using the RT/duroid 4350B laminates with a thickness of 0.762 mm.

In addition, a set of measurements are conducted in order to process various modulation schemes using this second architecture. The results for the BPSK and QPSK are reported in Figure 6.14(a) and 6.14(b), respectively. And the received QAM-16 and QAM-32 are reported in Figure 6.14(c) and 6.14(d), respectively.

The measurements are performed under the same conditions (data rate, transmitted power, antenna gain, distance between the transmitter and the receiver) like the first fabricated prototype previously described. Moreover, all measurements, for both architectures are carried out with an SNR of 30 dB as shown by the received power spectral density for the modulated BPSK signal as illustrated in Figure 6.14(e).

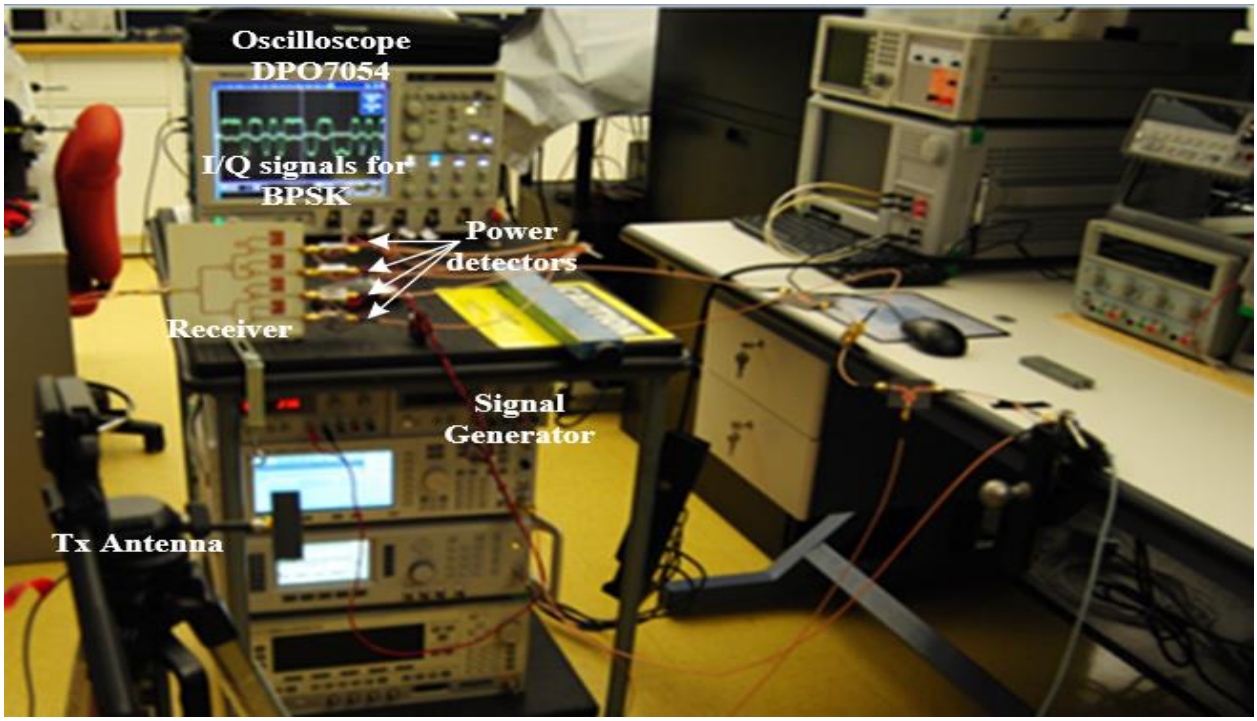

Figure 6.13 Photo of the proposed spatial interferometry based receiver with delay lines

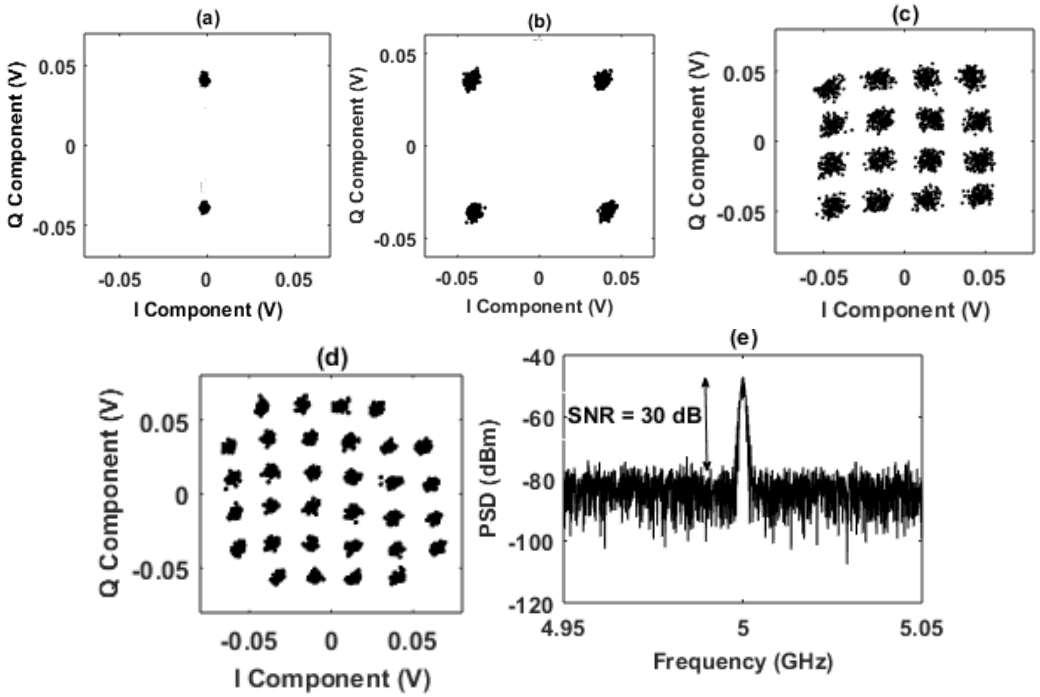

Figure 6.14 (a) received BPSK , (b) received QPSK , (c) received QAM-16, (d) received QAM-32, (e) spectrum of received BPSK at 1 Mb/s

6.4 Error Vector Magnitude measurement results

The error vector magnitude (EVM) which is a measure of the quality of the received signal is computed for the received constellations: BPSK, QPSK QAM-16 and QAM-32 for both receivers (AR1 for test bench in Figure 6.8 and AR2 for test bench in Figure 6.13 and the results are reported in the following table using the following formula [102].

$$EVM\ (\%) = \sqrt{\frac{\frac{1}{N}\sum_{n=1}^{N}\left|R_{EST}[n] - S_{trans}[n]\right|^2}{\frac{1}{N}\sum_{n=1}^{N}\left|S_{trans}[n]\right|^2}} \times 100 \tag{6.7}$$

where $S_{trans}[n]$ and $R_{EST}[n]$ refer to the n-th transmitted and n-th received symbols respectively. During the measurements, the data rate is fixed at 1MS/s for all modulation schemes, and the number of received symbols used to compute the EVM was set to 5000, 10000, 20000 and 25000 for BPSK, QPSK QAM-16 and QAM-32, respectively.

Table 6.1 Summary of EVM measurement results and comparison with the state of the art

Ref	ST	Freq (GHz)	Data rate (Mb/s)	NS	EVM (%)
This work	BPSK simulation	5	1	5000	1.87
	BPSK-AR1	5	1	5000	2.75
	BPSK-AR2	5	1	5000	2.73
	QPSK simulation	5	2	10000	3.3
	QPSK-AR1	5	2	10000	4.6
	QPSK-AR2	5	2	10000	4.5
	QAM-16 simulation	5	4	20000	6.85
	QAM-16 AR1	5	4	20000	7.7
	QAM-16 AR2	5	4	20000	7.5
	QAM-32 simulation	5	5	25000	9.6
	QAM-32 AR1	5	5	25000	10.3
	QAM-32 AR2	5	5	25000	10.1
[85]	QAM-16	7.5	250	N/A	13.5
[43]	QPSK	62	NA	NA	9.5
[86]	QPSK	2.45	0.4	2000	5.9
[87]	QPSK	1.8	31.25	1000	4.7

Note: ST=Signal Type, Freq=operating frequency, NS=number of received symbols

It is shown that as the size of constellation increases, EVM increases as well due to the non-linearity of power detectors. In the case of the first prototype (AR1), the measured EVM is 7.7% and 10.3 % for QAM-16 and QAM-32, respectively. For AR2, the measured EVM is 7.5% and 10.1 % for QAM-16 and QAM-32, respectively. Obtained results are compared with those presented in literature and show good performances in terms of achievable EVM.

6.5 Hardware limitation: Effect of power detector's rise time

The rise time of power detectors (mini-circuits ZX47-55-S+ in this work) being used during the measurements is 400 ns [103]. This limits the power detector bandwidth and consequently the bandwidth of the signal that can be recovered by the proposed receiver without inter symbol interference. The x-dB bandwidth (BW_{x-dB}) of power detectors is linked to its rise time by the following approximation formula [104].

$$BW_{x-dB} = \frac{\ln(9)\sqrt{10^{x/10}-1}}{2\pi t_{rise}} \tag{6.8}$$

The 10- and 3-dB bandwidth of the mini-circuit ZX47-55-S+ are 2.62 MHz and 874 KHz respectively. Hence, if the bandwidth of the demodulated signal is very high compared to the bandwidth of the used low-speed power detectors, the EVM of the received constellation would increase dramatically. Thus, the data rate is limited to a maximum of 1MS/s during the measurements.

Table 6.2 Maximum ratings for the mini-circuit ZX47-55-S+ power detector

Operating Temperature	-40°C to 85°C
Max. voltage	5.7 V
Max. current	120 mA
Rise/Fall time	400/10 ns
Input Power	+18 dBm

Consequently, in order to increase data rates for the proposed multi-input interferometer receiver (and in any other interferometer receiver architecture that requires the use of power detectors), fast power detectors exhibiting very low rise/fall time are needed to be designed in order to allow the processing of higher data rates in the order of 100 Mb/s or more.

6.6 Conclusion

In this chapter, a prototype which is designed and implemented to operate at 5 GHz is introduced in order to experimentally validate the feasibility of the proposed spatially distributed multi-input interferometer architecture, for use as a direct conversion receiver. In fact, measurement results show promising performances in terms of demodulation capability. Various PSK/QAM modulations schemes have been successfully received and processed by the proposed receivers with good EVM figures, which can be further decreased using proper signal processing techniques, such as modeling and calibration using the state of the art linearization algorithms, widely used in literature to enhance the performances of six-port receivers.

CHAPTER 7 PERFORMANCE ASSESSMENT OF THE MULTI-INPUT RECEIVER ARCHITECTURE

In this chapter, the proposed spatially distributed multi-input interferometer receiver is further studied through more system measurement results. In fact, while the previous chapter presented demodulation performance in terms of EVM at transmitter/receiver separation distance of 1m and a received power of about -50 dBm, this chapter focuses on assessing the experimental results of the proposed architecture at different received power values, and at a higher data rate of 20 MS/s using fast power detectors.

7.1 Demodulation performance for different values of the received power

Wireless receivers are designed to operate in real-world context, where the received power is always fluctuating due to the changing features of the surrounding environment (multi-path constructive and destructive interference, path-loss due to transmitter-receiver separation distance, etc.). Hence, it is not always possible to guarantee a fixed RF carrier power at the receiver side because of the channel variation, even when using automatic gain control units, especially at very high data rates, for which AGC cannot follow the speed of change of the received power. Some techniques have been introduced in literature to overcome wireless channels fast fading, such as diversity techniques (spatial diversity, frequency diversity or polarization diversity), in the aim of increasing the average signal to noise ratio (using selection combining SC, equal gain combining EGC or maximum ratio combining MRC), or to create redundancy (when using space time coding STC technique like Alamouti scheme) in order to overcome fading and decrease the bit error rate [1-4].

As a matter of fact, the proposed receiver demodulation performance must be assessed for different values of received RF signal power. Thus, the power of the transmitted modulated signal is varied, and the EVM is computed for each value, while keeping a fixed Tx/Rx distance in order to get different values of the received power. It is worth mentioning that getting multiple values of the received power could be also performed when changing the distance between the

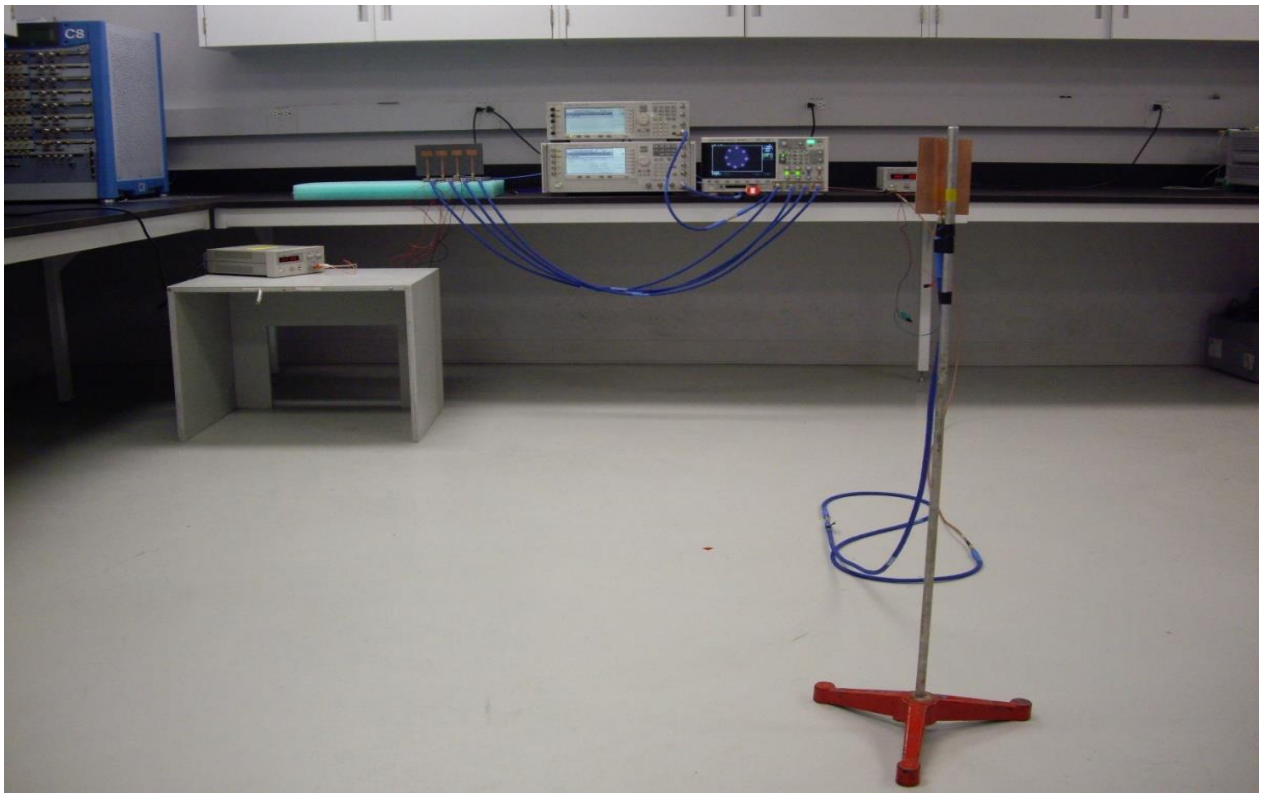

Figure 7.1 Experimental setup for performance assessment (8-PSK modulation)

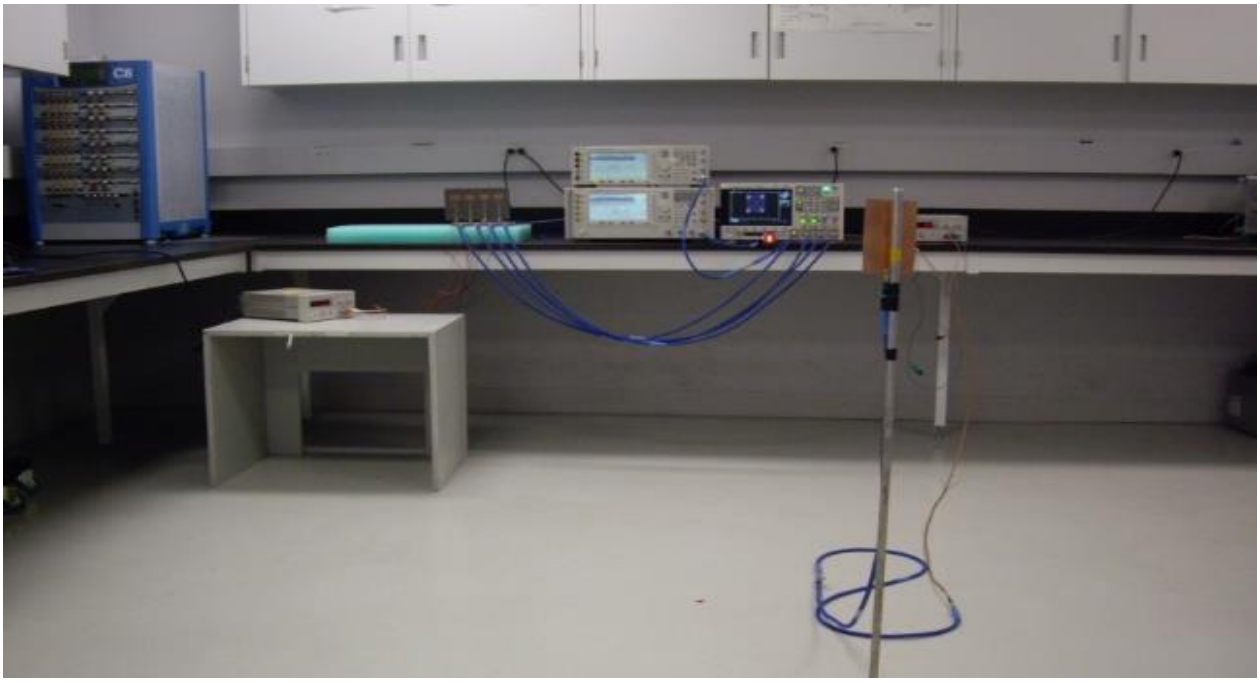

Figure 7.2 Experimental setup for performance assessment (QPSK modulation)

transmitter and receiver, while keeping the same transmitted power. However, getting only 6 dB change in the received power for this method requires doubling the Tx/Rx separation distance, when considering free-space propagation with a path-loss exponent of two. Hence, multiple cables will be required to get to far distances, which will further reduce the signal power because of the cables internal loss, and this would result in wrong estimation of the received power. For all these reasons the first method is used in our experiments as shown in Figure 7.1 and 7.2, because of its simplicity and better accuracy.

The distance between the transmitter and receiver is fixed at d = 3 m as shown in Figure 7.2 and the transmitted power P_t is varied between 5 dBm and -15 dBm. Gains of antennas used in measurements are $G_t = G_r$ = 6 dBi at 5 GHz. In addition, the mixers used for up-converting the modulated signal and the coherent carrier, introduce a conversion loss of about CL = 10 dB. Hence, a power amplifier with a gain G_{amp}=15 dB is included after mixing to enhance the transmitted RF signal power level, as depicted in Figure 7.3.

The free-space path loss can then be calculated as follows [1]:

$$FSPL = 20\log_{10}(\frac{4\pi fd}{c}) - G_t - G_r \tag{7.1}$$

where f = 5 GHz and $c = 3.10^8$m/s. For these values, the free-space path loss is about 44 dB.

Consequently, the power of RF modulated signal P_r at the input of each of receiving antenna elements is given by:

$$P_r = P_t + G_{amp} - CL - FSPL \tag{7.2}$$

Thus, the received power at each of four elements is varying between roughly -34 dBm and -54 dBm during experiments, which has been also verified using a spectrum analyzer, where a

difference of less than 2 dB is noticed, and proper correction is made at the transmitter side to get the expected received power level.

Table 7.1 Summary of the system parameter values

Frequency of operation	5 GHz
Tx/Rx Antenna Gain	6 dBi
Max. transmitted power before mixing	5 dBm
Min. transmitted power before mixing	-15 dBm
Power amplifier gain	15 dB
Mixer conversion loss, CL	10 dB
Tx/Rx separation distance	3 m
Path loss, FSPL	44 dB
Max. received power	-34 dBm
Min. received power	-54 dBm

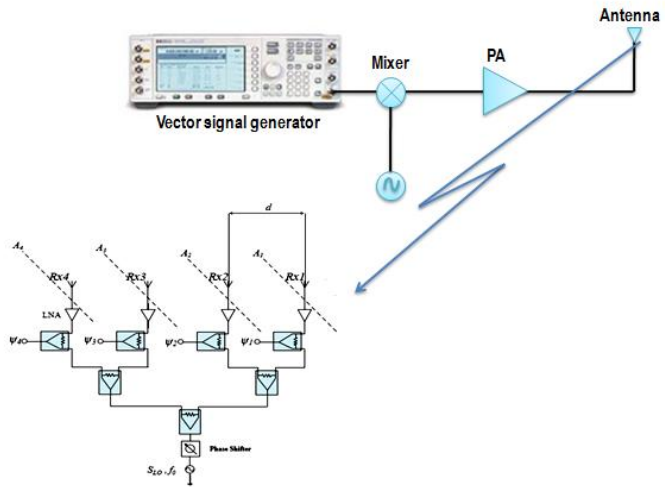

Figure 7.3 Bloc diagram of the experimental test bench

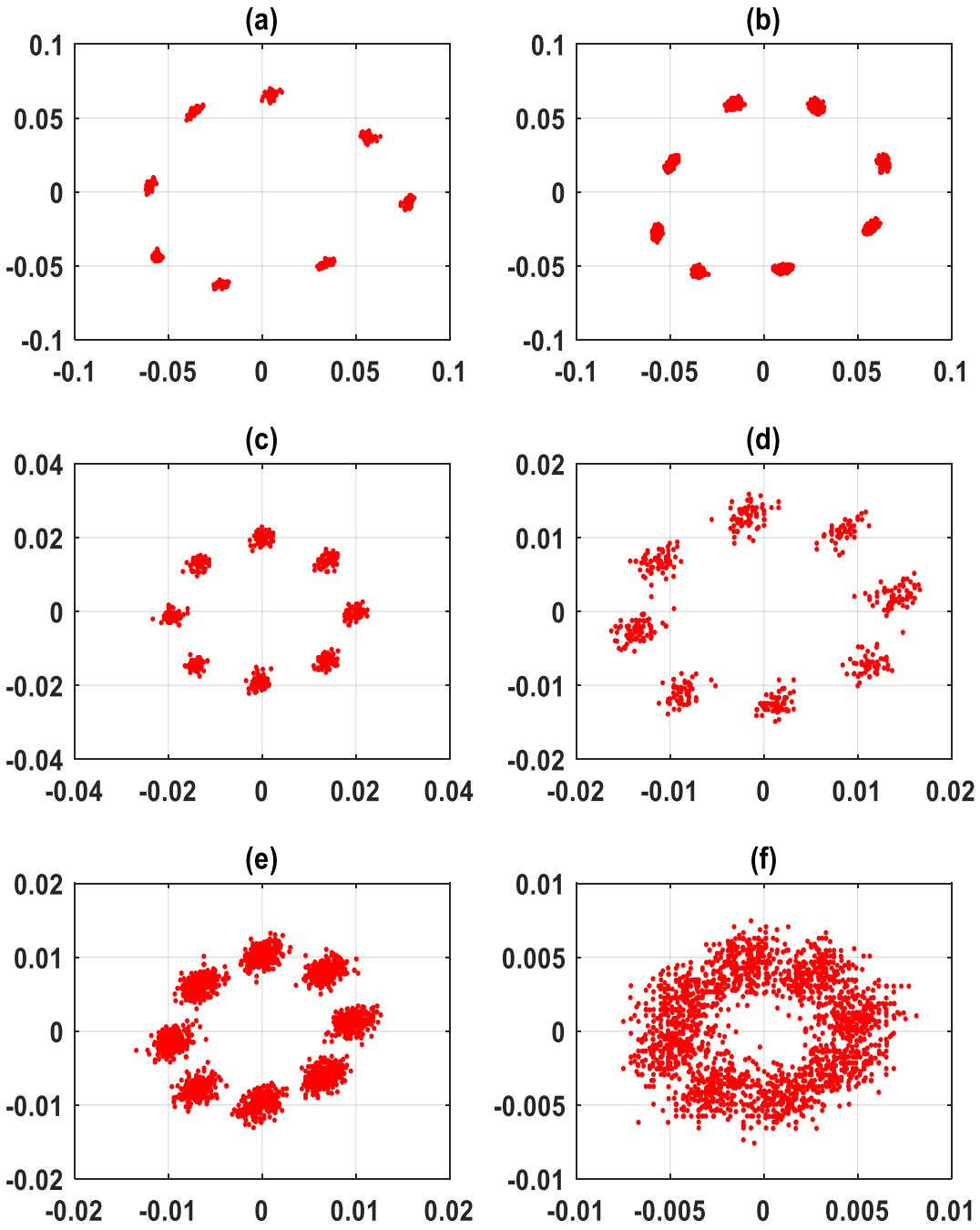

Figure 7.4 Received 8-PSK for : (a) P_r = - 34 dBm, (b) P_r = - 37 dBm,(c) P_r = - 40 dBm,(d) P_r = - 45 dBm,(e) P_r = - 50 dBm, (f) P_r = - 54 dBm

Measurement results at different power levels are reported in Figure 7.4 for 8-PSK modulation. The received power varies between -34 dBm and -54 dBm, while the LO at in the input of power detectors is kept at -25 dBm for all scenarios.

For each power level of the RF modulated signal, the received I/Q bit streams are captured through the Y-T function of the oscilloscope, then the measurement files are processed using MATLAB in order to plot the received constellations and compute the EVM for each value of the received power.

A set of 1000 symbols are used to plot the received constellation, with EVM results reported in the following table.

Table 7.2 EVM results for 8-PSK as a function of the received power

Received power (dBm)	**EVM (%)**
-34	8.2
-37	7.5
-40	4.9
-45	5.7
-50	8.32
-54	21.4

It can easily be noticed that EVM reaches its lowest value when the difference between the LO and RF modulated signal power levels is about 15 dB (for a received power of -40 dBm). If the level of the incoming RF signal is much lower than -40 dBm, the EVM increases to reach 21.4 % for a modulated signal level of -54 dBm, which is due to the non-linearity of the power detector response and the noise limit at the lowest end of the detector dynamic range.

Hence, the difference between the level of the coherent carrier and RF modulated signal must be kept moderate (between 10 and 20 dB), in order to get the lowest possible EVM. Such results can be also found in conventional six-port receivers as well.

7.2 Design of fast power detectors

The measurement results presented in the last section, as well as within the previous chapter are reported for a relatively low data rate of 1 MS/s (which is equivalent to 1 Mb/s for BPSK, 2 Mb/s for QPSK, 3 Mb/s for 8-PSK, 4 Mb/s for 16-QAM and 5Mb/s for 32-QAM).

However, 5G systems are supposed to operate at data rates which are multiple orders of magnitude higher than 1 MS/s. Thus, a solution must be introduced to experimentally validate the feasibility of the proposed multi-input architecture to operate at higher data rates.

The rise time of power detectors (mini-circuits ZX47-55-S+) being previously used during the measurements is 400 ns, which is the principal limitation against operating at higher data rates.

In fact, the rise time of power detectors defines the maximum bandwidth of the RF modulated signal to be processed, with almost no memory effect, as specified by (6.8). In order to increase data rates, power detectors with low rise time have to be designed. As a matter of fact, the 4 mm × 4 mm Analog Devices AD8318 logarithmic power detector with a rise time of about 10 ns, is chosen.

The basic connections of this surface mount chip are illustrated by Figure 7.5, with Table 7.3 highlighting the most important features of Analog Devices AD8318 logarithmic power detector as given by the manufacture data sheet [106].

Table 7.3 Principal features of Analog Devices AD 8318 logarithmic power detector

Bandwidth of operation	1 MHz to 8 GHz
Accuracy	±1.0 dB over 55 dB range (f < 5.8 GHz)
Stability over temperature	±0.5 dB
Rise/fall time	10 ns
Power-down feature	< 1.5 mW at 5V
Single-supply operation	5 V at 68 mA
Fabrication process	SiGe process
Dynamic range	70 dB

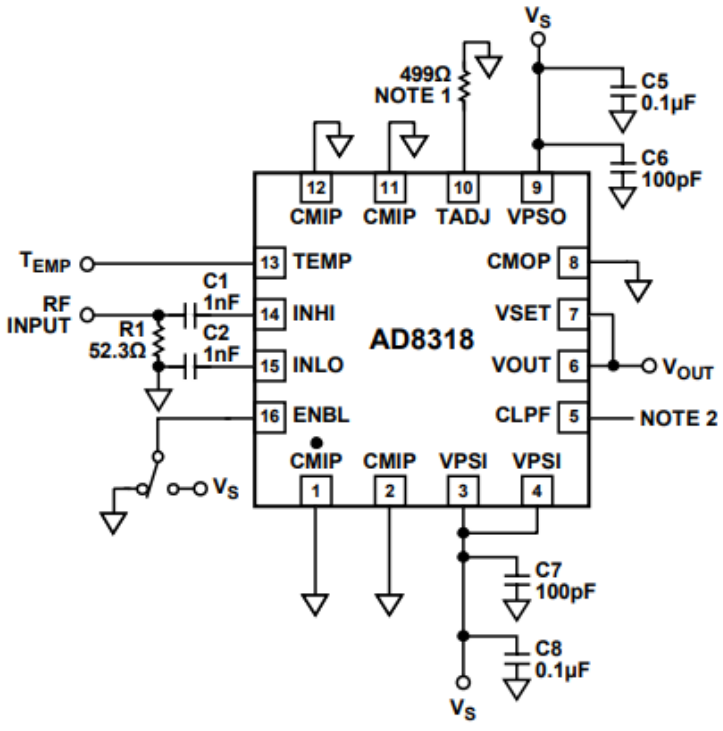

Figure 7.5 AD8318 basic connections

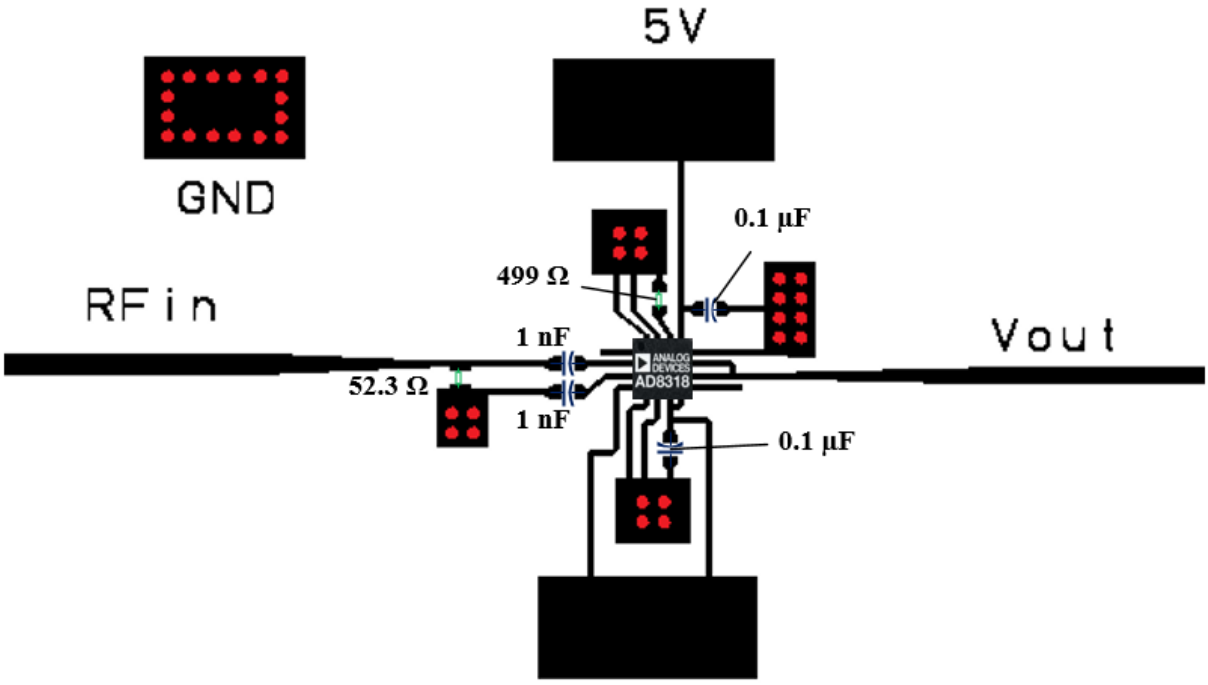

Figure 7.6 ADS layout of AD8318 power detector

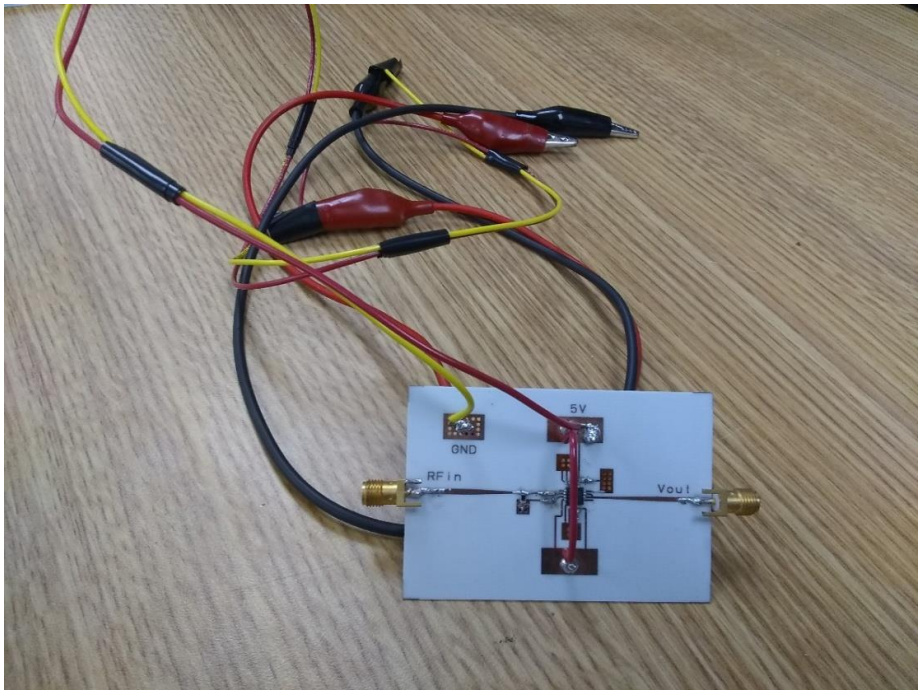

Figure 7.7 AD8318 fabricated prototype using RO4350B laminates with relative permittivity of 3.48 and thickness of 0.5 mm

7.3 Characterization of AD8318 power detector

The 3-dB bandwidth (BW_{3dB}) of power detectors is linked to their rise time through the formula given in (6.8). Thus, power detectors have to be used to detect the envelope of modulated signals with bandwidth less than BW_{3dB}. If the bandwidth of the modulated signal exceeds BW_{3dB}, the output response would exhibit memory effects, which will cause inter-symbol interference and increase the EVM of demodulated signals.

The fabricated AD8318 logarithmic power detector depicted in Figure 7.7 should be characterized before being used in demodulation .The process of characterization is performed using an input modulated signal (AM modulation with 100% modulation index) with carrier level of -30 dBm. A predefined baseband data stream consisting of a series of 4 zeros followed by 4 ones at 20 MS/s is used, in order to facilitate the interpretation of measured results and alleviate any confusion, as illustrated by the test bench in Figure 7.8.

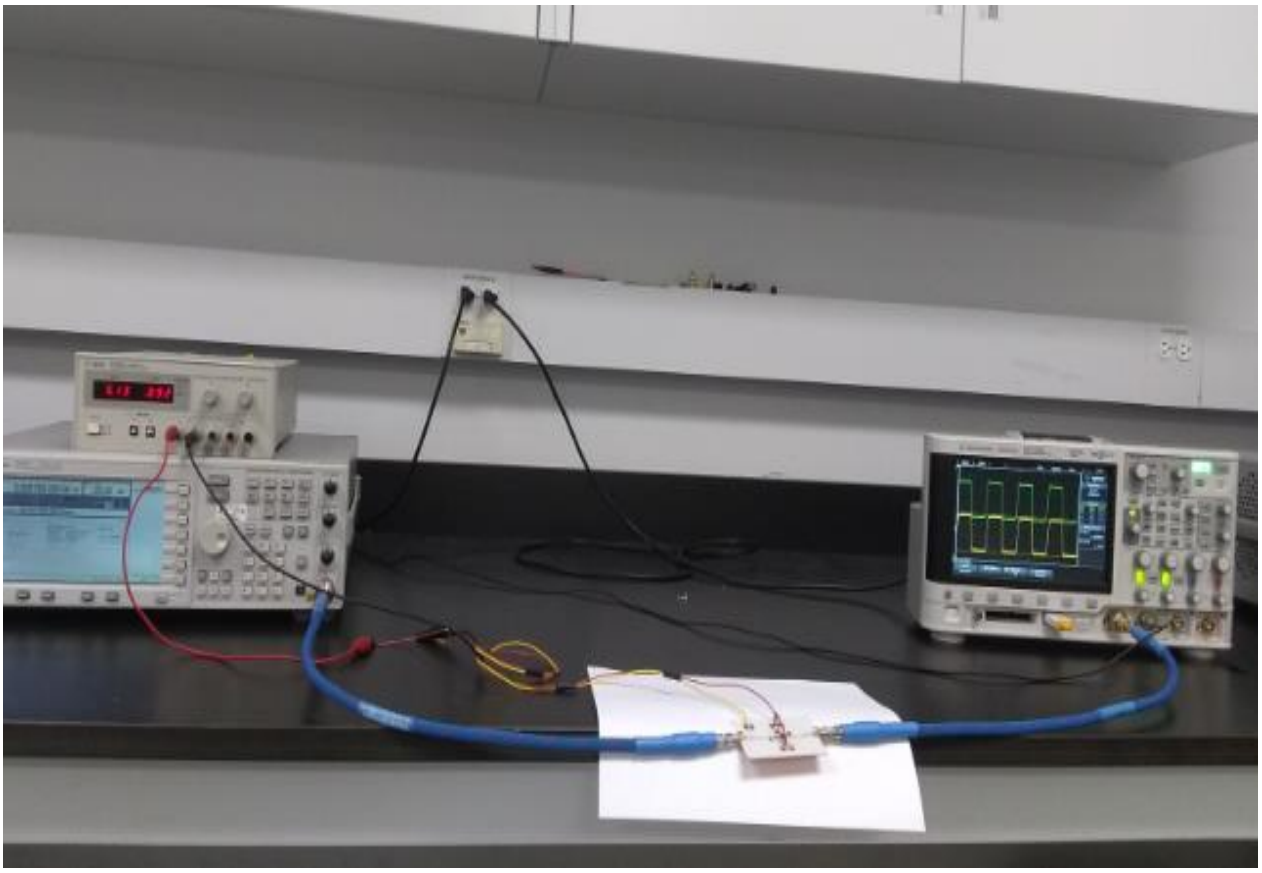

Figure 7.8 Photo of AD8318 power detector characterization test bench

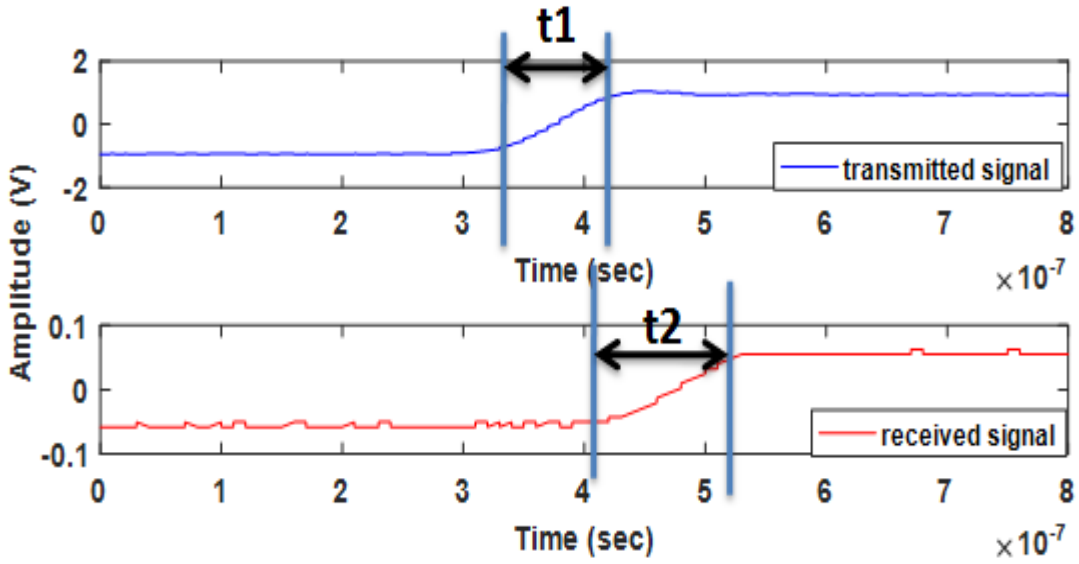

Figure 7.9 Measured input and output signal using AD8318 power detector at 20 MS/s

As depicted in Figure 7.9, the input baseband signal is not a pure square wave. Thus, we must compute the time difference t2-t1, which is called the de-embedded rise time. In the case of the fabricated AD8318 power detector, t2-t1=17 ns. In the datasheet, this power rise time is about 10 to 12 ns, the difference is mainly due to the quality of used coaxial cables during measurements (because of their low-pass filtering effect, which would increase the rise time of signals at their input).

Another characterization step is dynamic range, which is performed through getting the output voltage while varying the power level of a non-modulated carrier at the input of the fabricated power detector at the frequency of 5 GHz. It is worth mentioning that for the demodulation process using the proposed multi-input receiver architecture, it is only the linear region (output voltage that is proportional to input power) to be considered. Indeed, the part of the characteristic curve outside the linear region (also called square-law region) cannot be used, unless linearization of the whole receiver is performed in order to overcome distortion caused by non-linearity.

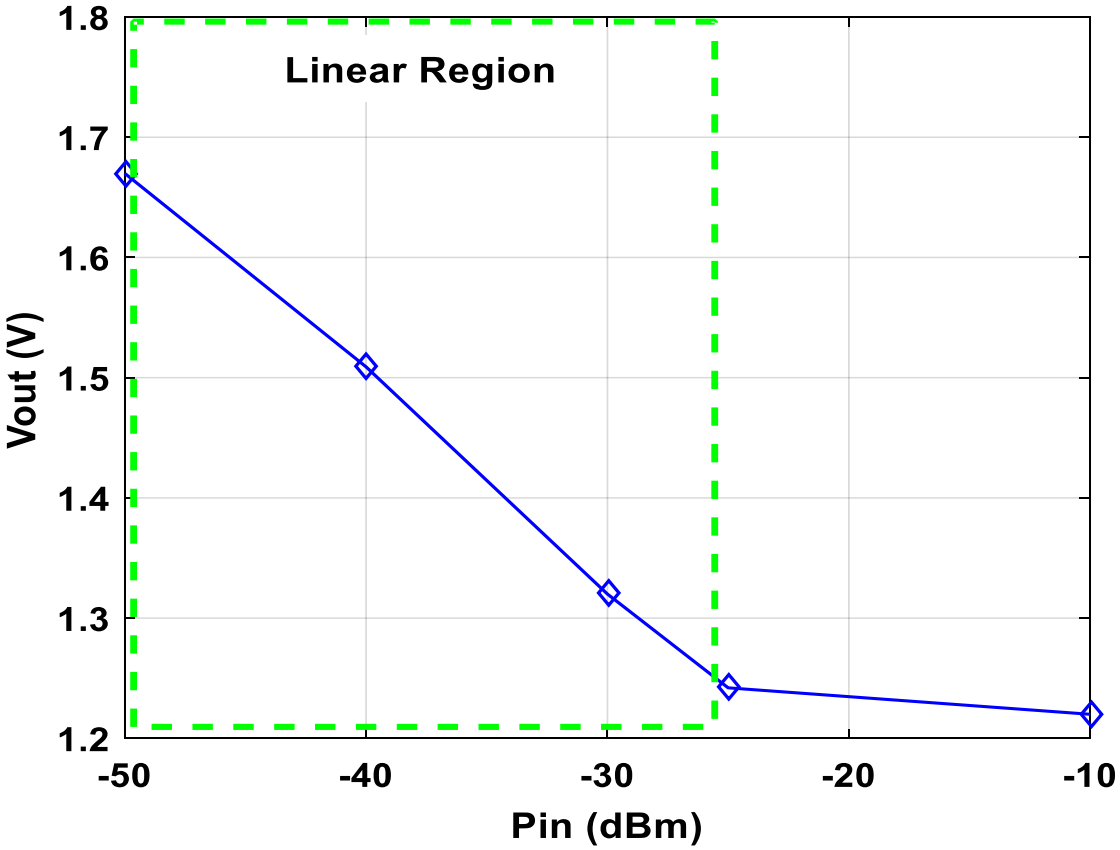

Figure 7.10 Measured output voltage as a function of input power level for the fabricated AD8318 power detector

The characteristic function of the fabricated power detector is given by Figure 7.10. In fact, the linear region extends from -50 dBm to -25 dBm, with a negative slope of -17 mV/dB computed through the following formula:

$$slope = (Vout_{-50dBm} - Vout_{-25dBm}) / 25 \tag{7.3}$$

Moreover, the measured 3dB-bandwdith of the fabricated power detector can be computed using the measured rise time of about 17 ns and is equal to 20.5 MHz following the formula (6.8). Consequently, the fabricated power detector can process data rates of up to 20 MS/s. the general 3dB-bandwdith as a function of rise time is illustrated by Figure 7.11.

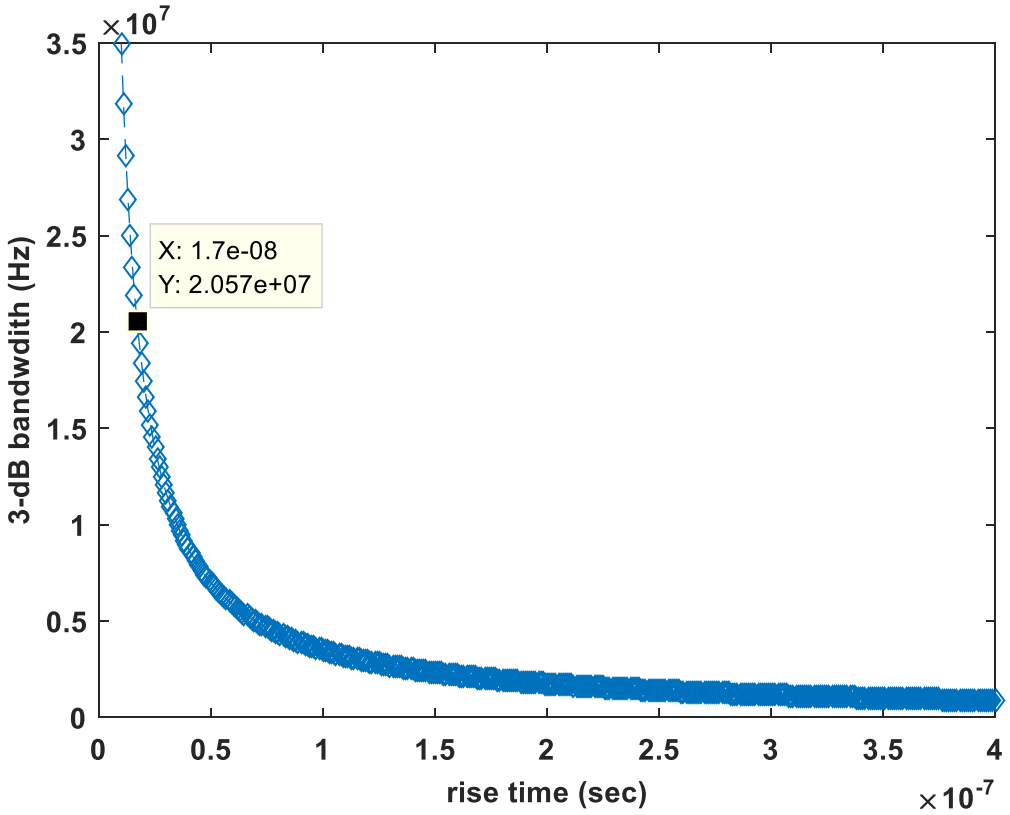

Figure 7.11 3dB-bandwidth of power detector as a function of its rise time

7.4 Demodulation results using AD8318 power detector

7.4.1 Experimental test bench

As depicted in Figure 7.12, an experimental test bench is implemented in order to demodulate signals at 20 MS/s data rate and using the fabricated AD8318 power detector. In fact, a set of four ultra-wideband Vivaldi antennas (as illustrated by Figure 7.13 and 7.14, along with simulated and measured return loss in Figure 7.15) are designed to operate between 3 GHz and 7 GHz with a roughly stable measured gain of 5.7 dBi. The inter-element distance is chosen to be equal to 4.5 cm and two vector signal generators are used during the experiments, where the Agilent E4438C ESG (VSG1) provides the RF modulated signal along with the coherent carrier at 2.5 GHz, while

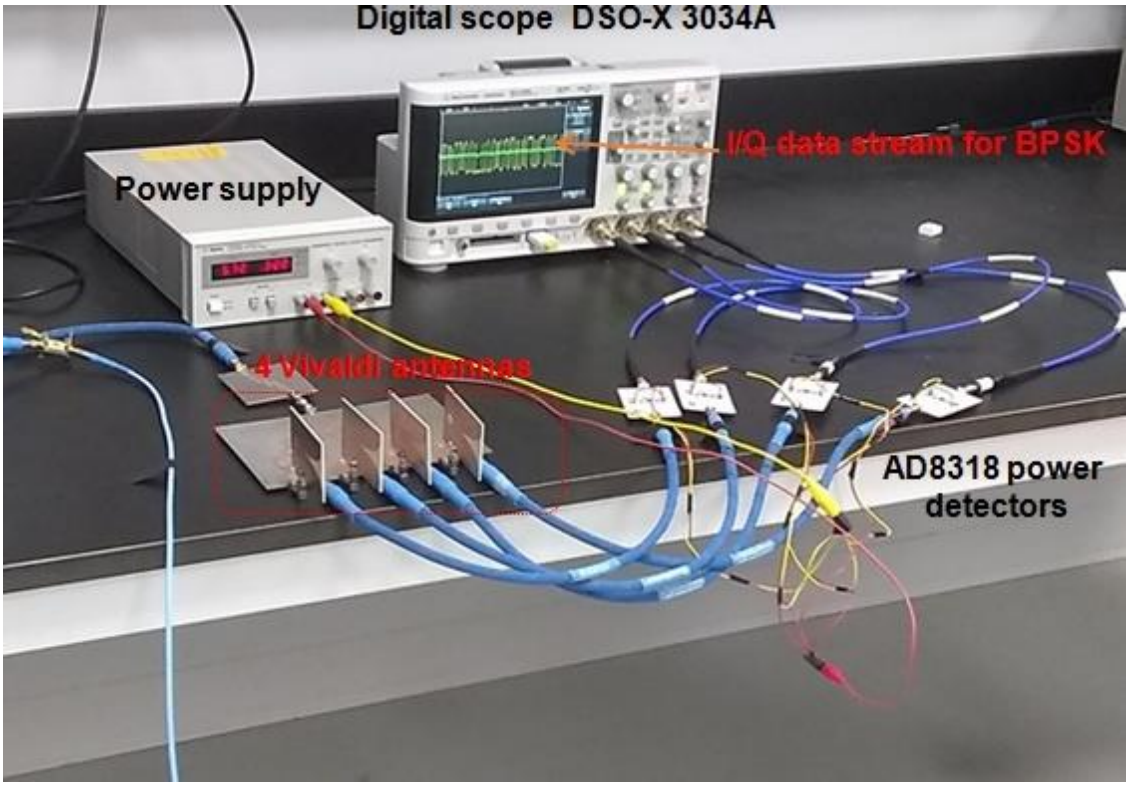

Figure 7.12 Photo of test bench operating at 5 GHz

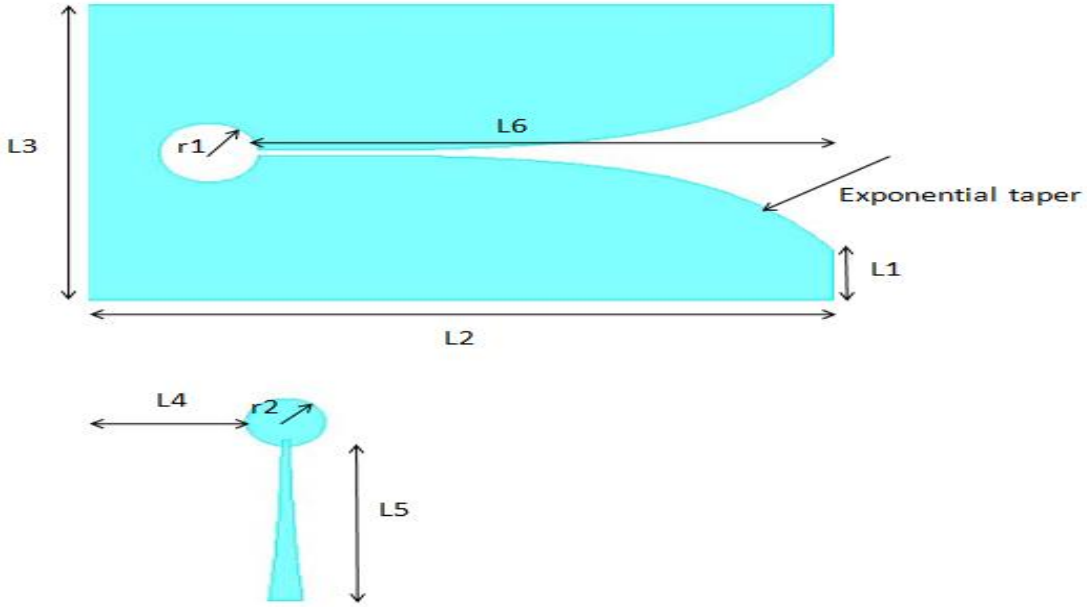

Figure 7.13 Layout of UWB vivaldi antenna (L1=9 mm, L2=75 mm, L3=51 mm, L4=8 mm, L5=22 mm, L6=58 mm, r1=5 mm, r2=3.5 mm)

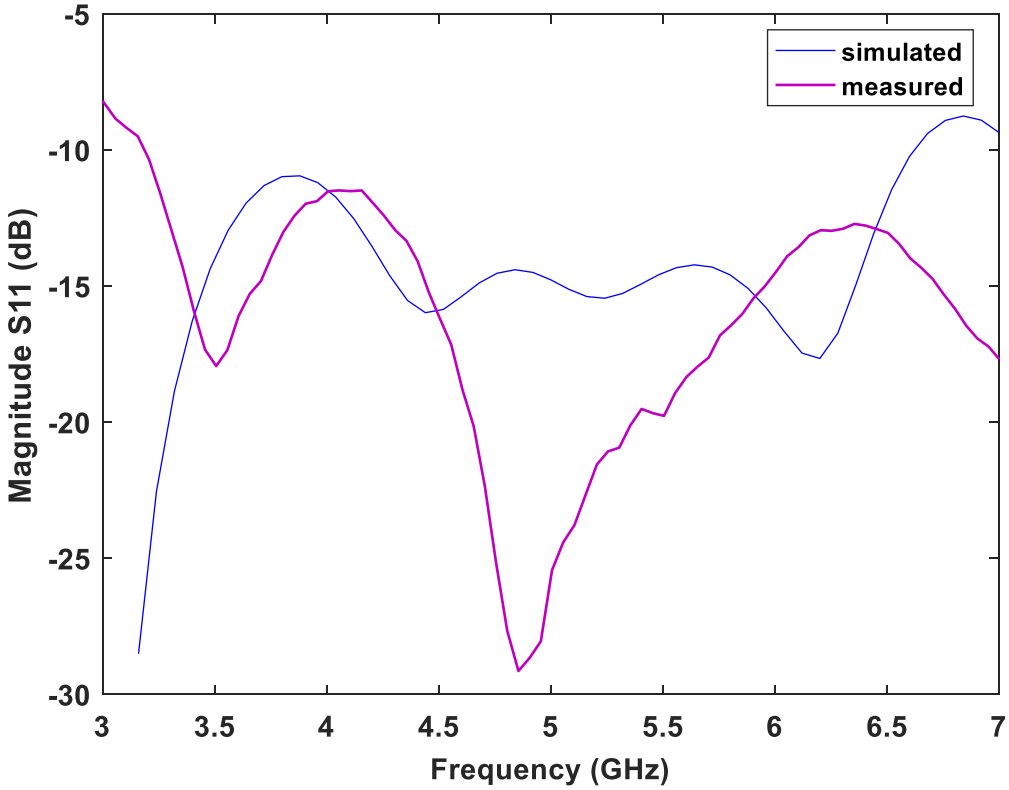

Figure 7.14 Simulated and measured return loss of Vivaldi antenna

The transmitter is fixed at an angle $\phi = 70^{o}$ to ensure that $\beta = 90^{o}$ during measurements. The four signals resulting after combination with the coherent carrier are applied to four logarithmic fast power detectors designed using Analog Devices AD8318 IC, which maintains accurate log conformance for signals of 1 MHz to 6 GHz and provides useful operation to 8 GHz using a single supply voltage of 5 V. The AD8318 IC is chosen for its 17 ns rise time (measured), which makes it more than twenty times faster than the Mini-Circuits ZX47-55-S power detectors previously used during proof of concept demonstration in Chapter 6. Consequently, the AD8318 can detect the envelope of signals having 3-dB bandwidth of up to 20 MHz. As a matter of fact, measurements are carried out for multiple modulation schemes at data rate of 20 MS/s.

7.4.2 Data recovery and demodulation at 5 GHz

During measurements, the transmitter is fixed at a distance *d* of 2 m from the receiver, and the stream of transmitted bits is created through the Agilent E4438C data pattern generator with a pseudorandom bit sequence (PSBR) $2^9 - 1$, before being modulated with different PSK/M-QAM modulation schemes. Data rate during experiments was set to 20 MS/s. The power generated by the vector signal generator is set to P_t = 10 dBm. Considering propagation in free-space, the path loss *FSPL* is linked to distance between the transmitter and receiver *d*, and the gain of the transmitting and receiving antennas (G_t and G_r) through (7.1):

For G_t = 6 dBi, G_r = 5.7 dBi, f = 5 GHz, and c = 3.108 m/s. The average received power P_r at each receiving antenna is:

$$P_r = P_t - FSPL = 10 - 40 \approx -30 dBm \tag{7.4}$$

During measurements, no low-noise amplifiers are used at the receiving antennas, and all modulations are processed successfully with a received power of about -30 dBm, which clearly highlights the promising performance of the proposed architecture to act as a low-power receiver, for use in applications requiring long-life batteries such as IoT sensors.

For every modulation scheme (QPSK, 8-PSK, QAM-16, and QAM-64), a train of 2000 received symbols is captured for further processing using MATLAB in order to obtain the average EVM. As depicted in Figure 7.16, multiple PSK (QPSK and 8-PSK at in Figure 7.16 (a) and (b), respectively) and QAM (16-QAM and 64-QAM in Figure 7.16 (c) and (d), respectively), are processed successfully through the fabricated prototype at 5 GHz, with EVM results reported in Table 7.4.

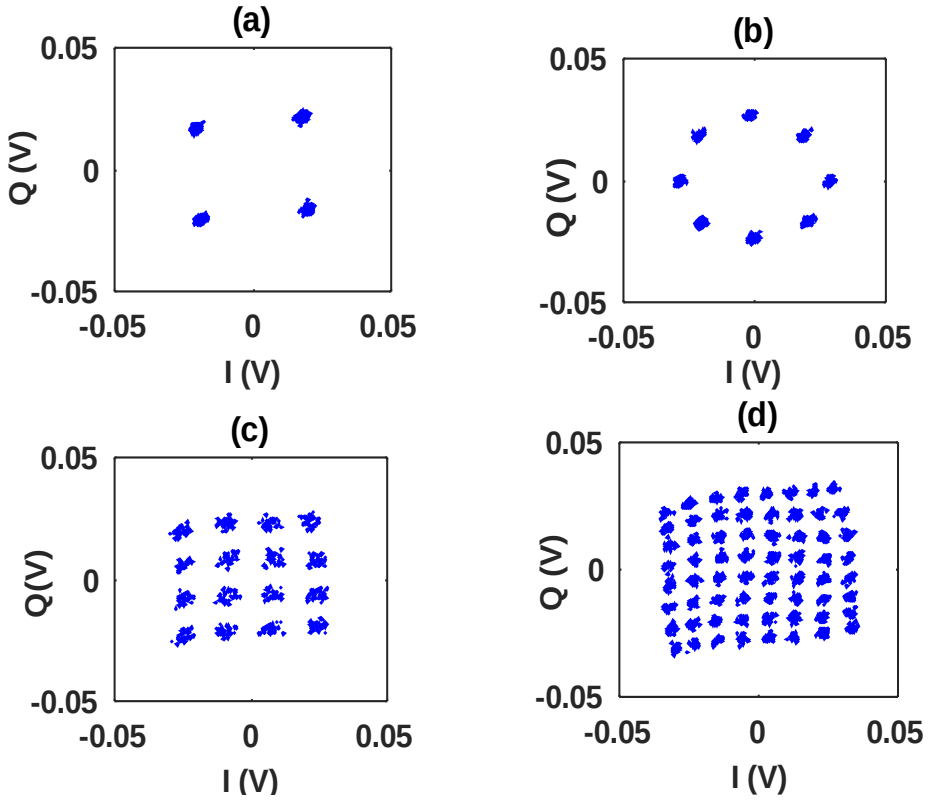

Figure 7.15 Received constellation for : (a) QPSK, (b) 8-PSK, (c)16-QAM, (d) 64-QAM

Table 7.4 Measured EVM at 20 MS/s and received power of -30 dBm

Modulation	**Data rate**	**EVM**
QPSK	40 Mb/s	2.1 %
8-PSK	60 Mb/s	3.12 %
16-QAM	80Mb/s	4.67 %
64-QAM	120 Mb/s	8.9 %

7.5 Conclusion

In this chapter, further measurement results are reported for the proposed spatially distributed multi-input interferometer receiver. In fact, received constellation for different modulation

schemes are reported at different received power levels. Then a low rise time power detector is designed and fabricated using the commercial Analog Devices AD8318 IC. This logarithmic power detector is experimentally studied in order to determine its de-embedded rise time and dynamic range. Moreover, measurements are carried out at data rate of 20 MS/s, which is equivalent to 120 Mb/s in the case of 64-QAM. The measured EVM for all modulation schemes is found to be less than 9 %, which confirms the feasibility of using the proposed receiver architecture for low-power communication systems to be adopted within the next generation of wireless systems. Finally, it is worth mentioning that obtained results concerned EVM can be further enhanced, by applying linearization algorithms that take into account hardware non-idealities and apply corrections using proper calibration models widely studied in the literature.

CHAPTER 8 JOINT DEMODULATION AND ANGLE OF ARRIVAL DETECTION

In the previous chapter, the proposed spatially distributed multi-input interferometer receiver is only studied at one angle of arrival, which creates the required 90^o phase difference between wave fronts at the input of four receiving antennas. Although, this is enough for good operation in the case of point-to-point communications, for which it is easy to fix both the transmitter and receiver at any required angle of arrival. It is necessary to study the ability of the proposed architecture to properly recover received data at any angle of arrival. In this chapter, we propose an algorithm that enables the proposed receiver architecture to properly and jointly demodulate data and detect the angle of arrival.

8.1 Demodulation at unknown angle of arrival

In the previous chapters, the transmitter and receiver are spatially set in a way to ensure that the phase difference between wave fronts at the input of consecutive receiving antennas is 90^o. And it is shown that as the angle of arrival ϕ deviates from the optimal $\phi_{90,}$ the bit error rate increases with the absolute value of deviation. This is illustrated by simulation results in Figure 8.1 for the received QPSK at SNR = 10 dB, for different angle of arrival when the inter-element distance is equal to 0.75 λ_0, where λ_0 is the free-space wavelength relative to the frequency of operation.

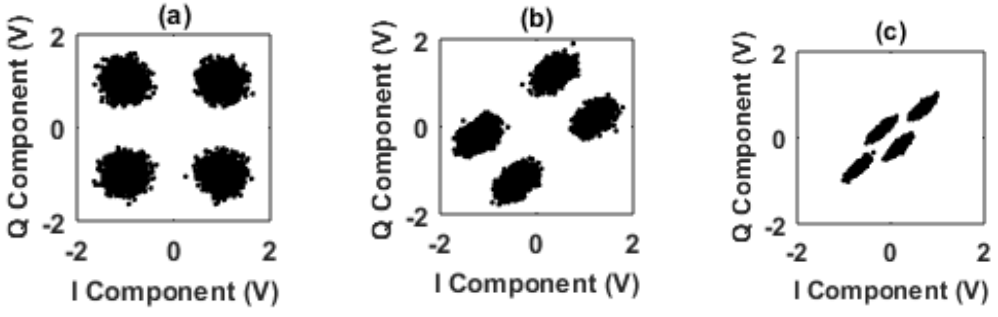

Figure 8.1 Received QPSK constellation for (a) ϕ =70^o, (b) ϕ =76^o, (c) ϕ =81^o

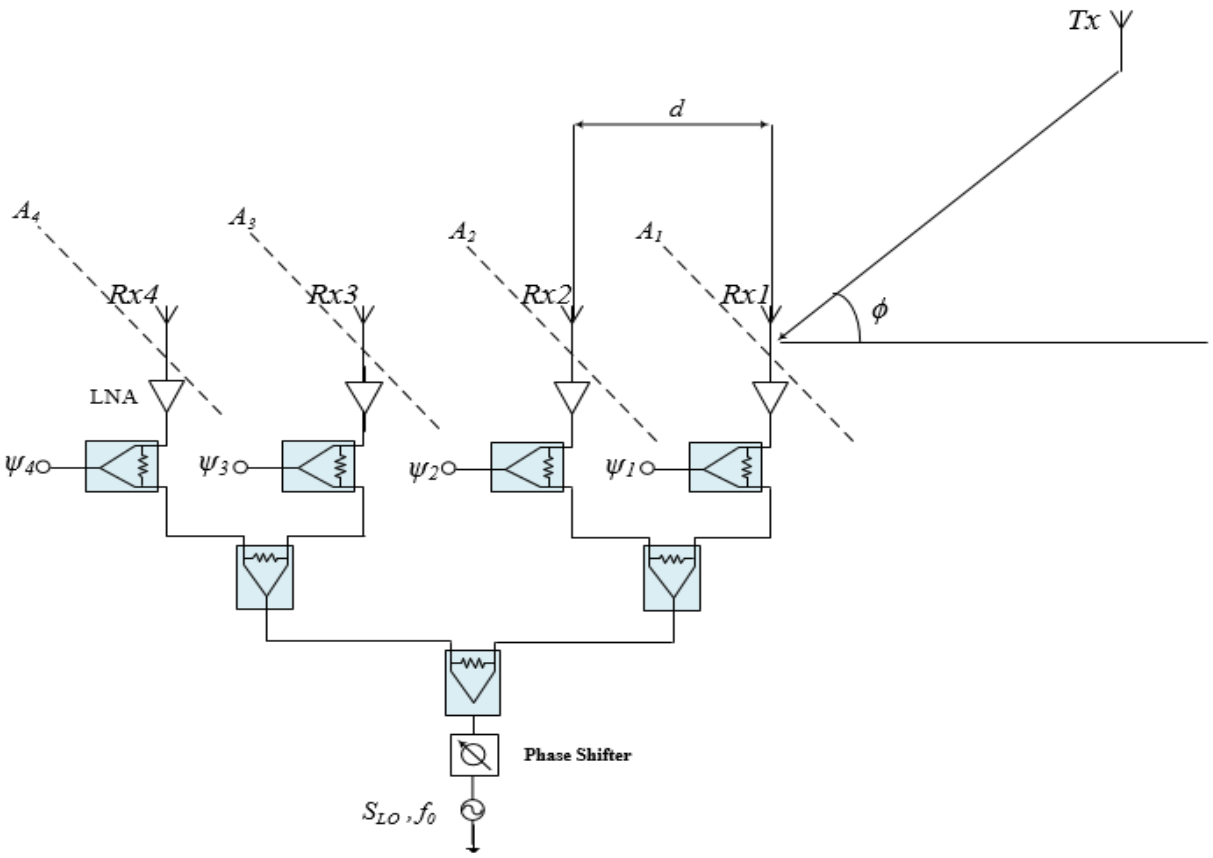

Figure 8.2 Schematic of the multi-input interferometer receiver for reception at unknown AoA

In order to get the mathematical formula for the received baseband signal at an unknown angle of arrival ϕ, let us consider the normalized received RF modulated signal $A_1(t)$ at antenna *Rx1* (after low-noise amplifier LNA) and the local oscillator signal $S_{LO}(t)$ to be defined as:

$$A_1(t) = \alpha(t).a.\exp(j(2\pi ft + \theta(t))) \tag{8.1}$$

$$S_{LO}(t) = a.\exp(j(2\pi ft + \theta_0)) \tag{8.2}$$

where $\alpha(t).\exp(j(\theta(t))$ is the instantaneous baseband modulated signal to be transmitted, which is modulated in amplitude and phase by $\alpha(t)$ and $\theta(t)$, respectively. The carrier signals used at the transmitter and receiver are given by $a.\exp(j(2\pi ft))$ and $a.\exp(j(2\pi ft+\theta_0))$, respectively. The phase difference between the transmitter and receiver carrier is set to be equal to θ_0. After LNAs, the normalized signals at antennas *Rx2*, *Rx3* and *Rx4* can be expressed as:

$$A_2(t) = A_1(t).\exp(-j\beta) \tag{8.3}$$

$$A_3(t) = A_1(t).\exp(-2j\beta) \tag{8.4}$$

$$A_4(t) = A_1(t).\exp(-3j\beta) \tag{8.5}$$

where β is the phase difference between wave-fronts and is expressed as :

$$\beta = 2\pi d\cos(\phi)/\lambda_0 \tag{8.6}$$

After combining the received RF signals at four antennas with the same reference LO following the circuit scheme presented in Figure 8.2, the four waves($\psi_i(t), i=1,2,3,4$) at the input of the power detectors can expressed using the following equations:

$$\begin{aligned}\psi_1(t) &= \frac{A_1(t)}{\sqrt{2}} + \frac{S_{LO}(t)}{2\sqrt{2}} \\ &= \frac{a.\exp(j(2\pi ft+\theta_0))}{\sqrt{2}}.\left(\frac{1}{2}+\alpha(t).\exp(j\Delta\theta(t))\right)\end{aligned} \tag{8.7}$$

$$\begin{aligned}\psi_2(t) &= \frac{A_1(t).\exp(-j\beta)}{\sqrt{2}} + \frac{S_{LO}(t)}{2\sqrt{2}} \\ &= \frac{a.\exp(j(2\pi ft+\theta_0))}{\sqrt{2}}.\left(\frac{1}{2}+\alpha(t).\exp(j\Delta\theta(t)-\beta)\right)\end{aligned} \tag{8.8}$$

$$\psi_3(t) = \frac{A_1(t).\exp(-2j\beta)}{\sqrt{2}} + \frac{S_{LO}(t)}{2\sqrt{2}} = \frac{a.\exp(j(2\pi ft + \theta_0))}{\sqrt{2}}.\left(\frac{1}{2} + \alpha(t).\exp(j\Delta\theta(t) - 2\beta)\right) \tag{8.9}$$

$$\psi_4(t) = \frac{A_1(t).\exp(-j3\beta)}{\sqrt{2}} + \frac{S_{LO}(t)}{2\sqrt{2}} = \frac{a.\exp(j(2\pi ft + \theta_0))}{\sqrt{2}}.\left(\frac{1}{2} + \alpha(t).\exp(j\Delta\theta(t) - 3\beta)\right) \tag{8.10}$$

where $\Delta\theta(t)$ is defined as the phase difference between the LO reference signal and $A_1(t)$

$$\Delta\theta(t) = \theta(t) - \theta_0 \tag{8.11}$$

Power detectors operating under their square law-region ($V_i(t) = K\left|\psi_i(t)\right|^2, i = 1,2,3,4$), are used to get dc output voltages as follows:

$$V_1(t) = \frac{K.a^2}{2}\left(\frac{1}{4} + \alpha(t)^2 + \alpha(t).\cos(\Delta\theta(t))\right) \tag{8.12}$$

$$V_2(t) = \frac{K.a^2}{2}\left(\frac{1}{4} + \alpha(t)^2 + \alpha(t).\cos(\Delta\theta(t) - \beta)\right) \tag{8.13}$$

$$V_3(t) = \frac{K.a^2}{2}\left(\frac{1}{4} + \alpha(t)^2 + \alpha(t).\cos(\Delta\theta(t) - 2\beta)\right) \tag{8.14}$$

$$V_4(t) = \frac{K.a^2}{2}\left(\frac{1}{4} + \alpha(t)^2 + \alpha(t).\sin(\Delta\theta(t) - 3\beta)\right) \tag{8.15}$$

Consequently, we can define the received in-phase and quadrature components, I_r(t) and Q_r(t) as follows:

$$\begin{aligned} I_r(t) &= \frac{K.a^2}{2}\alpha(t).\left(\cos(\Delta\theta(t)) - \cos(\Delta\theta(t) - 2\beta)\right) \\ &= K.a^2.\alpha(t).\cos(\Delta\theta(t)).\sin^2(\beta) \\ &+ K.a^2.\alpha(t).\sin(\Delta(\theta(t)).\cos(\beta).\sin(\beta) \end{aligned} \tag{8.16}$$

$$\begin{aligned} Q_r(t) &= \frac{K.a^2}{2}\alpha(t).\left(\cos(\Delta\theta(t) - \beta) - \cos(\Delta\theta(t) - 3\beta)\right) \\ &= K.a^2.\alpha(t).\cos(\Delta\theta(t)).\sin(2\beta).\sin(\beta) \\ &- K.a^2.\alpha(t).\sin(\Delta(\theta(t)).\cos(2\beta).\sin(\beta) \end{aligned} \tag{8.17}$$

The received signals I_r(t) and Q_r(t) are linked to the transmitted components ($\alpha(t).\cos(\Delta\theta(t))$ and $\alpha(t).\sin(\Delta\theta(t))$) through the following matrix representation:

$$\begin{bmatrix} I_r(t) \\ Q_r(t) \end{bmatrix} = K.a^2.\begin{pmatrix} \sin^2(\beta) & \cos(\beta).\sin(\beta) \\ \sin(2\beta).\sin(\beta) & -\cos(2\beta).\sin(\beta) \end{pmatrix}\begin{bmatrix} \alpha(t).\cos(\Delta\theta(t)) \\ \alpha(t).\sin(\Delta\theta(t)) \end{bmatrix} \tag{8.18}$$

Without loss of generality and for simplicity of computation, we will consider $k.a^2 = 1$ (with unity of Volt).

Hence, the transformation matrix M, relating the received and transmitted signals can be easily expressed as :

$$M = \begin{pmatrix} \sin^2(\beta) & -\cos(\beta).\sin(\beta) \\ \sin(2\beta).\sin(\beta) & -\cos(2\beta).\sin(\beta) \end{pmatrix} \tag{8.19}$$

In fact, symbols which are known at the transmitter and receiver (pilot or training symbols) are to be used, in order to get the coefficients of *M*. Then, if *M* is invertible ($\det(M) \neq 0$), the transmitted signal can be recovered using the inverse of M and the received components (I_r(t) and Q_r(t))

Moreover, the transformation matrix *M* in (8.19) is only a function of the phase difference β. therefore through some trigonometric manipulations, the determinant of *M* can be easily expressed as:

$$\det(M) = \sin^3(\beta) \tag{8.20}$$

8.2 Ambiguity analysis for angle of arrival

The determinant of matrix *M* equals zero for certain values of phase difference β. Since β is a function of the angle of arrival ϕ, and it is a periodic function with period 2π, then it is possible to establish a one-to-one function between β and ϕ, for the values of β within the interval $[-\pi, \pi]$.

$$\det(M) = 0 \rightarrow \sin^3(\beta) = 0 \rightarrow \beta = k\pi; k \in Z \tag{8.21}$$

The angle of arrival values for which $\beta = k\pi; k \in Z$ as stated in (8.20) do not allow the demodulation of received RF signals. In fact, for these AoA values, the transformation matrix *M* becomes singular (det(*M*)=0), and thus we call them dead angles as illustrated in Figure 8.3.

For example, when the inter-element distance is equal to 0.5 λ_0, demodulation fails for three values of ϕ ($\phi = 0^o$ with $\beta=180^o$, $\phi = 90^o$ with $\beta=0^o$ and $\phi = 180^o$ with $\beta=-180^o$).

For these AoA values, the waves at the input of receiving antennas *Rx1* and *Rx3* are in phase ($2\beta = 2k\pi; k \in Z$).

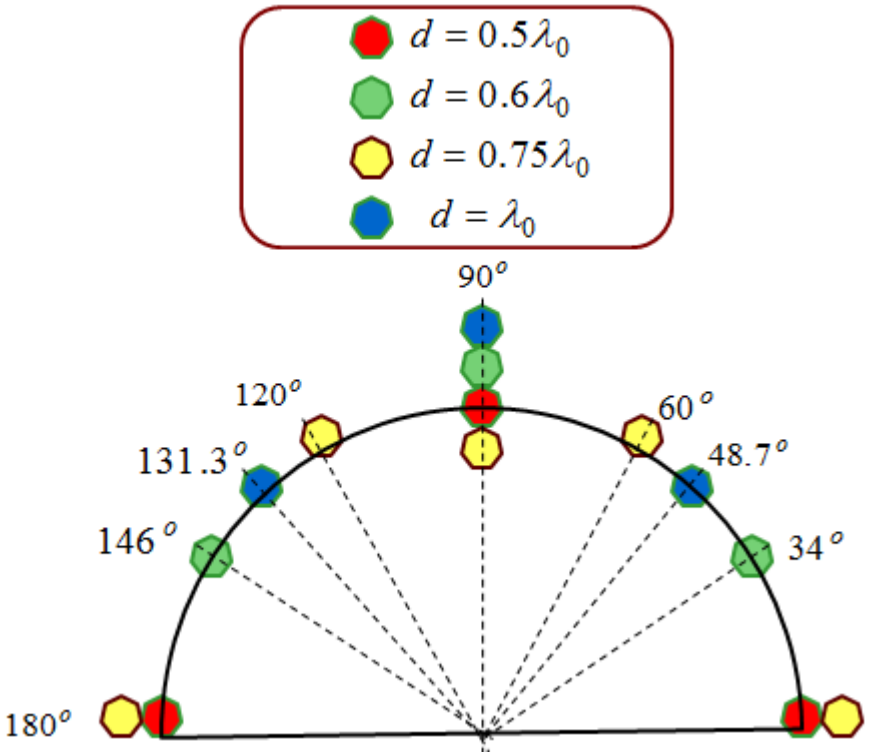

Figure 8.3 Dead angles as a function of the inter-element distance between receiving antennas

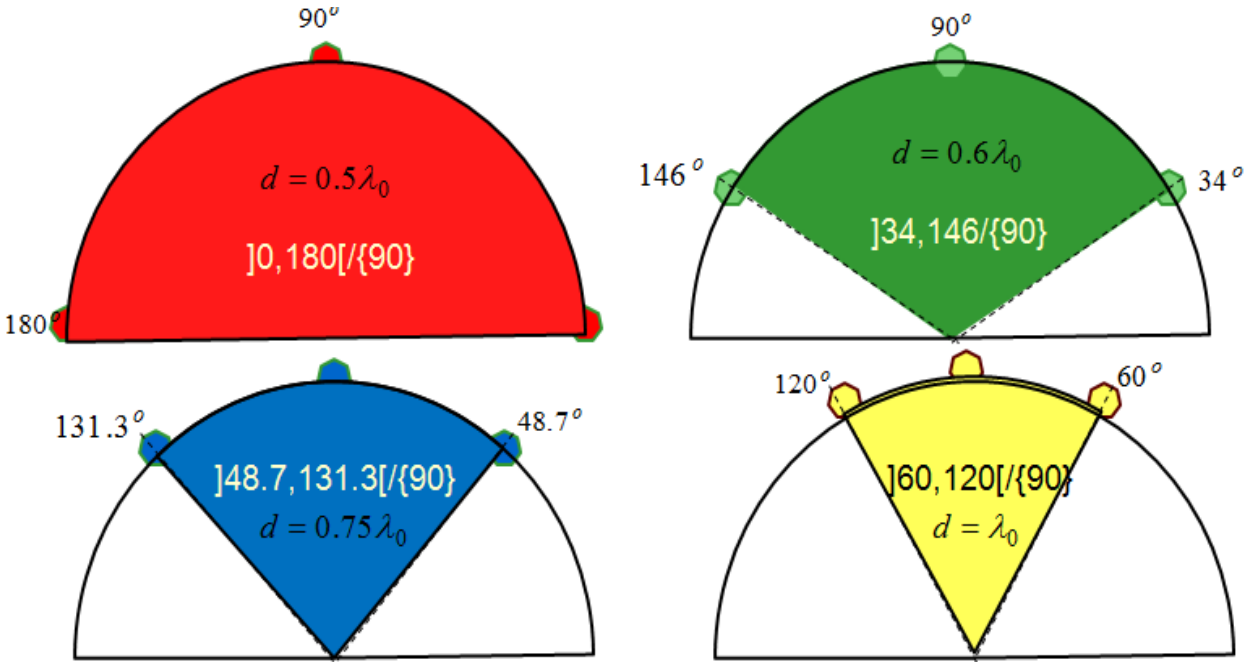

Figure 8.4 Angle of arrival ambiguity- free detection range

And as these waves are in-phase, then the dc output voltages will be equal which makes the received in-phase and quadrature components equal to zero as highlighted by the following equations, when $\beta = k\pi; k \in Z$:

$$I_r(t) = \frac{K.a^2}{2}\alpha(t).\left(\cos(\Delta\theta(t)) - \cos(\Delta\theta(t) - 2\beta)\right) = 0 \tag{8.22}$$

$$Q_r(t) = \frac{K.a^2}{2}\alpha(t).\left(\cos(\Delta\theta(t) - \beta) - \cos(\Delta\theta(t) - 3\beta)\right) = 0 \tag{8.23}$$

Consequently, all points of complex constellation relative to a specific modulation scheme will be received at the center of the complex plane. This explains why these specific AoA are called dead angles.

Figure 8.4 illustrates the ambiguity-free angle of arrival detection range for some values of the inter-element distance *d* between consecutive antennas at the receiver. In fact, for d=0.5 λ_0, the ambiguity-free AoA interval extends from 0^o to 180^o (excluding 90^o, for which all wave fronts will be in phase at the input of receiving antennas).

As the inter-element distance increases, the ambiguity-free AoA detection range shrinks. This can be easily seen in the case of an inter-element distance d= λ_0, where the AoA can be detected with no ambiguity within the interval [60^o, 120^o] / {90^o}.

8.3 Angle of arrival detection using training symbols

As stated before, within the ambiguity-free detection range, there is a one-to-one function which links the phase difference β to the angle of arrival ϕ. The first step is to find the phase difference β using received training symbols (known at both the transmitter and receiver).

In fact, let us consider two transmitted symbols $s1 = \alpha 1.e^{j\theta 1}$ and $s2 = \alpha 2.e^{j\theta 2}$. At the receiver, the symbols detected are $r_1 = m_1 + jn_1$ and $r_2 = m_2 + jn_2$. When $\theta_0 = 0^o$, the received in-phase and quadrature components of these received symbols are expressed as:

$$m1 = \alpha 1.\cos(\theta 1).\sin^2(\beta) - \alpha 1.\sin(\theta 1).\cos(\beta).\sin(\beta) \tag{8.24}$$

$$m2 = \alpha 2.\cos(\theta 2).\sin^2(\beta) - \alpha 2.\sin(\theta 2).\cos(\beta).\sin(\beta) \tag{8.25}$$

$$n1 = \alpha 1.\cos(\theta 1).2\sin^2(\beta).\cos(\beta) - \alpha 1.\sin(\theta 1).\cos(2\beta).\sin(\beta) \tag{8.26}$$

$$n2 = \alpha 2.\cos(\theta 2).2\sin^2(\beta).\cos(\beta) - \alpha 2.\sin(\theta 2).\cos(2\beta).\sin(\beta) \tag{8.27}$$

If we choose $\theta_1 = -\theta_2$, then we can determine $\sin(\beta)$ and $\cos(\beta)$ through the following formula:

$$\sin(\beta) = \pm\sqrt{\frac{(m1+m2)}{(\alpha 1+\alpha 2).\cos(\theta 1)}} \tag{8.28}$$

$$\cos(\beta) = \frac{(n1+n2)}{2(m1+m2)} \tag{8.29}$$

In order to overcome the ambiguity relative to the sign of sin (β), a simple verification using both possible values of sin (β) in (8.23) would determine the right sign. Once both the sine and cosine of the phase difference β are determined, then the angle of arrival ϕ is determined as well.

Finally, once the phase difference β is determined within the ambiguity-free detection interval using training symbols, the transformation matrix M can be inverted in order to recover the unknown transmitted symbols. This process can be easily updated every frame duration in order to track any change in the direction of arrival of transmitter, or to receive a different data stream coming from another transmitter located at a different angle from the receiver.

A simple training sequence to be used in order to determine the phase difference and angle of arrival could be defined as a sequence of BPSK modulation symbols ($s1 = e^{j\pi/2}$ and $s2 = e^{-j\pi/2}$) following the pre-defined condition (θ_1 = -θ_2) or any two symmetrical points from a PSK constellation. Figure 8.5 illustrates noise-free simulation results for the application of the proposed method aiming to determine the angle of arrival using a training sequence of BPSK symbols and make correct the received QPSK constellation by inverting the transformation matrix M. Simulations are carried out for an inter-element distance d=0.5 λ_0.

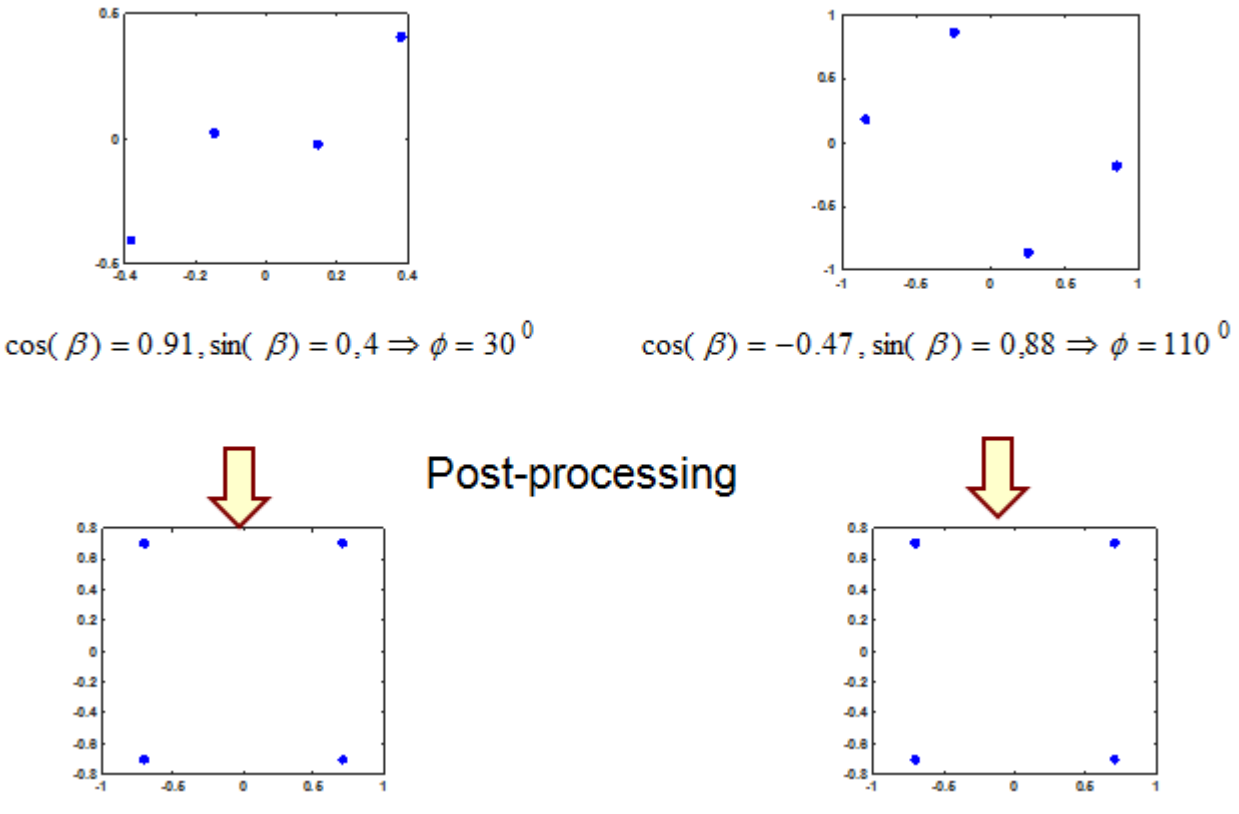

Figure 8.5 AoA detection and correction of received QPSK constellation using training sequence

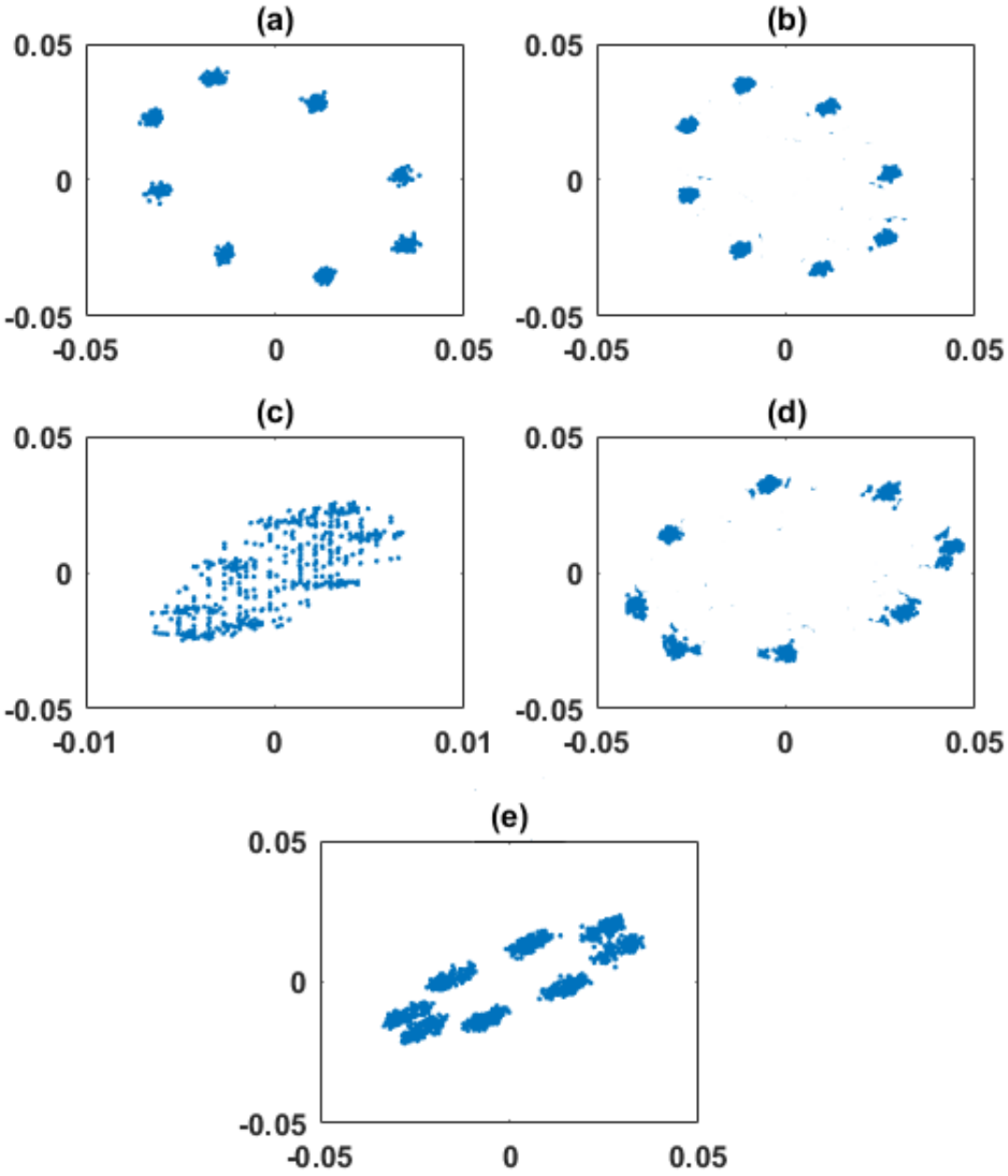

Figure 8.6 Received 8-PSK:(a) AoA=80^o, (b) AoA=75^o, (c) AoA=90^o,(d) AoA=60^o,(e) AoA =50^o

Measurements are performed using the same experimental setup in the previous chapter with the same constraints of transmitter-receiver separation distance, transmitted power, and an inter-element distance between receiving antennas d=0.75λ_0. As depicted in Figure 8.6, the shape of the received 8-PSK constellation depends on the value of the angle of arrival.

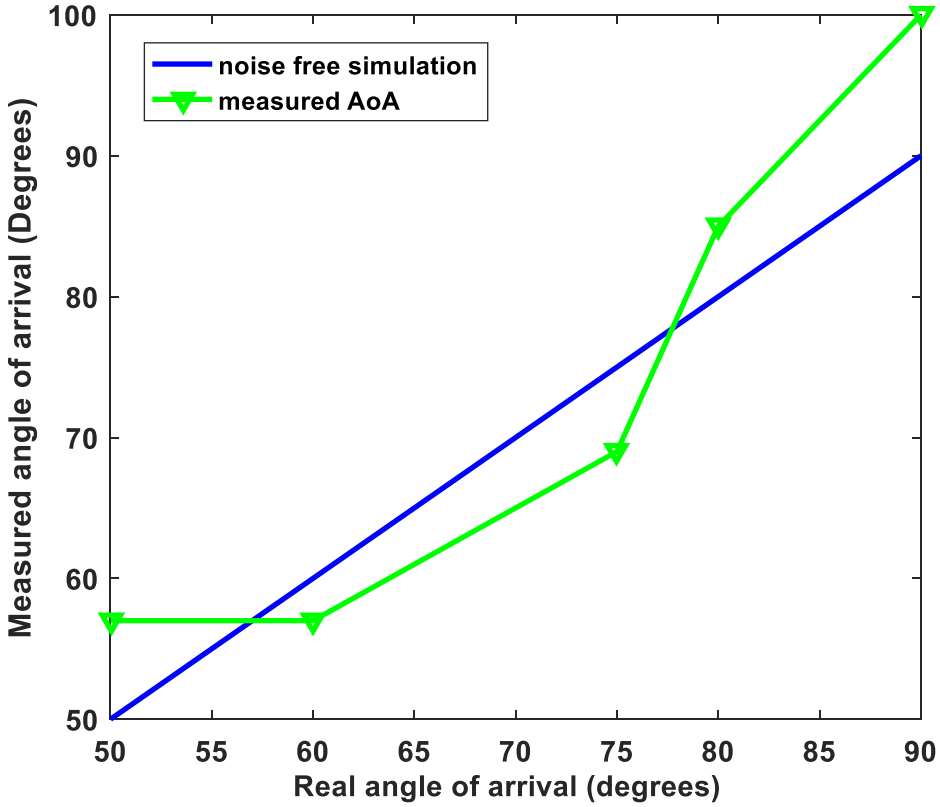

Figure 8.7 Measurement results for AoA using the proposed method

The original transmitted baseband in-phase and quadrature components for 8-PSK are directly obtained through the vector signal generator I-out and Q-out external ports. Then, the proposed method is applied to the received constellation by averaging the obtained angle of arrival over symmetrical points of 8-PSK constellation. As depicted in Figure 8.7, there is a good agreement between simulation (noise-free) and measurement results for AoA detection using the proposed algorithm, with an average error of less than 11 %.

8.4 Conclusion

In this chapter, we propose a method for measuring the angle of arrival for an RF signal that exploits symbols known at both the transmitter and receiver, in order to deduce the phase difference between wave fronts at the input of antenna elements in the multi-input interferometer

receiver. A mathematical modeling is presented to explain how this method is implemented, along with a study of the ambiguity-free detection range. Then, an experimental validation is carried out in order to prove the feasibility of the proposed method. Measurements results show and confirm the validity of the proposed method, and could be enhanced at higher values of the signal to noise ratio and using linearization techniques to overcome hardware imperfections.

CHAPTER 9 CONCLUSION AND RECOMMANDATIONS

In this chapter, we briefly summarize the main research outcomes and contributions of this thesis. There exist, however, some pending questions and extensions to the work presented in this thesis. In this regard, we also suggest some areas in which further research could be conducted in order to enhance the performance of the proposed architecture in terms of flexibility of operation and/or achievable data rate.

9.1 Summary

This thesis presents a comprehensive framework including modeling, mathematical analysis along with simulation and experimental validation of a novel spatially distributed multi-input interferometer receiver for 5G wireless systems and beyond. The proposed receiver architecture inherits the same advantages of conventional six-port receivers, which have been widely used, since their first introduction in 1994. In fact, six-port technique is used in various RF applications including direct conversion demodulation, angle of arrival of detection, automobile radar systems, the monitoring of vital signals as well as in the design of multifunctional multi-port architectures. The proposed receiver architecture in this thesis operates at low RF power levels, while presenting only 3 dB of loss, compared to the 6 dB and more natural loss of six-port receivers.

This multi-input interferometric receiver architecture is based on the use of a set of equally-spaced antenna elements, which receive phased versions of the same RF modulated signal. And if the receiving elements are properly fixed, in order for the phase difference to be equal to 90^{o}, each of the signals at the input of the receiving antennas is to be combined with a coherent carrier. Then, power detectors operating under their square law-region are used to get dc voltages, which are proportional to the power of waves at their inputs. These voltages are combined in a simple way to extract directly the in-phase and quadrature data streams of the received RF modulated signal.

The mathematical modeling of the demodulation process for the proposed receiver architecture is first studied. And the analysis of major factors affecting the demodulation performances for the

proposed receiver are presented in this thesis, such as coupling effect between receiving antennas on bit error rate, effect of carrier frequency offset between local oscillators at the transmitter and receiver, and bit error rate performance analysis as a function of received SNR for different angle of arrival values.

In addition, different PSK/QAM modulations schemes have been successfully recovered using an experimental prototype, which is fabricated to operate around the center frequency of 5 GHz. Comparison in terms of EVM with state-of-the-art six-port receiver demodulation results, show that the proposed architecture presents a promising candidate for future low-power wireless communication systems.

The first prototype developed in this thesis was based on the use of commercial off-the shelf power detectors from mini-circuits, which have a rise time of about 400 ns. These detectors cannot process modulated signals with bandwidth higher than 1 MHz, which explains the measurements results reported at a speed of 1 MS/s. As a matter of fact, another power detector based on the low rise time Analog devices AD8318 logarithmic power detector is designed, fabricated and experimentally characterized in terms of dynamic range and rise time. This detector has a measured rise time of about 17 nanoseconds, which enables the recovery and processing of RF modulated signals with bandwidth up to 20 MHz. Measurements are carried out at higher data rate using the new power detector, which enabled the successful recovery of multiple QAM signals at the speed of 120 Mb/s in the case of 64-QAM.

Moreover, a new method for the angle of arrival detection is proposed in this thesis, based on the use of a training sequence and the extraction of the phase difference between receiving antennas, which is linked to the direction of arrival through a one-to-one function within the ambiguity-free detection range. Simulation and measurement results are reported in order to confirm the feasibility of this method in the context of angle of arrival detection. Thus, the proposed spatially distributed multi-input interferometer receiver is proved to be a promising architecture for joint demodulation and angle of arrival detection, which are critical features for future multi-functional future receiver structures.

9.2 Recommendations for future works

The research effort presented in this work automatically exposes many tasks which require attention. In fact, the proposed architecture can be further studied and investigated taking into account the following recommendations:

- Dual-polarized systems are very important in wireless communications systems. In fact, two independent data streams can be carried over two orthogonal polarizations (vertical and horizontal) in the aim of doubling data rates. However, this must be carefully studied in terms of cross-polarization level, in order to mitigate the cross-talk between both polarizations, which could dramatically deteriorate the EVM of received signals over both polarized wireless channels. As a matter of fact, the proposed spatially distributed multi-input interferometer receiver can take advantage of polarization diversity in order to increase data rate or to decrease the bit error rate, when sending the same data stream over both polarizations (creating redundancy) and apply the well-known spatial diversity techniques, such as selection diversity, equal gain combining or maximum ratio combining, to enhance the received signal to noise ratio at the receiver.
- 5G wireless systems are required to operate at both microwave and millimeter wave frequencies. Indeed, microwave frequencies are the carriers for signals relative to users moving at high-speed in order to avoid the delay caused by handovers when crossing cell boundaries. Consequently, we suggest that the proposed architecture should be scaled and implemented at millimeter wave spectrum, such 28-, 38 and 60 GHz. At such frequencies, the wavelength is at least an order of magnitude smaller than microwave carriers, which makes easy the integration of the whole receiver within compact PCB structures. And thus multiple functionalities could be implemented within a relatively compact architecture.
- The work performed in this thesis focused on the fundamental characteristics of the proposed receiver architecture, while using a single antenna array, composed of four equally-spaced elements. However, we strongly believe that with a 2D antenna array, multiple functions can be operating simultaneously, such as energy harvesting, 2D angle

of arrival detection using two orthogonal sets of antennas in a 2D array, Doppler frequency detection, beam forming using sub-sets of the whole 2D array etc.

- During the experimental investigation of the proposed receiver, a critical feature was noticed, which is the effect of hardware impairments on the quality of recovered baseband signals. Hence, we strongly believe that future work must include the modeling and calibration of the whole receiver, using state-of-the-art linearization techniques and algorithms which are widely adopted for conventional six-port receivers.
- In the context of cognitive wireless systems, receivers must be able to reconfigure its frequency of operation on the fly at different frequency bands. This is usually done when the conditions of a given channel are deteriorated because of excessive interference level, and the change to operate at a different frequency band becomes a must. Thus, we believe that the proposed spatially distributed receiver structure should be studied and implemented in the context of cognitive radio systems.
- The proposed multi-input interferometer receiver could be also used in the context of MIMO communications. This would increase considerably the expected data rate, while using the same set of receiving antennas, and implementing signal processing algorithms to extract independent data streams.
- Finally, it is also recommended to exploit the features of RFIC design in order to implement the proposed architecture at millimeter-waves, rather than adopting conventional PCB design. In fact, RFIC design techniques offer very competitive advantages such ultra-compact design, low-cost, and low-power consumption.

REFERENCES

[1] T. S. Rappaport, *Wireless Communications*: *Principles and Practice*, Prentice Hall, 2001.

[2] A. Goldsmith, *Wireless Communications*: Cambridge University Press, 2005.

[3] S. Tabbane, *Handbook of Mobile Radio Networks*: Artech House Publishers, 2000.

[4] D. Tse and P. Viswanath, *Fundamentals of wireless communications*: Cambridge University Press, 2005.

[5] E. Dahlman, S. Parkvall, J. Skold, and P. Beming, *3G Evolution HSPA and LTE for Mobile Broadband,* Academic Press, 2008.

[6] M. Elkashlan, T. Q. Duong, and H.-H. Chen, "Millimeter-wave communications for 5G: fundamentals: Part I," *IEEE Communications Magazine,* vol. 52, pp. 52-54, 2014.

[7] M. Elkashlan, T. Q. Duong, and H.-H. Chen, "Millimeter-wave communications for 5G, Part 2: applications," *IEEE Communications Magazine,* vol. 53, pp. 166-167, 2015.

[8] A. I. Sulyman, A. Alwarafy, G. R. MacCartney, T. S. Rappaport, and A. Alsanie, "Directional Radio Propagation Path Loss Models for Millimeter-Wave Wireless Networks in the 28-, 60-, and 73-GHz Bands," *IEEE Transactions on Wireless Communications,* vol. 15, pp. 6939-6947, 2016.

[9] H. Zhao, *et al*., "28 GHz millimeter wave cellular communication measurements for reflection and penetration loss in and around buildings in New York City," in *Proc. IEEE Int. Conf. Commun.*, 2013, pp. 5163-5167.

[10] M. Alzenad, M. Z. Shakir, H. Yanikomeroglu, and M. S. Alouini, "FSO-Based Vertical Backhaul/Fronthaul Framework for 5G+ Wireless Networks," *IEEE Communications Magazine,* vol. 56, pp. 218-224, 2018.

[11] Document ITU-R IMT-2020/2 (Rev.1): "*Submission, evaluation process and consensus building for IMT-2020*", Feb. 2017.

[12] 3GPP TR38.901 V14.0.0: "*Study on channel model for frequencies from 0.5 to 100 GHz (Release 14)*", Mar. 2017.

[13] Draft new report ITU-R M. [IMT-2020.EVAL]: "*Guidelines for evaluation of radio interface technologies for IMT-2020*", Jun. 2017.

[14] M. Shafi et al., "5G: A tutorial overview of standards, trials, challenges, deployment, and practice," *IEEE J. Sel. Areas Commun.*, vol. 35, no. 6, pp. 1201–1221, Jun. 2017.

[15] A. F. Naguib, A. Paulraj, T. Kailath, "Capacity improvement with base-station antenna array in cellular CDMA", *IEEE Trans. Veh. Technol*., vol. 43, pp. 691-698, Aug. 1994.

[16] D. Shiu, G.J. Foschini, M.J. Gans, J.M. Kahn, "Fading correlation and its effect on the capacity of multielement antenna systems", *IEEE Trans. Commun.*, vol. 48, pp. 502-513, 2002.

[17] I.E. Telatar, "Capacity of multiple antenna Gaussian channels", *Eur. Trans. Telecommun*., vol. 10, pp. 585-595, 1999.

[18] D. S. Baum, D. Gore, R. Nabar, S. Panchanathan, K. V. S. Hari, V. Erceg, A. J. Paulraj, "Measurement and characterization of broadband MIMO fixed wireless channels at 2.5 GHz", *Proc. IEEE ICPWC*, pp. 203-206, 2000.

[19] R. Stridh, B. Ottersten, P. Karlsson, "MIMO channel capacity of a measured indoor radio channel at 5.8 GHz", *Proc. Asilomar Conf. Signals Systems and Computers*, vol. 1, pp. 733-737, 2000.

[20] J. P. Kermoal, L. Schumacher, P. E. Mogensen, K. I. Pedersen, "Experimental investigation of correlation properties of MIMO radio channels for indoor picocell scenarios", *Proc. IEEE VTC*, vol. 1, pp. 14-21, 2000.

[21] M. Joham, W. Utschick, J. Nossek, "Linear transmit processing in MIMO communications systems", *IEEE Trans. Signal Processing*, vol. 53, no. 8, pp. 2700-2712, Aug. 2005.

[22] T. L. Marzetta, "Noncooperative cellular wireless with unlimited numbers of base station antennas, " *IEEE Trans. Wireless. Commun.*, vol. 9, no. 11, pp. 3590–3600, Nov. 2010.

[23] H. Q. Ngo and E. G. Larsson, "No downlink pilots are needed in TDD massive MIMO, " *IEEE Trans. Wireless Commun*., vol. 16, no. 5, pp. 2921–2935, May 2017.

[24] F. Rusek, D. Persson, B. K. Lau, E. G. Larsson, T. L. Marzetta, O. Edfors, and F. Tufvesson, "Scaling up MIMO: Opportunities and challenges with very large arrays, " *IEEE Signal Process. Mag*., vol. 30, pp. 40–60, Jan. 2013.

[25] X. Gao, F. Tufvesson, O. Edfors, and F. Rusek, "Measured propagation characteristics for very-large MIMO at 2.6 GHz, " *in Proc. of the 46th Annual Asilomar Conference on Signals, Systems, and Computers*,, Pacific Grove, California, USA, Nov. 2012.

[26] J. Hoydis, C. Hoek, T. Wild, and S. ten Brink, "Channel measurements for large antenna arrays, " *in IEEE International Symposium on Wireless Communication Systems (ISWCS)*, Paris, France, Aug. 2012.

[27] H. Q. Ngo, E. G. Larsson, and T. L. Marzetta, "Energy and spectral efficiency of very large multiuser MIMO systems, "*IEEE Trans. Commun.*, vol. 61, pp. 1436–1449, Apr. 2013.

[28] Emil Björnson, Jakob Hoydis and Luca Sanguinetti , *Massive MIMO Networks: Spectral, Energy, and Hardware Efficiency*, Foundations and Trends in Signal Processing, 2017.

[29] J. Helander, K. Zhao, Z. Ying, and D. Sjöberg, "Performance Analysis of Millimeter-Wave Phased Array Antennas in Cellular Handsets," *IEEE Antennas Wireless Propag. Lett.*, vol. 15, pp. 504-507, 2016.

[30] J. Boccuzzi, M. Ruggiero, *Femtocells: Design and Applications*, McGraw-Hill, 2011.

[31] Park, S.-L. Kim, J. Zander, "Asymptotic behavior of ultra-dense cellular networks and its economic impact", *Proc. IEEE Glob. Commun. Conf. (GLOBECOM)*, pp. 4941-4946, 2014.

[32] S. Samarakoon et al., "Ultra Dense Small Cell Networks: Turning Density into Energy Efficiency", *IEEE JSAC*, vol. 34, no. 5, May 2016.

[33] M. Kamel et al., "Ultra-Dense Networks: A Survey", *IEEE communications surveys tutorials*, vol. 18, pp. 2522-2545, May 2016.

[34] J. Zander, "Beyond the Ultra-Dense Barrier: Paradigm Shifts on the Road Beyond 1000x Wireless Capacity", *IEEE Wireless Communications*, vol. 24, no. 3, pp. 96-102, Jan. 2017.

[35] Tue Bilen, Berk Canberk, Kaushik R. Chowdhury, "Handover Management in Software-Defined Ultra-Dense 5G Networks", *IEEE Network*, vol. 31, no. 4, July-August 2017.

[36] F. Rusek, D. Persson, B. Lau, E. Larsson, T. Marzetta, O. Edfors, and F. Tufvesson, "Scaling up MIMO: Opportunities and challenges with very large arrays, " *IEEE Signal Process. Mag.*, vol. 30, no. 1, pp. 40–60, 2013.

[37] H. Ngo, E. Larsson, and T. Marzetta, "Energy and spectral efficiency of very large multiuser MIMO systems, " *IEEE Trans. Commun.*, vol. 61, no. 4, pp. 1436–1449, 2013.

[38] E. Bjornson, M. Kountouris, and M. Debbah, "Massive MIMO and small cells: Improving energy efficiency by optimal soft-cell coordination, " in *Proc. Int. Conf. Telecommun. (ICT)*, 2013.

[39] J.R. Carson, Notes on the theory of modulation, *Proc. IRE*, vol. 10, no. 1, Feb. 1922.

[40] E. E. Djoumessi, S. O. Tatu, K. Wu, "Frequency-agile dual-band direct conversion receiver for cognitive radio systems", *IEEE Trans. on Microw. Theory and Techn.*, vol. 58, pp. 87-94, Jan. 2010.

[41] S. O. Tatu. "Nouveau récepteur six-port en ondes millimétriques". Ph.D.thesis, Montréal, École polytechnique, 2005.

[42] C. Hannachi, S. O. Tatu, "An Improved-Performance V-band Six-Port Receiver for Future 5G Short-Range Wireless Communications", *2017 IEEE Topical Conference on Wireless Sensors and Sensor Networks (WiSNet),* Phoenix, Arizona, January 15 – 18, 2017.

[43] C. Hannachi, E. Moldovan, Z. Ouardirhi, S. O. Tatu, "V-band Six-port Quadrature Demodulator : Error Vector Magnitude Analysis", *8th Global Symposium on Millimeter-Waves (GSMM2015),* Conference Proceedings, Montreal, Canada May 25-27, 2015.

[44] G.F. Engen, "The six-port reflectometer: an alternative network analyzer", *IEEE Trans. Microw. Theory Techn.*, vol. 25, no. 12, pp. 1075-1080, 1977.

[45] C. A. Hoer, "A network analyzer incorporating two six-port reflectometers", *IEEE Trans. Microw. Theory Techn*., vol. MTT-25, pp. 1070-1074, Dec. 1977.

[46] J. Li, R.G. Bosisio, K. Wu, "Six-port direct digital millimeter wave receiver", *Proc. of the IEEE MTT-S International Microwave Symp*., pp. 1659-1662, 1994.

[47] S. O. Tatu, E. Moldovan, K. Wu, R. G. Bosisio, "A new direct millimeter-wave six-port receiver", *IEEE Trans. Microw. Theory Techn*., vol. 49, no. 12, pp. 2517-2522, Dec. 2001.

[48] H. Nyquist, "Certain Factors Affecting Telegraph Speed," *Bell System Technical Journal*, p. 324, April 1924.

[49] Hartley, R. V. L., "Transmission of Information, " *Bell System Technical Journal*, p. 535, July 1928.

[50] C. E. Shannon, "A Mathematical Theory of Communication". *Bell System Technical Journal*, pp. 623–666, Oct. 1948.

[51] L. Han, "integrated communication and radar scheme for future intelligent transportation systems", Ph.D.thesis, Montréal, École polytechnique, 2011.

[52] A. Molisch, *Wireless Communications*, Wiley-IEEE Press, 2010.

[53] W. H. Tranter , K. S. Shanmugan, T. S. Rappaport, K. L. Kosbar, *Principles of Communication Systems Simulation with Wireless Applications*, Prentice Hall, 2003.

[54] A. Hasan, M. Helaoui, "Effort-reduced calibration of six-port based receivers for CR/SDR applications", *IEEE J. Emerg. Sel. Topics Circuits Syst,* vol. 3, no. 4, pp. 586-593, Dec. 2013.

[55] M. S. Alouini, "Adaptive and diversity techniques for wireless digital communications over fading channels", Ph.D. thesis, California Institute of Technology, 1998.

[56] R. A. Shafik, M. S. Rahman, A. R. Islam, "On the extended relationships among EVM BER and SNR as performance metrics", *Proc. Int. Conf. Elect. Comput. Eng*., pp. 408-411, Dec. 2006.

[57] C. Hannachi , and S. O. Tatu: Millimeter-wave Multi-Port Receivers Front-ends: Design considerations and Implementation, in book: *Electronic Circuit Principles, Architectures and Applications on Emerging Technologies*, ISBN 978-953-51-5837-0, 2018.

[58] Xinyu Xu; Bosisio, R.G.; Ke Wu, "Analysis and implementation of six-port softwaredefined radio receiver platform," *IEEE Trans. on Microw. Theory and Techn.*,vol.54, no.7, pp.2937-2943, July 2006.

[59] Chi-Hsueh Wang; Hong-Yeh Chang; Pei-Si Wu; Kun-You Lin; Tian-Wei Huang; Huei Wang; Chun Hsiung Chen, "A 60 GHz Low-Power Six-Port Transceiver for Gigabit SoftwareDefined Transceiver Applications," *IEEE International Solid-State Circuits Conference. Digest of Technical Papers.* , pp.192-596, 11-15 Feb. 2007.

[60] E. Moldovan, S. O. Tatu, "A 60 GHz Multi-Port Receiver with Analog Carrier Recovery for UWB WPAN", *European Microwave Week,* pp. 1779 - 1782, Amsterdam, October 27 - 31, 2008.

[61] C. Hannachi, S. O. Tatu, "Highly Isolated Broadband Five-port Circuit for V-Band High Data-rate Wireless Communications" *The 28th Annual IEEE International Symposium on Personal, Indoor and Mobile Radio Communications (IEEE PIMRC 2017)*, Montreal, QC, October 8 – 13, 2017.

[62] G. Vinci, A. Koelpin, F. Barbon, R. Weigel, "Six-port-based direction-of-arrival detection system*", Proc. Asia-Pacific Micro-wave Conf*, pp. 1817-1820, Dec. 2010.

[63] T. Hentschel, "The six-port as a communications receiver", *IEEE Trans. Microw. Theory Techn*., vol. 53, no. 3, pp. 1039-1047, Mar. 2005.

[64] G. Vinci, A. Koelpin, R. Weigel, "Employing six-port technology for phase-measurement-based calibration of automotive radar", *Asia Pacific Microwave Conference*, Dec. 2009.

[65] Gabor Vinci, Stefan Lindner, Francesco Barbon, Sebastian Mann, Maximilian Hofmann, Alexander Duda, Robert Weigel, Alexander Koelpin, "Six-Port Radar Sensor for Remote Respiration Rate and Heartbeat Vital-Sign Monitoring", *IEEE Microw. Theory and Techn.*, vol. 61, no. 5, pp. 2093-2100, 2013.

[66] D. Pozar, *Microwave Engineering*, Wiley, 2011.

[67] S. O. Tatu, E. Moldovan, K. Wu, R. G. Bosisio "Ka-band Analog Front-end for Software Defined Direct Conversion Receiver", *IEEE Trans. on Microw. Theory and Techn.*, vol. 53, no. 9, pp. 2768-2776, Sep. 2005.

[68] Ke Wu, "Multiport interferometer techniques for innovative transceiver applications", *IEEE Radio and Wireless Symposium (RWS) 2010*, pp. 531-534, 2010.

[69] Abul Hasan, Mohamed Helaoui, "Novel Modeling and Calibration Approach for Multiport Receivers Mitigating System Imperfections and Hardware Impairments", *IEEE Transactions on Microw. Theory and Techn.*, vol. 60, no. 8, pp. 2644-2653, 2012.

[70] A. Honda, K. Sakaguchi, J. Takada et al., "Six-port direct conversion receiver: novel calibration for multi port nonlinear circuits", *IEICE Trans. Electron*, vol. E87-C, no. 9, pp. 1389-1396, 2008.

[71] B. Mnasri, T. Djerafi, S. Tatu, K. Wu, "Dynamic range improvement of six-port interferometer receivers", *XXXIInd General Assembly and Scientific Symposium of the International Union of Radio Science (URSI GASS),* Aug. 2017.

[72] A. Koelpin, G. Vinci, B. Laemmle, D. Kissinger, and R. Weigel, "The six-port in modern society," Microwave Magazine, IEEE, vol. 11, no. 7, pp. 35-43, Dec. 2010.

[73] G. Vinci, A. Koelpin, F. Barbon, and R. Weigel, "A high accuracy direction-of-arrival and misalignment angle detector," in Proc. German Microwave Conference GeMiC 2011, Mar. 2011.

[74] T. S. Rappaport et al., “Overview of millimeter wave communications for fifth-generation (5G) wireless networks-with a focus on propagation models,” IEEE Transactions on Antennas and Propagation, Special Issue on 5G, Dec. 2017.

[75] T. S. Rappaport et al., “Broadband millimeter-wave propagation measurements and models using adaptive-beam antennas for outdoor urban cellular communications,” in IEEE Transactions on Antennas and Propagation, vol. 61, no. 4, Apr. 2013, pp. 1850–1859

[76] G. Vinci, F. Barbon, R. Weigel, and A. Koelpin, "A novel, wide angle, high resolution direction-of-arrival detector," in Proc. European Microwave Week (EUMW) 2011, Manchester, UK, 2011.

[77] B. Laemmle, G. Vinci, L. Maurer, A. Koelpin, R. Weigel, "An integrated 77-GHz six-port receiver front end for angle-of-arrival detection", *Proc. IEEE Bipolar/BiCMOS Circuits and Technology Meeting (BCTM)*, pp. 220-223, 2011.

[78] T. S. Rappaport *et al*., ‘‘Millimeter wave mobile communications for 5G cellular: It will work!’’ *IEEE Access*, vol. 1, pp. 335–349, Mar. 2013.

[79] S. Rangan, T. S. Rappaport, and E. Erkip, “Millimeter-Wave Cellular Wireless Networks: Potentials and Challenges,” *Proc. IEEE*, vol. 102, no. 3, pp. 366–385, Mar. 2014.

[80] C.-X. Wang *et al*., "Cellular architecture and key technologies for 5G wireless communication networks", *IEEE Commun. Mag.*, vol. 52, no. 2, pp. 122--130, Feb. 2014.

[81] U. Siddique, H. Tabassum, E. Hossain, D. I. Kim, "Wireless backhauling of 5G small cells: Challenges and solution approaches", *IEEE Wireless Commun*., vol. 22, no. 5, pp. 22--31, Oct. 2015.

[82] G. S. Shiroma, R. Y. Miyamoto, J. D. Roque, J. M. Cardenas, and W. A. Shiroma, "A high-directivity combined self-beam/ null-steering array for secure point-to-point communications,"*IEEE Trans. Microw. Theory Techn.*, vol. 55, no. 5, pp. 838--844, May 2007.

[83] F. F. He; K. Wu; W. Hong; L. Han; and X. Chen, " Low Cost 60-GHz Smart Antenna Receiver Subsystem Based on Substrate Integrated Waveguide Technology," *IEEE Trans. Microw. Theory Techn.*, vol.60, no.4, pp.1156--1165, Apr. 2012.

[84] Z. He *et al*.,"A Hardware Efficient Implementation of a Digital Baseband Receiver for High-Capacity Millimeter-Wave Radios", *IEEE Trans. Microw. Theory Techn*., vol. 63, no. 5, pp. 1683-1692, May 2015.

[85] J. Osth, A. Serban, Owais, M. Karlsson, S. Gong, J. Haartsen, and P. Karlsson, "Six-port gigabit demodulator," *IEEE Trans. Microw. Theory Tech*., vol. 59, no. 1, pp. 125-131, 2011.

[86] K. Haddadi, M. M. Wang, C. Loyez, D. Glay, and T. Lasri, “Four-port communication receiver with digital IQ-regeneration*,” IEEE Microw. Wireless Compon. Lett*., vol. 20, no. 1, pp. 58–60, Jan. 2010.

[87] C. de la Morena-Álvarez Palencia and M. Burgos-García, “Four-octave six-port receiver and its calibration for broadband communications and software defined radios,” *Progr. Electromagn. Res*., vol. 116, pp. 1–21, 2011.

[88] Y. Liu, “Calibrating an industrial microwave six-port instrument using the artificial neural network technique,” *IEEE Trans. Instrum. Meas.*,vol. 45, no. 2, pp. 651–656, Apr. 1996.

[89] E. Moldovan, S. Affes, S. O. Tatu, "A 60 GHz Multi-Port Receiver with Analog Carrier Recovery for Ultra-Wideband Wireless Personal Area Networks", *European Microwave Week (EuMW),* Amsterdam, pp. 27-31, Oct. 2008.

[90] S. O. Tatu, T. A. Denidni, "New millimeter-wave six-port heterodyne receiver architecture", *IEEE MTT-S Int. Microwave Symp*., pp. 11-16, Jun. 2006.

[91] B. Mnasri , T. Djerafi , S. Tatu , K.Wu, " Dual Input Interferometer Direct Conversion Receiver Architecture", 2018 18th International Symposium on Antenna Technology and Applied Electromagnetics (ANTEM), Waterloo, Aug. 2018.

[92] S. M. Winter, A. Koelpin, R. Weigel, "Six-port receiver analog front-end: Multilayer design and system simulation", *IEEE Trans. Circuits Syst. II Exp. Briefs*, vol. 55, no. 3, pp. 254-258, Mar. 2008.

[93] J. Östh et al., "Diode configurations in six-port receivers with simplified interface to amplifier and filter", *Proc. IEEE Int. Conf. Ultra-Wideband (ICUWB)*, pp. 360-363, Sep. 2010.

[94] J. Östh, Owais, M. Karlsson, A. Serban, S. Gong, "Performance evaluation of six-port receivers with simplified interface to amplifier and filter", *Proc. IEEE Int. Conf. Ultra-Wideband (ICUWB)*, pp. 190-194, Sep. 2011.

[95] X. Xu, R. G. Bosisio, K. Wu, "Analysis and implementation of six-port software-defined radio receiver platform", IEEE *Trans. Microw. Theory Techn.*, vol. 54, no. 7, pp. 2937-2943, Jul. 2006.

[96] W. Zhang, A. Hasan, F. M. Ghannouchi, M. Helaoui, Y. Wu, Y. Liu, "Novel calibration algorithm of multiport wideband receivers based on real-valued time-delay neural networks", *IEEE Trans. Microw. Theory Techn*., vol. 64, no. 11, pp. 3540-3548, Nov. 2016.

[97] W. Zhang, A. Hasan, F. M. Ghannouchi, M. Helaoui, Y. Wu, Y. Liu, "Design and calibration of wideband multiport homodyne wireless receivers", *IEEE Trans. Instrum. Meas*., vol. 66, no. 12, pp. 3160-3169, Dec. 2017.

[98] W. Zhang, A. Hasan, F. M. Ghannouchi, M. Helaoui, Y. Wu, Y. Liu, "Concurrent dual-band receiver based on novel six-port correlator for wireless applications", *IEEE Access*, vol. 5, pp. 25826-25834, Oct. 2017.

[99] M. Shafi *et al*., "5G: A tutorial overview of standards, trials, challenges, deployment, and practice," *IEEE Journal on Selected Areas in Communications*, vol. 35, no. 6, pp. 1201–1221, Jun. 2017.

[100] X. Cai and G. B. Giannakis, "Bounding performance and suppressing inter carrier interference in wireless mobile OFDM," *IEEE Trans. Commun*.,vol. 51, no. 12, pp. 2047–2056, Dec. 2003.

[101] J. Lee et al., "A 75-GHz phase-locked loop in 90-nm CMOS technique," *IEEE J. Solid-State Circuits*, vol. 43, no. 6, pp. 1414–1426, Jun. 2008.

[102] M. D. McKinley, K. A. Remley, M. Myslinski, J. S. Kenney, D. Schreurs, and B. Nauwelaers, "EVM calculation for broadband modulated signals," in *Proc. 64th ARFTG Conf. Dig.*, pp. 45–52, Dec. 2004.

[103] ZX4755+ Datasheet: https://www.minicircuits.com/pdfs/ZX47-55+.pdf

[104] C. Mittermayer and A. Steininger, "On the determination of dynamic errors for rise time measurement with an oscilloscope," *IEEE Trans. Instrum. Meas.*, vol. 48, no. 6, pp. 1103–1107. Dec. 1999.

[105] J. A. Lima, J. M. W. Rogers, and R. E. Amaya, "Optimization of EVM Through Diode Bias Control Using a Blind Algorithm Applied to Multiport Receivers" *IEEE Trans. Circuits and Systems.*, vol. 62, no. 3, pp. 286–290. Mar. 2015.

[106] AD8318 Datasheet: https://www.analog.com/media/en/data sheets/AD8318.pdf

APPENDIX A-LIST OF PUBLICATIONS

Patent

[1] **Mnasri, B.**, Djerafi, T., Tatu, S. & Wu, K. (2018). "Spatially-distributed multi-input interferometer receiver for 5G backhauling systems." U.S. Patent No. 16/024,210.

Peer reviewed Journal Papers

[1] **Mnasri, B.**, Djerafi, T., Tatu, S. & Wu, K." Spatially Distributed Multi-Input Interferometric Receiver for 5GWireless Systems and Beyond ", *IEEE Trans. on Microw. Theory and Techn.*, vol. 67, no. 7, pp. 2904-2915, Jul. 2019.

[2] Burasa, P., **Mnasri, B.**, & Wu, K." Millimeter-Wave CMOS Sourceless Receiver Architecture for 5G-Served Ultra-Low-Power Sensing and Communication Systems", *IEEE Trans. on Microw. Theory and Techn.*, vol. 67, no. 5, pp. 1688-1696, Mar. 2019.

[3] **Mnasri, B.**, Tatu, S. & Wu, K." Multi-Input Interferometric Receiver for Joint Demodulation and Angle of Arrival Detection," to be submitted to *IEEE Transactions on Microwave Theory and Techniques*

Conference Papers

[1] **Mnasri, B.**, Djerafi, T., Tatu, S. & Wu, K." Dual Input Interferometer Direct Conversion Receiver Architecture", *18th International Symposium on Antenna Technology and Applied Electromagnetics ANTEM*., Waterloo, August, 2018.

[2] **Mnasri, B.**, Burasa, P., Tatu, S. & Wu, K." Interferometer based Direction-Of-Arrival Detection System", *18th International Symposium on Antenna Technology and Applied Electromagnetics ANTEM*., Waterloo, August, 2018.

[3] Burasa, P., **Mnasri, B.**, & Wu, K." A Sourceless Low-Power mmW Receiver Architecture Using Self-Oscillating Mixer Array in 65-nm CMOS", *2018 IEEE Wireless Power Transfer Conference (WPTC)*, Montreal, June, 2018.

[4] **Mnasri, B.**, Djerafi, T., Tatu, S. & Wu, K." Dynamic range improvement of six-port interferometer receivers" *XXXIInd General Assembly and Scientific Symposium of the International Union of Radio Science (URSI GASS)*, Montreal, August, 2017.